
El Niño/Southern Oscillation during the Holocene and Eemian Warm Periods

**Dissertation
zur Erlangung des Doktorgrades
der Mathematisch-Naturwissenschaftlichen Fakultät
der Christian-Albrechts-Universität
zu Kiel**

**Vorgelegt von
Opeyemi R. S. Salau**

Kiel 2012

Referent:	Professor Birgit Schneider
Korreferent:	Professor Mojib Latif
Tag der Disputation:	05.07.2012
Zum Druck genehmigt:	05.07.2012
Der Dekan:	gez Prof. Dr. Lutz Kipp

Table of Contents

Table of Contents	v
List of Acronyms	vii
Acknowledgements	viii
Abstract	ix
Zusammenfassung	xi
1 Introduction	1
1.1 Background and Motivation.....	1
1.2 The Orbital Parameters	7
1.2.1. Obliquity	7
1.2.2. Precession.....	9
1.2.3. Eccentricity	10
1.3 The Observed and Modelled Orbitally-Induced Climate Variability	10
1.3.1 Descriptions of the Holocene and the Eemian Climates	11
1.3.2 Observed and Modelled ENSO Variability	13
1.4 Tropical Pacific Climate	14
1.4.1 The Annual Mean State.....	15
1.4.2 The Seasonal Cycle.....	18
1.4.3 The Interannual Variability.....	20
1.5 Research Objectives	26
2 Model and Experimental Set Up	29
2.1 Description of the Kiel Climate Model (KCM)	29
2.2 The Control Experiment	30
2.3 Tropical Pacific Climate in the Preindustrial Control Simulation and Observation.....	32
2.3.1 SST - The Annual Mean State.....	32
2.3.2 SST - The Seasonal Cycle and the Interannual Variability	34
2.3.3 Precipitation - The Annual Mean State.....	35
2.3.4 Precipitation - The Seasonal Cycle and the Interannual Variability	37
2.4 Changes in the Simple Indices	37
2.5 The Experiments	38

3 The Impacts of Orbital Forcing.....	43
3.1 Changes in the Tropical Pacific Mean Climate.....	43
3.1.1 SST - The Annual Mean State.....	43
3.1.2 SST - The Seasonal Cycle.....	45
3.1.3 SST - The Interannual Variability	46
3.1.4 The Semi-annual and Annual cycles.....	47
3.1.5 Changes in the Surface Heat Flux and the Ocean Heat Transport.....	49
3.2 Changes in the Simulated ENSO	52
3.2.1 Changes in the Simple Indices	52
3.2.2 Link to the Mean State Change	53
3.3 Relationship between the Mean State and Changes in the Atmospheric Circulation.....	55
3.3.1 Relationship with seasonal changes in the SST and Zonal Wind Stress.....	55
3.3.2 Changes in the Velocity Potential and Walker Circulation.....	57
3.3.3 Changes in the Tropical Pacific Mean State and the North-South Migration of ITCZ..	60
3.3.4 Simulated Changes in the Cloud Cover, Precipitation and Water Vapour.....	62
3.4 Phase Locking of the ENSO Variability to the Annual Cycle	64
3.5 Effect of individual Orbital Parameters on the Mean Climate	65
3.6 Summary.....	66
4 Comparison with other Studies	69
4.1 Comparison of KCM Result with Paleo-reconstruction.....	69
4.2 Comparison of the KCM Results with Model Studies	70
4.3 Summary.....	75
5 Discussion.....	77
5.1 Discussion of the Main Findings.....	77
5.1.1 The link between ENSO variability and the Tropical Pacific Mean State	77
5.1.2 The Response of ENSO to changes in the mean state in other Model Experiments	78
5.1.3 The Changes in the Frequency of the ENSO Variability	79
5.1.4 The ENSO Variability and Changes in the ITCZ Position	80
5.1.5 The ENSO Amplitude and the Annual SST Cycle.....	80
5.2 The Setbacks and Model Biases.....	81
5.3 Summary and Conclusion.....	81
5.4 Possible Future Research.....	82
References.....	87

List of Acronyms

ENSO	E l Niño/ S outhern O scillations
SST	Sea Surface Temperature
SSTA	Sea Surface Temperature Anomaly
WEP	Western Equatorial Pacific
EEP	Eastern Equatorial Pacific
TOA	Top of atmosphere
SLP	Sea Level Pressure
WPWP	Western Pacific Warm Pool
WP	Warm Pool
CT	Cold Tongue
AOGCM	Atmosphere-Ocean General Circulation Model
ITCZ	I nter T ropical C onvergence Z one
1kyr BP	1 kilo Y ear B efore P resent or 1000 years Before Present
1ka	1 kiloannum (=10 ³ years)
SOI	S outhern O scillation I ndex
NH	Northern Hemisphere
SH	Southern Hemisphere
AWV	Atmospheric Water Vapour
EHT	Early Holocene Trend
LHT	Late Holocene Trend
FHT	Full Holocene Trend
EET	Early Eemian Trend
LET	Late Eemian Trend
FET	Full Eemian Trend
HC	Hadley Circulation
WC	Walker Circulation
SSH	Sea Surface Height

Acknowledgements

I wish to express my profound gratitude to my primary supervisor, Prof. Dr. Birgit Schneider for giving me the opportunity to do my PhD in her group and for excellent supervision of my thesis. I appreciate her steady academic support, advice, her assistance whenever I have question and for creating the most conducive international environment in her group. I am very grateful to Prof. Mojib Latif for his guide, academic supervision of my PhD, and for creating time to attend to me and share his expert knowledge with me. I would like to thank Dr. Wonsun Park for his support at the time of problems and difficulties in handling the Kiel Climate Model.

Special thanks to Prof. Ralph Schneider for creating platforms for exchange of ideas between the working groups through seminars and workshops. I am grateful to the members of our working group for the friendly working environment. Thanks to Stefanie Maack, Vyacheslav Khon and Anke Dürkop for reading part of my texts and Alexander Keidel for his assistance. Others are Uta Krebs-Kanzow for her advice and reading of my texts, Laura Bordelon and Li-Ya Jin for their readiness to assist and for the family-like condition in our office - it is interesting to know that we are all from different continents. I would like to extend my appreciation to Janne Repschläger, Guillaume Leduc, Ogundari Kolawole, Tijani Yakub, Uzor Osmund and Omolade Oluwaseun for reading my texts. I also thank Elfi Mollier-Vogel, Veronica Krossa, Thomas Larsen, Yiming Wang, Jeroen van der Lubbe, Camille Butruille, Emma Khadun, Mohamed Aquit, Elena Lo Giudice, Nicholas Fraser, Janne Lorenzen, Regenberg Marcus, Sebastian Meier, Tim Bolliet, Khélifi Nabil, Wolf-Achim Kahl, Christine Bauke, Sven Nielsen and Ogundemuren Adeleke.

I am grateful to my wife Mrs Tanja Salau for her support throughout the time of my study. I really appreciate the support and assistance provided by my parents - Chief Salau Egunjobi (RIP) and Mrs Monisola Salau. Many thanks to Tim and Juliya Thomsen, Cedric and Chidera Glenz, Svenja and Heiko, Mr Richard Plagge, Mrs Sabine Plagge and to the Salau's family like Alhaji Salau A. Aderemi, Salau Oluwasola, Salau Lasisi, Salau Ojo, Taiwo and Oluwatoyin Oluwabusuyi, Oluwatosin Olajutemu and my daughter, Salau Joy. Thanks to H.R.H Oba M.O. Aladejana and the wife Mrs Victoria Aladejana, Mrs Olayinka, Prince Bisi Aladejana (RIP) and the wife Mrs Adunni Aladejana. I am very grateful to Prof. I. O. Orubuloye, the former vice chancellor of the University of Ado-Ekiti (2004-2008), Nigeria for his support and assistance during the study. Thanks to the administration of the University of Ado-Ekiti (now Ekiti State University, EKSU) for their support throughout the time of my study. Finally, I give glory to God for making this work possible.

This work was supported by the Cluster of Excellence 'The Future Ocean' (DFG EXC80/1) and the SFB754, funded by the German Science Foundation (DFG), I am very grateful to them for making my dream come true. Thanks to the Computing Centre of the University of Kiel that made the model integrations possible.

Abstract

El Niño/Southern Oscillation (ENSO) is a natural interannual climate fluctuation originating in the Tropical Pacific Ocean, which affects climate worldwide through atmospheric teleconnections. The sensitivity of ENSO phenomenon to changes in the mean Tropical Pacific climate is investigated with a coupled atmosphere-ocean-sea ice general circulation model (AOGCM), the Kiel Climate Model (KCM). Different mean climate states of the two most recent interglacial warm periods, the Holocene (last 10 kyr BP) and the Eemian (126–115 kyr BP), were generated by changing the orbital parameters that determine the latitudinal and seasonal distribution of the top of atmosphere (TOA) solar insolation which was the major driver of both climates. The orbital induced insolation changes throughout the Eemian are about twice as large as the changes throughout the Holocene. This is due to the higher values of eccentricity which is about twice the value in the Holocene but both exhibits a largely similar seasonal and latitudinal structure of the TOA insolation. Changes in all other climate forcings such as variations in greenhouse gas concentration and continental ice volume are considered to be of minor importance during the periods of interest (Holocene, Eemian) and have been neglected for the benefit of comparability.

The simulated annual mean TOA insolation and the corresponding sea surface temperature (SST) increases over time in the Tropical Pacific in both the Holocene and the Eemian. The resulting ENSO amplitude is positively correlated with both the Equatorial Pacific SST and the Equatorial zonal SST contrast. The latter is controlled by the upwelling-induced dampening of the SST changes in the Eastern Equatorial Pacific (EEP), and by the vertical ocean dynamical heating and zonal heat transport convergence in the Western Equatorial Pacific (WEP). The ENSO amplitude also correlates positively with the seasonal SST amplitude in the EEP and negatively with the strength of the easterly Trades over the Equatorial Pacific. Only minor variations in the upper ocean heat content of the Tropical Pacific are simulated, indicating that the origin of the ENSO changes is primarily linked to surface layer processes. The enhanced SST gradient in conjunction with weakened trades suggests the direct radiative forcing effects played a role in addition to air-sea interactions. However, the ENSO period is rather stable and stays within 3-4 years. Enhanced ENSO amplitude is simulated during the late-Holocene, in agreement with paleo proxy records. The tight positive correlation ($r=0.89$) between the ENSO strength and the Western Pacific Warm Pool (WPWP) SST suggests that the latter may provide an indirect measure of the ENSO amplitude from proxy data that cannot explicitly resolve interannual variability.



Zusammenfassung

El Niño/Southern Oscillation (ENSO) ist die Bezeichnung für eine natürliche Fluktuation des Klimas auf mehrjähriger Zeitskala, welche ausgehend vom Ostpazifik durch atmosphärische Telekonnektionen weltweit das Klima beeinflusst. Die Sensitivität des ENSO Phänomens gegenüber Veränderungen im mittleren Klima des tropischen Pazifik wird hier untersucht mithilfe des Kiel Climate Models (KCM), einem gekoppelten allgemeinen Zirkulationsmodell von Ozean, Atmosphäre und Meereis (AOGCM). Erzeugt wurden verschiedene mittlere Klimazustände der letzten beiden interglazialen Warmzeiten, dem Holozän (die letzten 10000 Jahre) und dem Eem (126000-115000 Jahre vor heute) durch Variation der Orbitalparameter, welche die breitenabhängige und jahreszeitliche Verteilung der solaren Einstrahlung an der Oberseite der Atmosphäre (TOA) bestimmen und welche die Haupteinflussfaktoren für beide Klimaepochen darstellen. Aufgrund einer größeren Exzentrizität sind die orbital bedingten Einstrahlungsänderungen während des Eems ungefähr doppelt so groß wie während des Holozäns, zeigen aber eine weitgehend ähnliche jahreszeitliche und breitenabhängige Struktur. Veränderungen weiterer klimabestimmender Faktoren, wie etwa Treibhausgaskonzentration und kontinentales Eisvolumen, wurden als zweitrangig für die untersuchten Klimaperioden (Holozän und Eem) erachtet und wurden zugunsten der Vergleichbarkeit vernachlässigt. Sowohl im Verlauf des Holozän als auch im Verlauf des Eems steigt über dem tropischen Pazifik die solare Jahreseinstrahlung an der Oberseite der Atmosphäre.

In beiden Warmzeiten gehen diese positiven Trends in der solaren Jahreseinstrahlung mit einem Anstieg der simulierten mittleren jährlichen Meeresoberflächentemperaturen (SST) im tropischen Pazifik einher. Die resultierende ENSO Amplitude ist positiv korreliert, sowohl mit der Äquatorialpazifischen SST, als auch dem zonalen SST Kontrast entlang des pazifischen Äquators. Letztere Korrelation wird kontrolliert durch die auftriebsbedingte Dämpfung von SST-Veränderungen im östlichen äquatorialen Pazifik (EEP) und durch vertikale dynamische Erwärmung und Konvergenz des zonalen Wärmetransports im westlichen äquatorialen Pazifik. Die ENSO Amplitude korreliert außerdem positiv mit der jahreszeitlichen SST Amplitude im EEP und negativ mit der Stärke der Passatwinde über dem äquatorialen Pazifik. Der simulierte Wärmeinhalt der Deckschicht des tropischen Pazifiks schwankt nur geringfügig, was darauf hinweist, dass die Ursache der ENSO-Veränderungen in erster Linie mit Vorgängen in der oberflächennahen Schicht verknüpft ist. Der verstärkte SST-Gradient zusammen mit den abgeschwächten Passatwinden deutet darauf hin, dass zusätzlich zu der direkten Wirkung der Einstrahlung, auch Ozean-Atmosphären-Wechselwirkungen involviert sind. Die ENSO-Periode hingegen bleibt mit 3-4 Jahren nahezu unverändert. Die verstärkte ENSO Amplitude in der Simulation des späten Holozäns stimmt mit Paleorekonstruktionen überein. Die starke positive Korrelation ($r=0.89$) zwischen ENSO-Amplitude und SST des westlichen, pazifischen Warm Pool (WPWP) legt nahe, dass Temperaturrekonstruktionen des WPWP ein

indirektes Maß für die ENSO Amplitude liefern könnten, ohne zwischenjährliche Variabilität explizit auflösen zu müssen.

CHAPTER ONE

Introduction

1.1 Background and Motivation

The accurate prediction of El Niño/Southern Oscillation (ENSO) event in a changing climate is still hindered by poor understanding of the relationship between the changes in the mean state of the Tropical Pacific and the modulation of the ENSO amplitude [Li *et al.*, 2011; Kucharski *et al.*, 2011, and the references therein]. Several studies have shown that the response of the ENSO to global warming is model dependent with some models reporting a reduction in the ENSO amplitude while the amplitude rises in another set of models and remain unchanged in the others [Latif and Keenlyside, 2009; Collins *et al.*, 2010; Cane, 2005]. An excellent way of assessing the sensitivity of ENSO to climate variations is through better understanding of its characteristics in the past climate conditions [Timmerman *et al.*, 2007]. Hence, this thesis describes the influence of the orbitally-induced changes in the mean Tropical Pacific climate on the ENSO variability during the Holocene and Eemian climates, which have comparable orbital forcing with increased warming in the Eemian. This is necessary since changes in the orbital forcing have been identified as the main driver of climate variability during the Holocene [Lorenz *et al.*, 2006; Braconnot *et al.*, 2008; Berger, 1988; Mayewski *et al.*, 2004]. Similarly, the orbital forcing was also an important factor driving climate change during the Eemian [Montoya *et al.*, 2000; Kutzbach *et al.*, 1991; Crowley and Kim, 1994]. The aim of this study is to contribute to the improvement of ENSO prediction and the overall climate prediction.

ENSO event is a prominent complex natural interannual climate fluctuation in the Tropical Pacific Ocean that is usually explained by either a naturally sustained oscillation or by a damped mode forced by atmospheric noise [Neelin *et al.*, 1998; Wang and Picaut, 2004; Fedorov and Philander, 2000; McWilliams and Gent, 1978; Lau, 1985; Kleeman and Moore, 1997; Penland and Sardeshmukh, 1995; Eckert and Latif, 1997; Kessler, 2002; Moore and Kleeman, 1999; Thompson and Battisti, 2001; Dijkstra and Burgers, 2002; Larkin and Harrison, 2002; Zavala-Garay *et al.*, 2003; Blanke *et al.*, 1997]. The atmospheric component of the air-sea interactions called the Southern Oscillation (SO), is characterized by rising pressure in the western Pacific which drops in the east as the region warms during an El Niño event (warm phase) while the pattern is reversed in the La Niña period (cold phase) [Latif and Keenlyside, 2009; Wang and Schimel, 2003]. Some of these robust relationships between ENSO and the mean Tropical Pacific climate state have been successfully derived with the current generation of climate models [Guilyardi, 2006], which are supported by 1000 years of tree ring data of

the past millennium from the North American continent [Li *et al.*, 2011]. For example, ENSO strength in the models has been shown to be an inverse function of the mean trade wind strength in the Central Equatorial Pacific as well as of the relative strength of the seasonal cycle in the Eastern Equatorial Pacific. Changes of the mean state also affect the feedback loops such that in a warm climate, for instance, SST sensitivity is amplified due to an increased sharpness of the thermocline. However, various competing processes act at the same time so that it is difficult to anticipate the net effect of future expected warming [Philip and van Oldenborgh, 2006]. Nevertheless, the results from climate model simulations are important to understand the effect of mean state changes on ENSO and ocean-atmosphere feedbacks in the Tropics.

The El Niño event ("the boy child" in Spanish) was first observed in the late-nineteenth century (1801-1900) by fishermen along the coast of Ecuador and Peru around Christmas time [Dijkstra and Burgers, 2002; Wang and David, 2002; Cane, 2005]. However, earlier events have been linked to the existence of the both El Niño and La Niña (ENSO) which continued till the modern time, these include the events in 1790-1793, 1828, 1876-1878, 1891, 1925-1926, 1972-1973, 1982-1983, and 1997-1998 years [Davis, 2001; see also McPhaden, 1999]. ENSO is associated with anomalous regional wind, precipitation and temperature patterns [Ropelewski and Halpert, 1995] that change upper ocean stratification and vertical motion, and thus nutrient conditions [Stenseth *et al.*, 2002]. Once started, an ENSO event can persist for more than a year while the frequency of successive El Niño events is about 2-7 years [Guilyardi *et al.*, 2009; Clement *et al.*, 1999; Collins *et al.*, 2010; Liu *et al.*, 2000; Cane, 2005; Stute *et al.*, 2001]. The phenomenon influences not only the climate and biosphere but also the economies of Tropical Pacific and several countries worldwide through atmospheric teleconnections, thereby affecting human societies [Philander, 1990; McPhaden *et al.*, 1998, 2006; Chavez *et al.*, 1999]. For instance, the poor crop yield experienced in Europe in 1789-1793 has been attributed to El Niño [Grove, 1998] while the event was also responsible for the deadly famine caused by the extreme weather conditions in 1876-1877 [Ó Gráda, 2009; Cane, 2005].

During an El Niño, the supply of nutrients to the euphotic (sunlit) zone is cut off or slowed down by the surface warming in the eastern Pacific [Wang and Schimel, 2003], thus lowering the marine productivity in the region. Consequently, the sustainability of the existing commercial fisheries along the east coast of the Tropical Pacific is threatened by the low fish population caused by the insufficient marine primary productivity [Wang and Schimel, 2003]. The El Niño is accompanied by strong precipitation along the Peruvian and Chilean coasts of the Eastern Equatorial Pacific, EEP (Figs. 1.1a, b) [Latif and Keenlyside, 2009]. The eastward shift in the region of strong precipitation is capable of transforming the coastal desert to grassland in the EEP. For instance, the 1997-98 El Niño event leads to flooding in Peru, Ecuador and dryness in Bolivia and within the Nordeste part of Brazil [Cane, 2005]. Also, the Mosquito-borne malaria diseases will be on the rise under the influence of heavy rainfall along the Peruvian coast in the EEP during an El Niño year. The numbers of Tropical

cyclones rise in the eastern and central Pacific while they are suppressed over the Tropical Atlantic [Pielke and Landsea, 1999]. In addition, the Southern California gets more rainfall while the numbers of frost days rises in Florida, USA [Latif and Keenlyside, 2009].

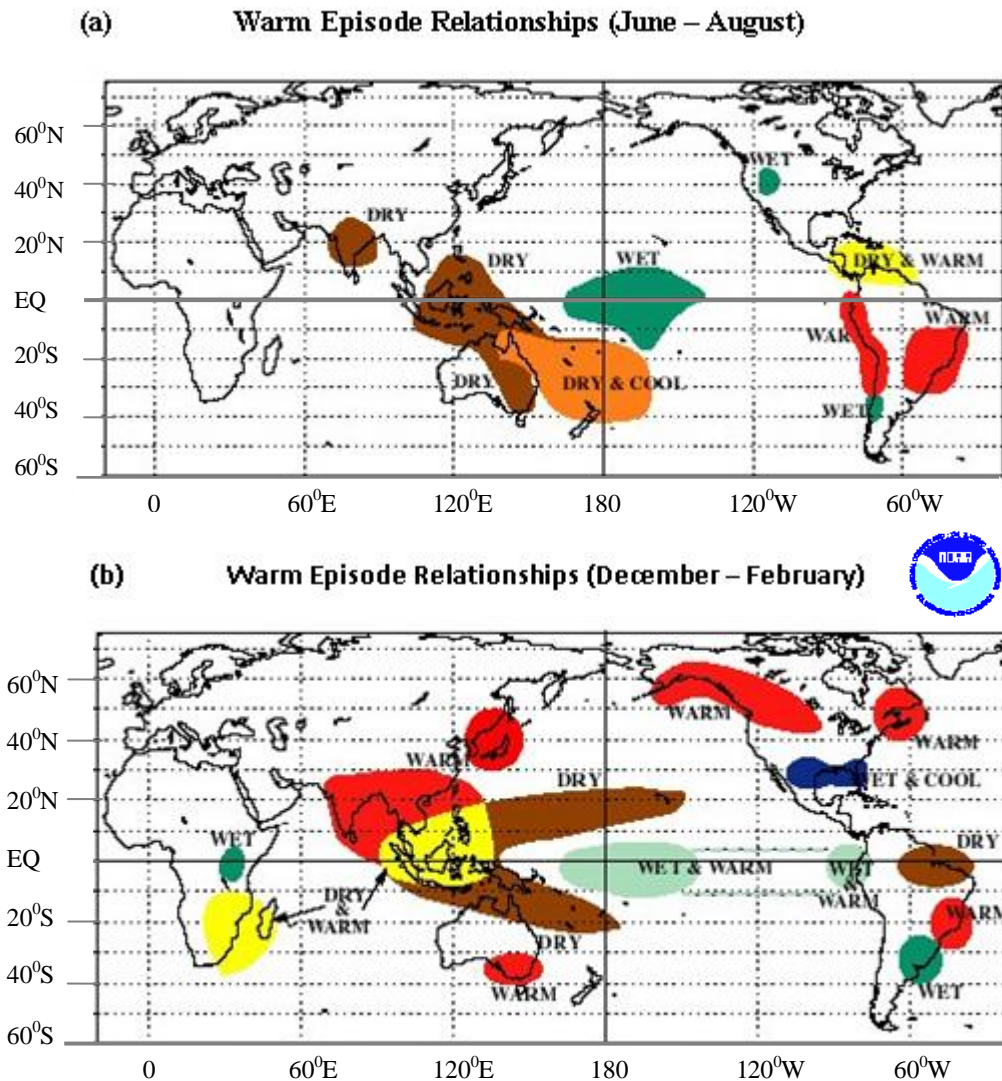


Figure 1.1: The Global influence of the shift in the regional temperature and precipitation during an El Niño event in (a) June-August and (b) December-February. The pattern depends on different event. (Adapted from NOAA Climate Prediction Center, NCEP).

Conversely, the western Pacific is under intense drought due to reduced rainfall [Latif and Keenlyside, 2009] with possible frequent incidences of forest fires [Cane, 2005], desertification and famine due to crop failure during an El Niño event (Figs. 1.1a, b). In their investigation, Page *et al.* [1997] reported an increase in the atmospheric carbon due to rise in wildfires from Indonesia and other drought affected Tropical regions [Schimel and Baker, 2002] during the 1997-1998 El Niño events. In addition, the closure of airports in Singapore, Malaysia and Indonesia during the 1997-1998 El Niño periods has been attributed to the thick smoke from the widespread bush burning in Kalimantan,

Indonesia [Cane, 2005]. The damages and low agricultural yield caused by the associated drought puts the farmers from Indonesia and Australia at disadvantage in the El Niño years [Latif and Keenlyside, 2009]. Similarly, the reduction in the monsoon rain over India during an El Niño event [Liu, 2002; Kripalani and Kulkarni, 1997] (Fig. 1.1a) might lead to famine in the region [Cane, 2005] due to less agricultural outputs and weakened the economy which rely heavily on agriculture. The crop types and the yields were influenced by ENSO events in the East Africa with more productivity from suitable crops during the extended rainy season caused by strong easterly winds in the El Niño years in Uganda [Phillips and McIntyre, 2000] while Southern Africa become warm and dry (Fig. 1.1b). The overall global effects of the shift in the temperature and precipitation patterns for different regions during an El Niño event are summarized in the Figure 1.1 (a, b).

The El Niño conditions and the effects are mostly reversed during a La Niña event [Latif and Keenlyside, 2009]. A La Niña (“the little girl” in Spanish) event is associated with westward shifts of the Tropical Pacific rainfall and wind patterns, resulting in dryness over the eastern Pacific (Figs 1.2a, b). The event has global and regional impacts on the agriculture, economy and human social life. For instance, the La Niña event is accompanied by less Tropical storm and less hurricane activities over the eastern and central Pacific while their occurrences increase in the Tropical Atlantic region [Pielke and Landsea, 1999]. In their report, Pielke and Landsea [1999] revealed that the damages from the hurricanes along the American Atlantic are higher during La Niña events compared to the El Niño periods. The paper showed that the cost of damages from either extreme La Niña or El Niño event is in billions of US dollars. Also, the intensification of the monsoon rain caused by the strong Hadley Circulation (HC) and Walker Circulation (WC), raises the agricultural yield which results in improved economy of India during a La Niña year. Also, the West Africa cools (Fig. 1.2a) while it becomes wetter in the East Africa during the cold phase of ENSO events (Fig. 1.2b).

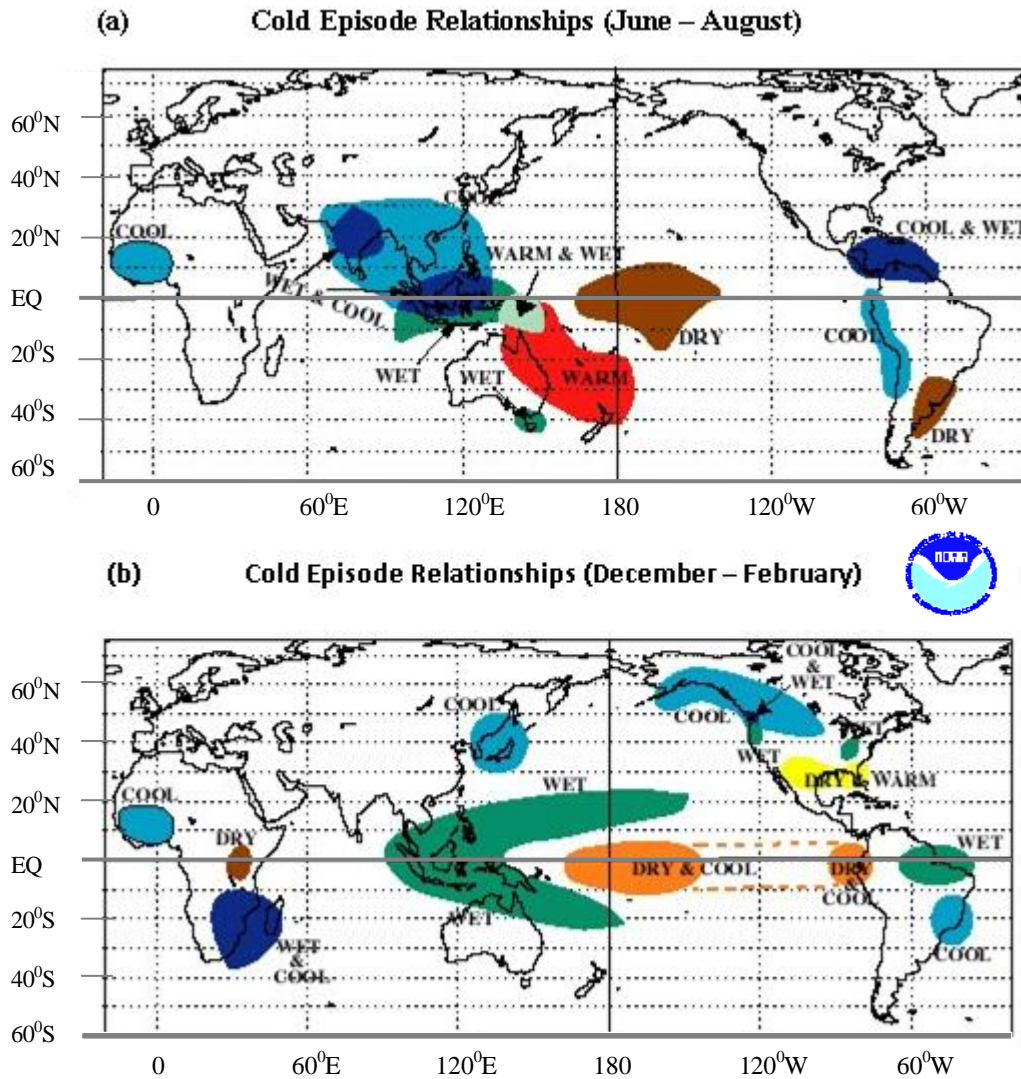


Figure 1.2: The Global influence of shift in the regional temperature and precipitation during La Niña in: (a) June-August and (b) December-February. The pattern can vary with different La Niña event (Adapted from NOAA Climate Prediction Center, NCEP).

The strong and widespread impacts of the observed El Niño in the last decades has brought the ENSO to prominence and inspired innovative climate research which has led to improved predictability of the event in the recent years [Pielke and Landsea, 1999; Tudhope et al., 2001]. However, the improvement in the understanding of the physics and modelling of the ENSO is still overshadowed by uncertainties in the response of the event to future climate change [Brown et al, 2008] due to inaccuracies in model simulations [Latif et al, 2001] and inconsistent natural fluctuations. The natural variability is usually induced by external factors (like changes in solar radiation) and the internal sources (including the non-linear interactions between the ocean and atmosphere, atmosphere and biosphere) which are more difficult to predict than the former. For example, the observation from Tropical Ocean-Global Atmosphere (TOGA) data revealed that the ENSO variability is not steady and limits the predictability of the event to about 1 year [McPhaden et al., 1998]. This is in agreement with

the one year forecast of the El Niño in 1985 by the first successful model prediction of the event by *Cane and Zebiak*, [1987]. Presently, no model has the accurate skill needed to forecast the event with a better and longer lead-time [*Landsea and Knaff*, 2000; *Neelin and Latif*, 1998]. Also, models' ability to anticipate the right amplitude of the El Niño's peak at a medium range lead-time of about 6 to 11 months is still a problem [*Landsea and Knaff*, 2000]. These inaccuracies have lowered our confidence in the efficiency of current models to accurately predict ENSO changes [*Walsh and Pittock*, 1998; *Fedorov and Philander*, 2000].

Presently, little is known about the modulation of the ENSO by natural decadal to millennial climate variations [*Clement et al.*, 1999], an accurate knowledge of the modulation patterns might improve ENSO predictability. There is evidence that the ENSO amplitude increases over the relatively stable Holocene period which started at about 11,000 years ago till the late Holocene period [*Moy et al.*, 2002]. The increase is attributed to alteration in the top of atmosphere (TOA) insolation caused by variations in the orbital obliquity (tilt of the Earth's axis), precession (dates of perihelion or Earth's closest distance from the Sun) and the eccentricity (deviation of the Earth's orbit from a circular path) on the multi-millennial time scale [*Milankovitch*, 1941]. Another period which is mostly comparable with the Holocene in terms of changes in the orbital parameters, insolation trends and the long-term climate trends is the Eemian which covered 126 kyr BP to 115 kyr BP in this study. However, the Eemian is less documented than the Holocene while the changes in the orbital forcing and the resulting warming are weaker (especially in the low latitudes) during the Holocene compared to the Eemian [*Leduc et al.*, 2010].

Evidence from recent data also raised the questions on whether the characteristics of ENSO (amplitude and frequency) are changing with rising concentration of greenhouse gases and increased global warming [*Clement et al.*, 2000]. For instance, the existence of ENSO in the last 130 kyr BP has been confirmed in the annually banded corals from Papua New Guinea with stronger ENSO amplitude in the modern day compared to any time over the last 150 kyr BP which is probably induced by both orbital precession and glacial dampening [*Tudhope et al.*, 2001]. According to the findings using the lake sediments from Ecuador, the observed ENSO period is above 15 years during 15-7 kyr BP interval while the present periodicity is between 2-8 years [*Rodbell et al.*, 1999, *Zelle et al.*, 2005]. Furthermore, the model studies reported by *Timmermann et al.* [1999] and *Collins* [2000a] suggested that an amplification of the surface temperature over the Tropical Pacific due to rising atmospheric CO₂ will likely be unsteady and may lead to intensification of ENSO variability [*Clement et al.*, 2000]. However, while the response of ENSO to increasing global warming raises the ENSO amplitude in some models, the amplitude decreases in other models and shows no significant change of amplitude in the remaining groups of models [*Collins et al.*, 2010]. In addition, the changes in the ENSO events, frequency and phase lock simulated with the second version of the Hadley Centre Coupled Ocean–Atmosphere General Circulation Model (HadCM2) [*Zelle et al.*, 2005] are missing in the ENSO

statistics obtained using the new (third) version of the model (HadCM3) [Collins *et al.*, 2000b]. These discrepancies have been attributed to differences in the physical parameterization of the models rather than to the resolution of the different models [Zelle *et al.*, 2005].

For a better picture of the changes in the ENSO amplitude and frequency for the future, an excellent understanding of the influence of natural forcing induced by changes in solar irradiance may play an important role in improving our knowledge of climate predictability. In their findings, Fedorov and Philander [2001] also indicate that the ocean-atmosphere feedbacks and the resulting growth rate of the ENSO events, depend on the changes in the mean background climate induced by the trade winds, thermocline (Z20) depth (boundary between the warm surface and cold subsurface waters) and the difference in the temperature across the Z20 depth. Hence, this study will go a step further to investigate the effect of changes in the orbital parameters on the Tropical Pacific mean climate and in particular on its interannual variability. The experiments will be done by using a coupled atmosphere-ocean general circulation model (AOGCM) to study the Holocene and the Eemian climates which only differ in their respective solar forcing.

1.2 The Orbital Parameters

For more than a century of investigation, many questions on the causes of climate variability are still unanswered despite several attempts made to unravel the mystery. However, the orbital hypothesis seems to provide the only explanation that could be tested geo-logically [Hays *et al.*, 1976]. Named after the Mathematician, the Milankovitch [1941] theory suggests that the shape of the Earth's orbit around the Sun and the distribution of the TOA insolation are strongly controlled by the orbital obliquity, eccentricity and the precession. The theory indicates that the seasonal cycle of the solar irradiance induced by the varying orbital parameters has one of the strongest impacts on the long term climate change [Berger, 1988; Lorenz *et al.*, 2006]. However, there is no clear understanding of the mechanisms responsible for the amplification and the observed feedback in the climate system [Timm *et al.*, 2008 and the references therein]. Hence, the brief descriptions of the characteristics of the orbital parameters are presented in this section.

1.2.1. Obliquity

The obliquity (or tilt, **T**) of the Earth's axis describes the variations in the angle between the Earth's axis and the plane of Earth's orbit (Fig. 1.3). The value (**T**) fluctuates between 22° and 24.5° over a period of about 41,000 year's cycle, the present value is about 23.4° [Buchdahl, 1999] (Fig. 1.4). The Earth's tilt is responsible for the existence of seasons while the strength of the season is modified by changes in the tilt [Buchdahl, 1999] such that an increase (reduction) in the tilt amplifies (lowers) the seasonality. A low obliquity reduces (increases) the annual mean TOA insolation received at high latitudes (low latitudes) while the impact of changes in the obliquity decreases toward the equator

[Buchdahl, 1999]. At low tilt, the sunlight received at the poles is less since the sun's rays are reaching the polar surface at low angles, reducing the energy received per unit area while reflection increases [Rohling *et al.*, 2008]. As the obliquity decreases, the associated reduction in the temperature at high latitudes might lead to an ice age after years of continuous accumulation of snow and ice that are left from previous years. In addition, a high obliquity results in the amplification of the annual mean solar energy at high latitudes while the latitudinal temperature gradient decreases [Buchdahl, 1999].

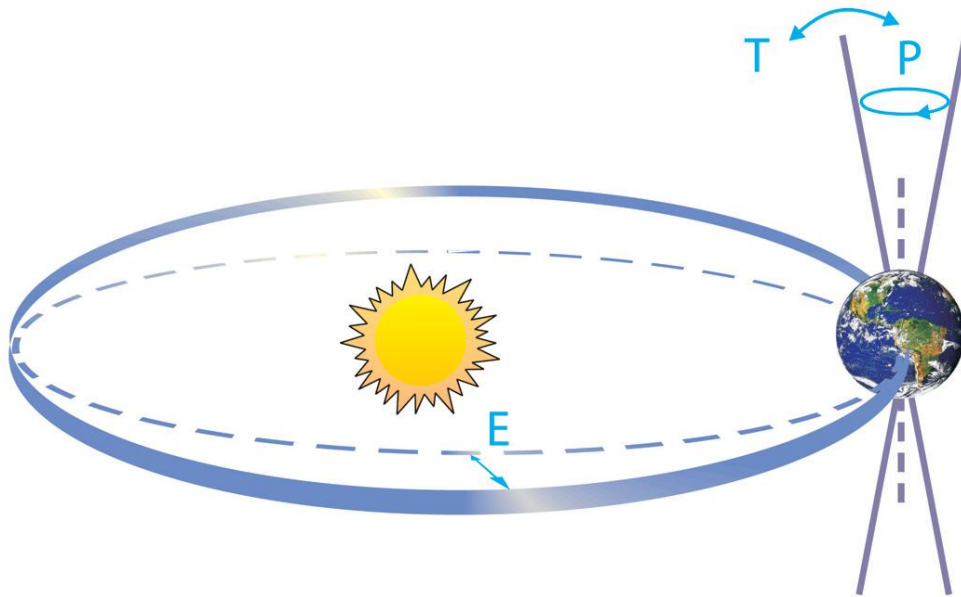


Figure 1.3: The schematic representation of the Earth's orbital changes [source: Rahmstorf and Schellnhuber, 2006]. The alphabets **T**, **P** and **E** stand for changes in the Obliquity or Tilt, Precession and Eccentricity respectively.

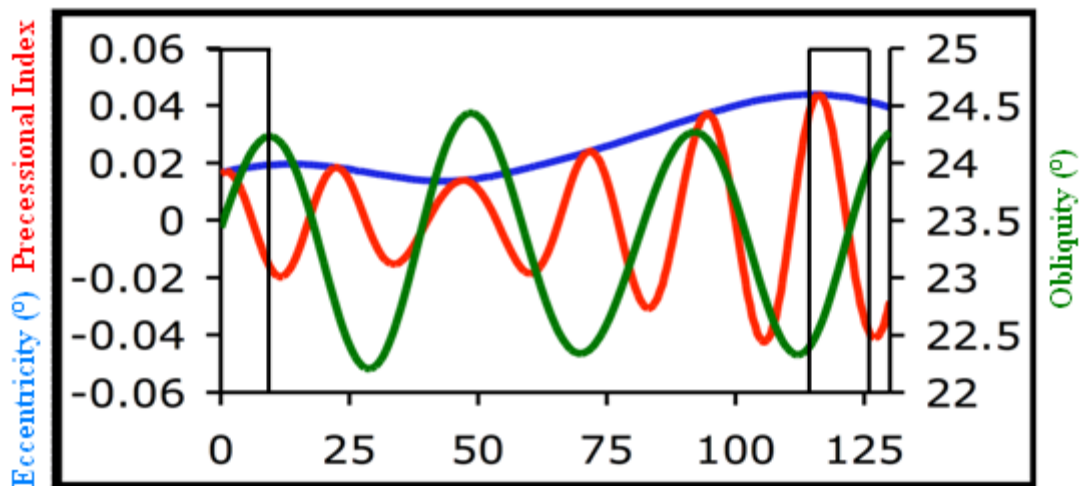


Figure 1.4: The variations of the orbital parameters [obliquity, eccentricity (**E**) and precessional index ($E\sin\omega$)] in the last 130 kyr (Adapted from: Berger, 1978). The ω is the angle between the vernal equinox and perihelion measured in a counter clockwise direction. The two boxes are the Holocene (9.5 kyr-0 kyr) and the Eemian (126 kyr-115 kyr) periods covered in this study.

1.2.2. Precession

The precession (**P**) is a measure of the change in orientation of the Earth's rotational axis (Fig. 1.3). The Earth's precessional cycle takes about 19,000–23,000 years [Hays *et al.*, 1976; Crowley and North, 1991] (Fig. 1.4) causing a slow shift in the dates of perihelion (closest distance between the Earth and the Sun) and aphelion (longest distance of Earth from the Sun) (Fig. 1.5). The magnitude of the seasonal solar radiation increases when the Earth passes through the perihelion while the radiation is minimum at the aphelion. The precession controls the seasonal variations in the hemispheric distribution of solar energy. The associated change in the intensity of seasons results in an overall amplification of the seasonal contrast in one hemisphere and decreasing it in the other hemisphere [Buchdahl, 1999; Rohling *et al.*, 2008].

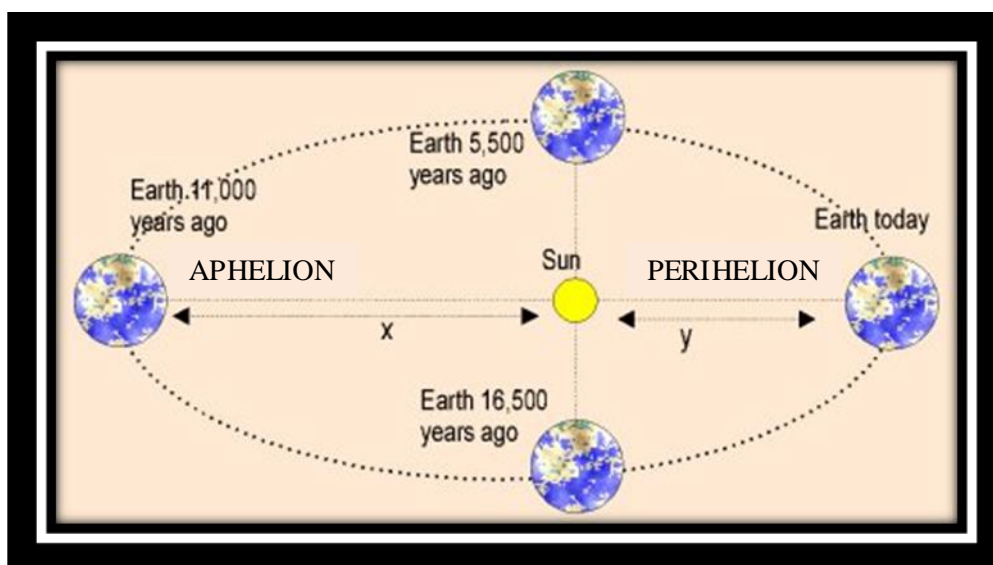


Figure 1.5: Present and past Earth's orbital locations during boreal winter [adapted from Buchdahl, 1999]. The length "x" is the point in the Earth's orbit where the Earth is farthest away from the Sun (at aphelion) while "y" represents the closest distance of the Earth to the Sun (at perihelion).

The modification of the seasonal intensity is caused by the slow shifts in the dates of solstices (longest distance of the Sun to the Equator) and equinoxes (equal lengths of days and nights as the Sun crosses the Equator) [Rohling *et al.*, 2008; Crowley and North, 1991]. This implies that, if the perihelion occurs in mid-June when the Northern Hemisphere (NH) is pointing towards the Sun at high obliquity, the TOA insolation increases in the NH summer when compared to Southern Hemisphere (SH) where the pattern is opposite [Buchdahl, 1999]. Similarly, a rise (reduction) in winter solar radiation in the NH (SH) is associated with the occurrence of perihelion in December (Fig. 1.5). Thus, in the present day climate which is close to a precessional extreme, NH winters are near perihelion (Fig. 1.5), such that the NH (SH) experiences damped (enhanced) seasonal contrast. Within a distance of half a precessional cycle (~11 kyr Before Present, BP) this pattern is reversed, and in between there is less contrast in the seasonal amplitudes of both the NH and SH.

1.2.3. Eccentricity

The Eccentricity (**E**) is a magnitude of the deviation of the shape of Earth’s orbit around the Sun from nearly circular during a low eccentricity (0.005) to a mildly elliptical shape at high eccentricity (0.06) (Fig. 1.3), the current value is about 0.018 (Fig. 1.4) [Buchdahl, 1999]. The two main periods of the eccentricity cycles take ~400,000 and ~100,000 years [Rohling et al., 2008; Jansen et al., 2007]. The fluctuations in the eccentricity forcing modulate the Sun-Earth distance and thereby affecting the total amount of solar radiation received at the top of the Earth’s atmosphere with little influence on the global mean [Jansen et al., 2007]. The difference in the global TOA solar radiation between the perihelion and aphelion could be about 30% at maximum eccentricity (Fig. 1.5) [Goodess et al., 1992]. Basically, the impact of the eccentricity on insolation is mainly through modulation of the amplitude of the precessional effect [Berger, 1988, Rohling et al., 2008]. For instance, a high eccentricity helps to amplify the precessional-induced seasonal and hemispheric contrasts of insolation. According to equation (1.1) below, the eccentricity is estimated by comparing the lengths “x” (at aphelion) and “y” (during perihelion) in Figure 1.5 [Buchdahl, 1999].

$$E = [(x^2 - y^2)^{1/2}]/x \dots\dots\dots (1.1)$$

The overall variations in the astronomical parameters have been calculated (Fig. 1.4) [Berger, 1978] and confirmed by the appearance of their dominant frequencies in paleo reconstructions [Hays et al., 1976] while the existence of the astronomical cycles is also supported by paleoclimate modelling [Timmermann et al., 2007]. For example, the spectral analysis of the SSTs derived from marine sediment ($\delta^{18}O$) within Southern Indian Ocean links the glacial-interglacial alternations of the Quaternary ($\approx 0-2.588$ Ma) ice ages to orbitally-induced changes [Hay et al., 1976].

1.3 The Observed and Modelled Orbitally-Induced Climate Variability

Important insights into the mechanisms driving climate variability and change may be derived from the past climate conditions. These past conditions have been studied beyond the approximately 140 years of instrumental records that are too short for the assessment of long-term climate variability. This makes it possible to distinguish between the natural variability and the human induced (anthropogenic) changes in the present climate using proxy records that are free from modern anthropogenic influence. Similarly, the use of proxies offers opportunity for testing the accuracy of climate models. The assumption that the alternations of the past glacial and interglacial periods are mainly controlled by variations in the orbital parameters can provide the link between the orbital parameters and the climate change. Here, the characteristics of the orbitally-induced SSTs from paleo reconstructions and climate models will be applied in the definitions of the Holocene and the Eemian warm periods and in distinguishing the different time slices used in this study.

1.3.1 Descriptions of the Holocene and the Eemian Climates

(a) The Characteristics of the Holocene Climate

Evidence of Holocene Climate Variability from Paleo-reconstruction

Temperature reconstructed from many proxy records indicates that the warm Holocene climate patterns started at about 11.6 kyr BP [Jouzel *et al.*, 1996] (Fig. 1.6) with growing modern society [Mayewski *et al.*, 2004] and increasing anthropogenic influences [Jansen *et al.*, 2007]. According to paleo reconstruction from Vostok (78.47°S, 106.8°E) ice core in Antarctica, the transition from about 21 kyr BP (Fig. 1.6) to the early-Holocene (9.5 kyr BP in this study) is characterized by melting of glaciers which constitute the major influence on the climate change during the early-Holocene [Davis and Brewer, 2009]. The mean temperature in the early Holocene gradually declines over the Holocene period. On the global scale, the temperature during the mid-Holocene (6 kyr BP in this study) is estimated to be about 1°C to 2°C warmer compared to today, probably due to increased summer temperature during the mid-Holocene than today [Buchdahl, 1999]. The paleo data from the mid-northern latitudes revealed long-term reduction in the region's SST from the early-Holocene to the late-Holocene period (0 kyr BP in this study) [Jansen *et al.*, 2007; Johnsen *et al.*, 2001; Marchal *et al.*, 2002; Andersen *et al.*, 2004; Kim *et al.*, 2004; Kaplan and Wolfe, 2006].

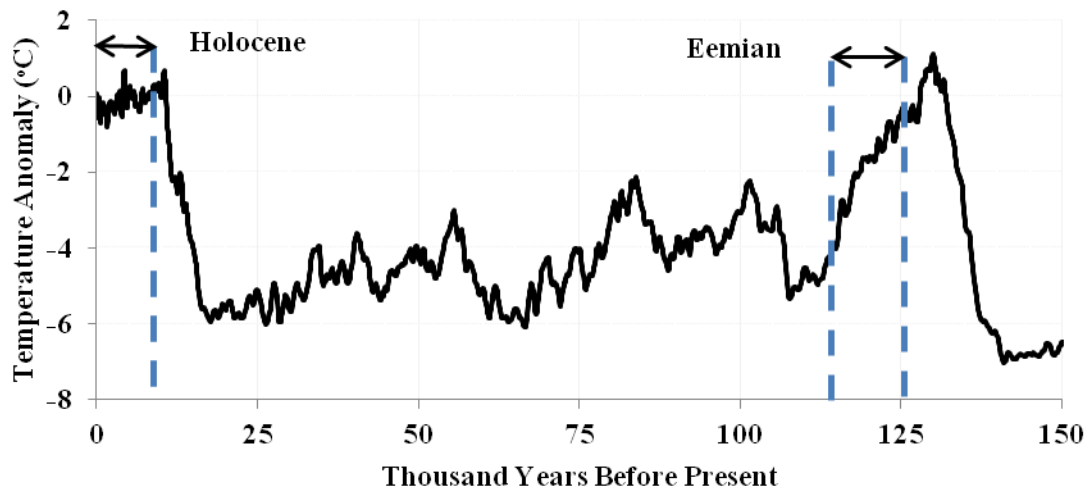


Figure 1.6: The temperature anomaly relative to the present over the last 150,000 years estimated from Vostok (78.47°S, 106.8°E) ice core deuterium measurements (Russian Vostok base in Antarctica; source: Lorius *et al.*, 1995). The arrows and the blue broken lines show the periods covered in this study of the Eemian (126K to 115K) and the Holocene (9.5K to 0K).

In addition, the observed trends in the sea level [Fairbanks, 1989] and oxygen isotopic composition of polar ice sheets [Grootes *et al.*, 1993] proved that the Holocene period is warm [Buchdahl, 1999] and relatively more stable than the Eemian climate (Fig. 1.6) [Lorenz *et al.*, 2006]. A northward expansion of temperate forest and glacial melting [Bigelow *et al.*, 2003; Kaplan *et al.*, 2003] deduced from global pollen-based reconstructions [Prentice and Webb, 1998; Prentice *et al.*,

2000] and microfossils [MacDonald *et al.*, 2000] is in agreement with the warming trend in the mid-Holocene [Jansen *et al.*, 2007]. The human death and the collapse of Maya civilization (near the present day Mexico) has been attributed to drought between 1.2 kyr-1 kyr B.P. [Hodell *et al.*, 2001; Gill, 2000] while that of Greenland's Norse colonies at about 600 calendar year is linked to polar cooling [Buckland *et al.*, 1995; Mayewski *et al.*, 2004]. However, paleoclimatologists are still unable to find natural climatic explanations for the present-day warming since the decrease in summer insolation from the northern hemisphere in the last few millennia should favour ice buildup [Jansen *et al.*, 2007; Hoyle, 1981].

Evidence of Holocene Climate Variability from Model Study

A slight increase in the mean global temperature (below 0.4°C) caused by changes in the seasonality of orbital forcing has been simulated in the 6 kyr BP (mid-Holocene) climate forced by variations in the orbital parameters [Masson-Delmotte *et al.*, 2005]. In addition, the modelled intensification of the North Australian, Indian and southwest American monsoons during the mid-Holocene [Harrison *et al.*, 2003; Liu *et al.*, 2004; Zhao *et al.*, 2005] has been attributed to the influence of orbital forcing [Braconnot *et al.*, 2004; Zhao *et al.*, 2005]. Braconnot *et al.* [2007, and the references therein] reported an insolation induced strong African monsoon in the mid-Holocene simulation due to ocean feedbacks induced by the inter-hemispheric gradient of SST over Atlantic Ocean which allows inland advection of moist air. However, a mid-Holocene reduction of the monsoon is found in the Indian Ocean due to increase in the summer sea surface temperature and the associated strong deep convection over the Indian Ocean compared to the continent [Liu *et al.*, 2004; Braconnot *et al.*, 2007]. Also, an early to mid-Holocene enhanced precipitation has been reconstructed from Lake and vegetation changes in North Africa [Jolly *et al.*, 1998] while an orbitally-induced warming of NH during the early-Holocene, which reduces thereafter over the Holocene has been reported in the model study by Braconnot *et al.* [2008].

(b) *The Characteristics of the Eemian Climate*

Evidence of Eemian Climate Variability from Paleo-reconstruction

The proxy data indicate that the Eemian period occurred between 130 ± 1 kyr BP to $116 \text{ kyr BP} \pm 1$ kyr BP (Fig. 1.6) [Stirling *et al.*, 1998; Jansen *et al.*, 2007]. The period is characterized by reduced global glacial ice [Stirling *et al.*, 1998] than now and the regional warming induced by the orbital forcing is consistent with reduction in the ice extents [Kukla *et al.*, 2002] (Lorius *et al.*, 1995; Fig. 1.6). An orbitally-induced higher global temperature of about 3°C to 5°C compared to the present was estimated from the ice core data within the Greenland and Antarctica for the early-Eemian (126 kyr BP in this study) [Watanabe *et al.*, 2003; NGRIP, 2004; Landais *et al.*, 2006]. According to IPCC [2007] report, the warming might be responsible for the reduction in the polar ice with corresponding

rise in global sea level. This is further supported by the observation from coastal sedimentary deposits and Tropical coral which suggests that the global sea level is likely 4-6 m higher in the 125 kyr BP compared to the present [IPCC, 2007; Rostami *et al.*, 2000; Muhs *et al.*, 2002].

Furthermore, the evidence from paleofauna obtained from New Zealand reveals a high temperature in the late-Eemian (115K in this study) which is consistent with the latitudinal pattern of orbital forcing [Marra, 2003]. An orbitally-induced cooling in the 122 kyr BP (mid-Eemian in this study) with glacial occurrence at about 118 kyr BP has also been reported in the temperature reconstructed from the Greenland ice core [Sirocko *et al.*, 2005, and the references therein]. The late-Eemian was mostly warmer (Fig. 1.6) and wetter compared with today in the NH with a possible expansion of forest. The Eemian is believed to be fairly stable like Holocene but with an overall warmer climate due to the intensified orbital forcing compared to the present climate (Fig. 1.4). However, little is known about the model study of Eemian. In general, findings have led to the assumption that the highest global temperature in the last 200 kyr BP might have occurred during the Eemian while this temperature pattern and the late Quaternary (0-20 Kyr BP) temperature could serve as analogous for studying future climate warming under rising greenhouse gas [Montoya *et al.*, 2000].

1.3.2 Observed and Modelled ENSO Variability

Several reconstructions of the Holocene climate (last 10 kyr BP) agree that ENSO amplitude was weaker during the early to mid-Holocene compared to the present climate [Jansen *et al.*, 2007; Shulmeister and Lees, 1995; Gagan *et al.*, 1998; Rodbell *et al.*, 1999; Tudhope *et al.*, 2001; Moy *et al.*, 2002; McGregor and Gagan, 2004]. Evidence comes from layers of inorganic debris deposits in lake sediments from Ecuador, which indicates that a switch toward more frequent strong El Niños started around 7 kyr BP [Rodbell *et al.*, 1999] while amplification in the last few thousand years has also been confirmed in the high resolution paleo records (corals, archaeological middens, lake and ocean sediments) from several regions [Jansen *et al.*, 2007 and the references therein]. Also, replacement of tundra by boreal forest at middle to high latitudes of the NH has been observed in the mid-Holocene proxy data reported by Prentice *et al.* [2000].

The reconstructions of ENSO variability using time slices covering the last 120 kyr BP from different locations reveal the existence of active ENSO event around 125 kyr BP with a possible reduction in the ENSO activity between early to mid-Holocene [Timmermann *et al.*, 2007 and the references therein]. In the Indo-Pacific Warm Pool, $\delta^{18}\text{O}$ and Sr/Ca data from corals, recording salinity (precipitation) and temperature variations, respectively, have shown increasing ENSO-related fluctuations over the Holocene [Tudhope *et al.*, 2001]. The data show considerably higher variability at modern times compared to the last glacial and interglacial periods (~20 and 130 kyr BP) [Tudhope *et al.*, 2001; Moy *et al.*, 2002; Gagan *et al.*, 2004]. Similarly, pollen records from northern Australia

show a period of less variable conditions around 4 kyr BP, indicative of weaker ENSO variability, followed by a switch back to a drier (El Niño-like) state thereafter [*Shulmeister and Lees, 1995*].

Furthermore, model simulating the climate of the Holocene supports the tendency of damped ENSO variability during the mid-Holocene [*Clement et al., 2000; Liu et al., 2000; Otto-Bliesner et al., 2003; Brown et al., 2006*] which is mostly explained by the effect of precession-induced enhancement of the Asian Monsoon [*Zheng et al., 2008; Kutzbach et al., 1997*]. Several studies on the response of Tropical climate to changes in the orbital forcing using coupled ocean-atmosphere model [*Clement et al., 1999*] and general circulation models [*DeWitt and Schneider, 2000; Liu et al., 2000; Otto Bliesner et al., 2003*] reveal an early to mid-Holocene reduction in ENSO variability which agrees with paleo reconstruction [*Tudhope et al., 2001; Moy et al., 2002*]. Intensification of the ENSO between early-Holocene and present has been integrated from GCMs [*Jansen et al., 2007*]. Furthermore, many model studies and data point to La Niña-like mean state in the Tropical Pacific before the mid-Holocene [*Clement et al., 2000; Liu et al., 2000; Kitoh and Murakami, 2002; Otto-Bliesner et al., 2003; Liu, 2004*]. In addition, model simulations with atmosphere and Slab Ocean are also in agreement with a La Niña-like mean condition during the mid-Holocene [*Shin et al., 2006*].

In general, the Eemian experienced a warmer climate compared to today [*Jansen et al., 2007*] probably with significant reduction in the NH ice volume [*Stirling et al., 1998; Otto-Bliesner et al., 2006*]. The Holocene and the Eemian periods are within the well-dated 150 kyr interval over which a meaningful test of the orbital theory could be made with a good accuracy in the geological chronology [*Hays et al., 1976*]. However, paleo records are less sufficient in the Eemian compared to the Holocene period [*Leduc et al., 2010*]. Also, the available paleo proxies often do not permit the reconstruction of seasonal to interannual variability, which is mainly due to lack of sufficient temporal resolution and/or proxy sensitivity while the uncertainties in the reconstructed climate become high with time into the past due to increasingly limited spatial coverage [*IPCC, 2007; Leduc et al., 2010*]. Therefore, forming a robust link between ENSO and the mean state could allow proxy records with coarse time resolution to provide a strong constraint on reconstructions of ENSO during past climates.

1.4 Tropical Pacific Climate

The focus on the Tropical Pacific is important since the region is capable of organizing [*Clement et al., 1999*] and influencing global climate due to its large size. For instance, the Pacific Ocean constitutes the largest part of the global oceans that are playing critical roles in the heat distribution by ocean current which drives the global circulation and transport heat from the warm Tropics to the cool Polar Regions. The ocean also serves as a strong stabilizing force on the Earth's climate system by storing heat, the heat is later released into the atmosphere as latent energy while the latent heat in evaporated water is also released during cloud and precipitation formation [*Buchdahl, 1999*] thereby affecting biological diversity. In addition, the Equatorial Pacific is important for seasonal forecasting

while the changes in the mean state of the region or ENSO statistics under global warming will have impact on the climate of several locations globally [Latif *et al.*, 2001].

1.4.1 The Annual Mean State

The Tropical Pacific is influenced by the thermally-induced wind driven circulations which include the North Equatorial Current, NEC and South Equatorial Current (SEC) that transport water westward [Fig. 1.7; Tomczak *et al.*, 2003]. Sandwiched between the NEC and SEC is the Equatorial Counter Current (ECC) that partly return the westward flow back to the east with higher (weaker) strength of the ECC (SEC) during an El Niño year [Taft and Kessler, 1991; Kessler and McPhaden, 1995] compared to the La Niña year. Also, the strength of Equatorial Undercurrent (EUC) weakens during an El Niño year in the Central Pacific, lowering the supply of cold upwelling water (not shown) [Kessler and McPhaden, 1995]. Similarly, the currents from the western Pacific serve as a source of flux into the Indonesian Throughflow (ITF) and the Indian Ocean where the vertical exchange of the dense, cold and salty water with the lighter, warmer and fresher water from the Pacific Ocean affects the global thermocline circulation. For instance, the transport of warm water through the ITF increases under strong trade winds in a La Niña year while the reverse conditions occur during an El Niño event [Wainwright *et al.*, 2008] with low temperature of thermocline and surface flow [Newton *et al.*, 2011].

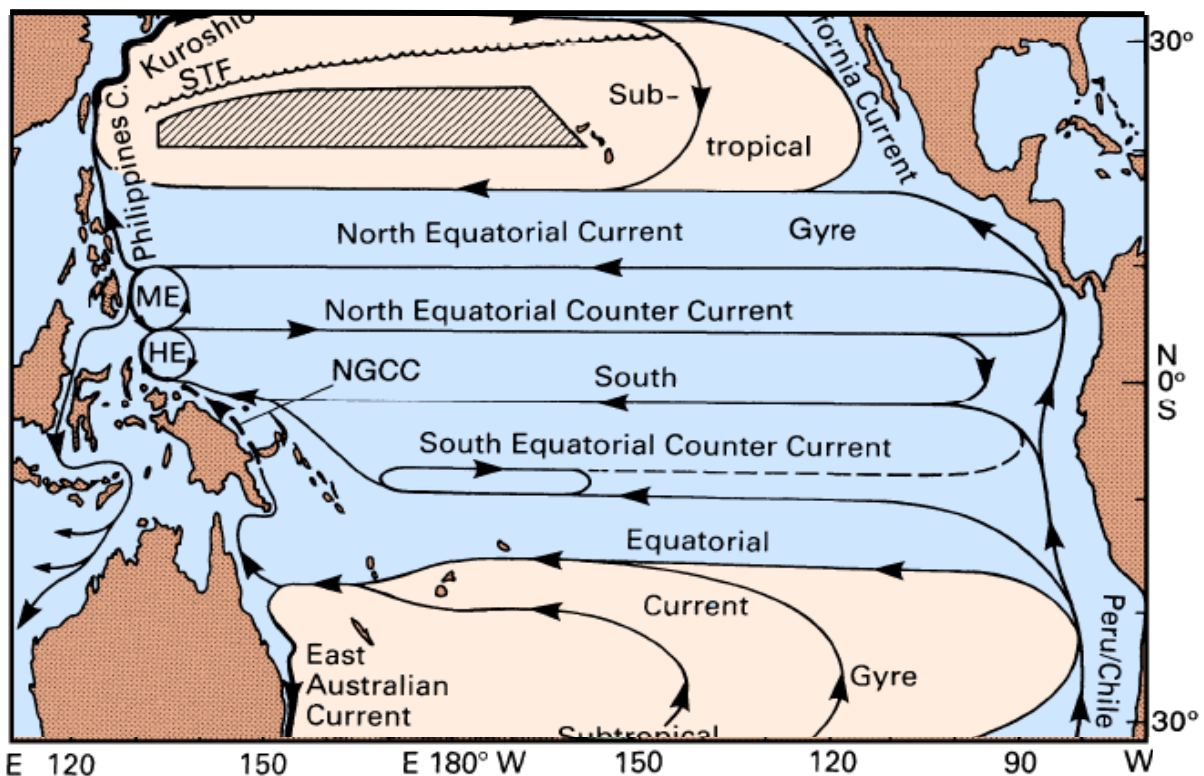


Figure 1.7: The main surface currents over the Pacific Ocean (arrows indicate the direction of flow) [adapted from: Tomczak *et al.*, 2003]. Below are the details of the abbreviations in the Figure: Mindanao Eddy (ME), Halmahera Eddy (HE), Subtropical Front (STF), and New Guinea Coastal Current (NGCC).

The mean state of the Tropical Pacific is characterized by a warm pool in the west and a cold tongue in the east (Fig. 1.8). The warm pool has been defined as an area of strong convection, a closed region with SST of about 28°C [Zhang and Chen, 2008; Ho et al., 1995] and above [McPhaden and Picaut, 1990]. According to the HadISST (1950-1999) observation [Rayner et al., 2003], the annual mean SST exceeds the 28°C in the western Pacific and it is below 25°C in the east (Fig. 1.9). The changes in the temperature pattern over the Tropical Pacific under the air-sea interactions [Dijkstra and Neelin, 1995] is strongly influenced by fluctuations in the strength of the Walker Circulation (WC) and Hadley Circulation (HC) [Collins et al., 2010] (Fig. 1.8, Fig. 1.10) due to variations in the trade wind (Fig. 1.7, Fig. 1.8). The normal condition involves moderate increase in the strength of the WC and HC circulations, this strengthens the westward flowing trade winds across the Tropical Pacific with the WC dominating over the HC along the Equator [Collins et al., 2010; Latif and Keenlyside, 2009]. There is accumulation of warmer surface water in the Western Pacific compared to the Eastern Pacific which cools under the influence of upwelling of cold thermocline water in the region (Fig. 1.8). Also, the ascending arm of the WC from the western Pacific warm pool, WPWP (the heat source) diverges in the mid-troposphere and flows eastward where it finally descends over the cold Eastern Pacific water [Collins et al., 2010] (the heat sink) (Fig. 1.8) to complete the circulation. The overall circulation maintains a warm pool structure in the Western Pacific while a cold tongue dominates in the Eastern Pacific.

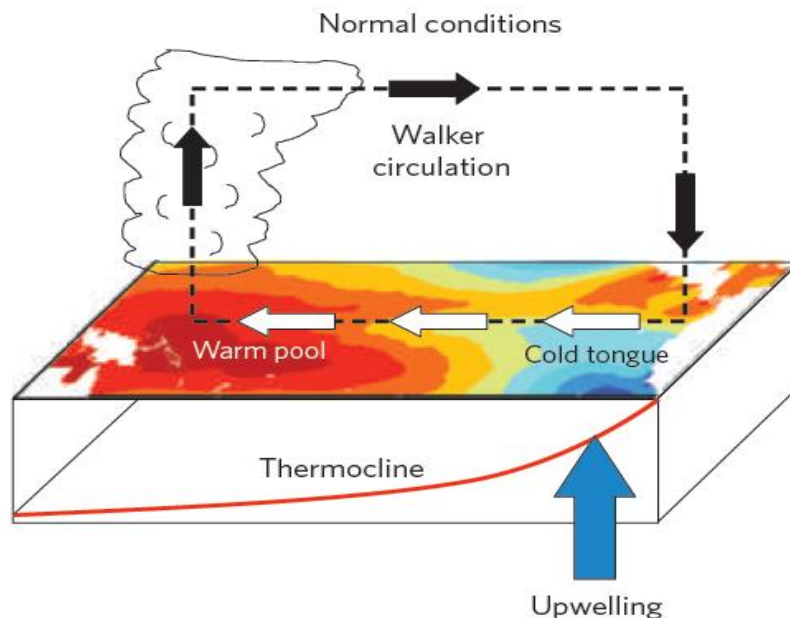


Figure 1.8: The schematic representation of the mean atmospheric and oceanic conditions of the Tropical Pacific and their interactions during Normal condition [source: Collins et al., 2010]. The warm regions are in red colour while the blue stands for the cold areas. The trade winds and Walker circulation are shown in white arrows and the descending black arrows respectively. The ascending black arrow is associated with rainfall from the mean position of convection while the blue upward arrows stand for upwelling. Note that the size of the arrows (white and blue) is a measure of the strength of the variables they are representing.

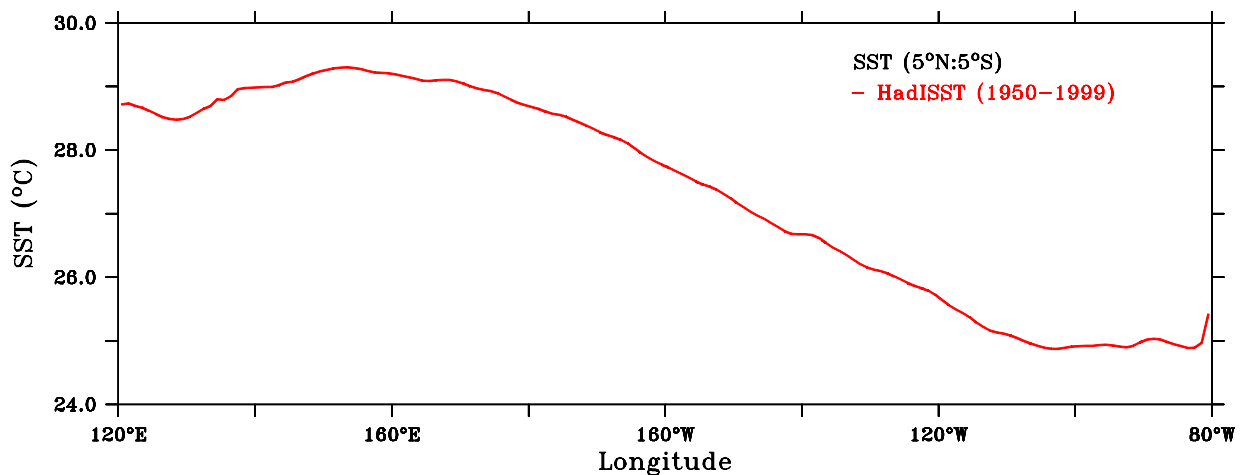


Figure 1.9: The annual mean SST (°C) over the Equatorial Pacific (5°N:5°S) from the Hadley Centre Sea Ice, HadISST (1950-1999) observation.

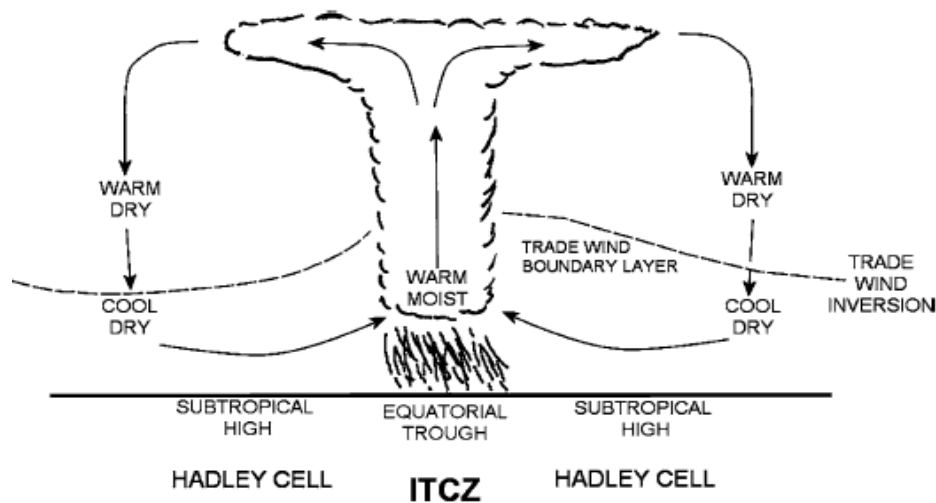


Figure 1.10: Schematic representation of Hadley Cell and ITCZ position (source: Nicholson, 2009).

The contribution of HC to the changes in the mean state of the Tropical Pacific is associated with the stronger SST over the Tropical Pacific compared to the subtropics. For instance, the warm Tropical Pacific air rises to create a band of low pressure and strong convection called the intertropical convergence zone (ITCZ) near the Equator [Philander *et al.*, 1996] (Fig. 1.10). The ITCZ position is sustained in a more northern location in the east by the enhanced heating from the larger land mass in northern part of the region compared to the west. The rising Tropical Pacific warm air flows poleward near the tropopause (the atmospheric boundary between the troposphere and the stratosphere) within the Hadley cell and turns eastward under Coriolis force, which deflects winds to the right (left) in the NH (SH). The air later descends over the subtropical regions (within 30°N and 30°S) before returning equator-ward at the surface where it is deflected to the west by the Coriolis effect to form the trade

winds (easterlies) [Xie *et al.*, 2007]. The trade wind strengthens the WC, raising the ocean surface temperature (Fig. 1.9), precipitation and the Sea Surface Height (SSH) in the west where the Sea Level Pressure (SLP) is lower compared to the east (Fig. 1.8).

1.4.2 The Seasonal Cycle

According to the Tropical Atmosphere Ocean (TAO) data [McPhaden, 1998], an insolation-induced annual cycle of SST is created over the eastern Tropical Pacific while a semi-annual cycle dominates in the western Tropical Pacific (Fig. 1.11a). Although the Sun crosses the Tropic twice in a year, the occurrence of annual cycle of SST in the eastern Pacific is associated with the stronger upwelling-induced dampening of the SST in the east compared to the west. The warm phase of the annual SST cycle is strongest in March over the eastern Pacific while the cold phase of the annual SST cycle is in September [see Xie *et al.*, 2007]. A northward migration of the ITCZ location and the associated SST after March is accompanied by intensified southerly cross Equatorial wind induced by seasonal changes in the insolation [Mitchell and Wallace, 1992; Xie, 1994; Xie *et al.*, 2007] over the eastern Pacific. This northward shift of the ITCZ position raises the north-south SST asymmetry in the east since the cross-equatorial winds weaken in the north with respect to the south. The strengthening of the meridional SST asymmetry is further aided by the weak mixing and formation of low-level stratus cloud that amplifies the reflection of solar radiation over the cold eastern Pacific [see Timmermann *et al.*, 2007]. The overall air-sea interaction generates the positive feedback (Bjerknes) which leads to the formation of coupled annual cycle in the eastern-central region of the Equatorial Pacific. The north-south asymmetry diminishes in the east along with the strength of the annual cycle of the SST and the upwelling during the southward migration of the ITCZ position [Xie *et al.*, 2007].

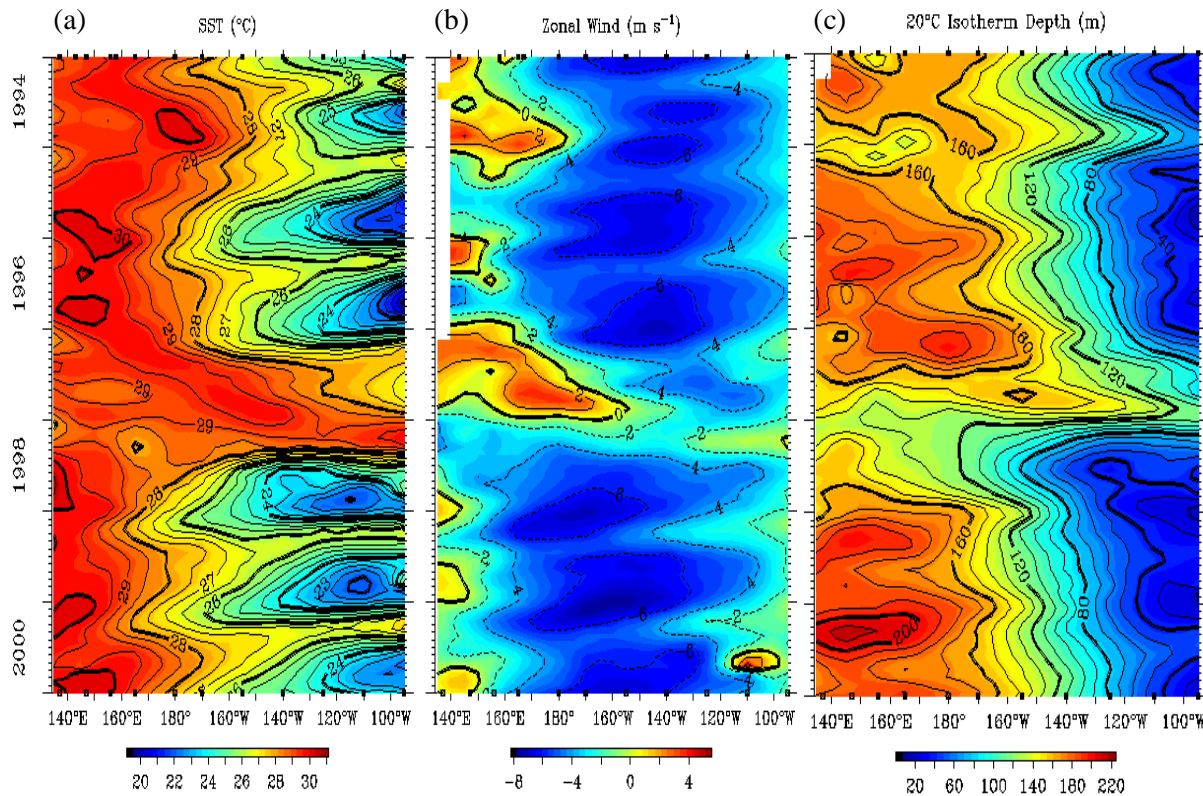


Figure 1.11: The Time versus longitude sections of the (a) mean SST ($^{\circ}\text{C}$), (b) surface zonal wind (m/s) and (c) 20°C thermocline (isotherm) depth (m) from January 1994 to December 2000 and averaged over $2^{\circ}\text{S}:2^{\circ}\text{N}$ from the monthly Tropical Atmosphere Ocean (TOA) data. The positive winds are westerly while negative winds are easterly (Source: <http://www.pmel.noaa.gov/tao/jsdisplay>).

The zonal asymmetry of the SST [Dijkstra and Neelin, 1995; Sun and Liu, 1996] and the ENSO development [Neelin *et al.*, 1998; Wang and Picaut, 2004] are maintained by the interactions between the eastern cold tongue and the easterly winds over the Equatorial Pacific [Xie *et al.*, 2007]. A La Niña-like mean state is accompanied by northward shift of the ITCZ in the east where the upwelling increases the seasonal intensification of the trade winds (Figs. 1.11a, b, c). However, there is weakening of the wind and the upwelling of cold Z20 water as the ITCZ shifts southward during an El Niño-like mean state (Figs. 1.11a, b, c) [Mitchell and Wallace, 1992]. A typical example is seen in the 1997/1998 El Niño event [McPhaden, 1999] which is characterized by eastward expansion of the warm pool, collapse of the trade wind and reduced upwelling due to deepening of the Z20 depth over the eastern Pacific. The existence of a tight coupling between ENSO and the seasonal cycle of SST fits the earlier report [Xie *et al.*, 2007; Jin *et al.*, 1994; Chang *et al.*, 1994; Li and Hogan, 1999] which proposed that changes in the mean state and the seasonal cycle of the Tropical Pacific affect the period, seasonality and the amplitude of the ENSO events. Thus, accurate model studies of the ENSO events require reasonable simulation of the annual cycle in the eastern Pacific [see also Xie *et al.*, 2007].

1.4.3 The Interannual Variability

On the interannual time scale, the TAO data show that the eastward extension of warm pool peaks in the late boreal summer (Fig. 1.11a) as the easterlies weaken (Fig. 1.11b) with the flattening of the west-east thermocline (20°C) gradient (Fig. 1.11c). Using the 1997/1998 El Niño event as a case study [McPhaden, 1999], the eastward expansion of the warm pool raises the positive SST anomalies in the east while the west cools slightly (Fig. 1.12a). The resulting reversal of the trade winds in the western-central Equatorial Pacific deepens the thermocline in the east while it slightly shoals in the west (Figs. 1.12b, c). The El Niño event is terminated with the return of the normal condition when the trade winds strengthen moderately in the eastern Pacific while the patterns are reversed during a La Niña event. In favour of the observation, many model studies suggested that the ENSO variability is an inverse function of the mean trade wind strength in the central Pacific as well as of the relative strength of the seasonal cycle of the SST [Guilyardi, 2006] in the EEP. For example, Timmermann *et al.* [2007] linked the changes in the seasonal cycle of the SST, the modulation of the strength of the SST annual cycle and ENSO to precessional cycle.

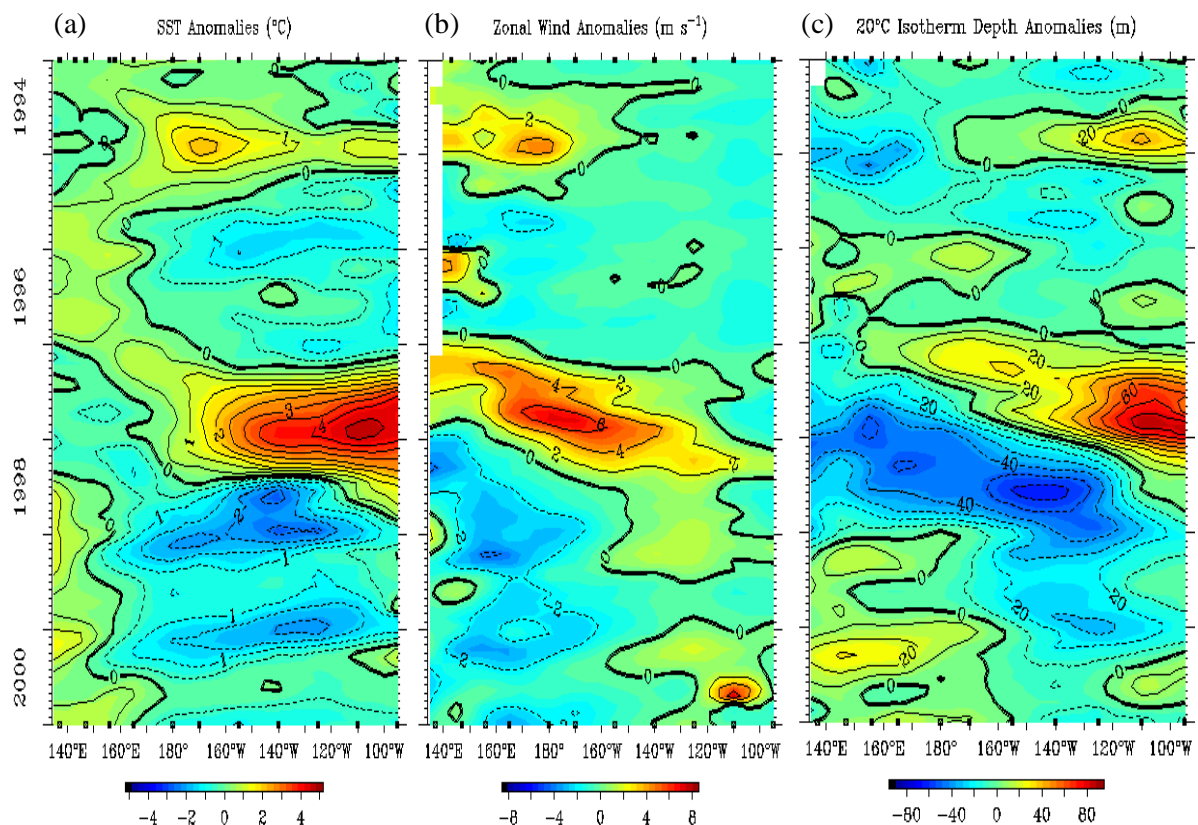


Figure 1.12: The time versus longitude sections of the anomalies in the observed (a) SST ($^{\circ}\text{C}$), (b) Surface Zonal Wind (m/s) and (c) thermocline (Z_{20}) depth (m) from January 1994 to December 2000. The values are estimated over $2^{\circ}\text{N}:2^{\circ}\text{S}$ of the Tropical Pacific using the monthly TAO data. The Positive winds are westerly while positive 20°C isotherm stands for deeper thermocline depth compared to the normal condition (Source: <http://www.pmel.noaa.gov/tao/jsdisplay>).

The La Niña Condition

During a La Niña event, the trade wind amplifies above the mean strength in a normal condition (Fig. 1.8, Figs. 1.2a-c) across the Tropical Pacific. This boosts the upwelling of cold thermocline water in the eastern Pacific and raises the accumulation of warmer water in the west. For instance, these changes are seen in the 1998/1999 La Niña event and during the weak La Niña episode of 1995/1996 [McPhaden *et al.*, 1999]. According to the observed interannual variability from the Global Precipitation Climatology Project, GPCP (1994-2000) data [Adler *et al.*, 2003], the La Niña event is characterized by a westward shift of the region of strong convection with higher precipitation in the western Pacific compared to the east (Fig. 1.13a). The accompanying increase in the trade winds results in the amplification of the SSH in the western Pacific than in the east (not shown) where the Z20 depth is shallower (Fig. 1.12c). Overall, the north-south SST meridional gradient amplifies in the eastern Pacific while the west-east SST gradient increases under the strong easterlies (Figs. 1.11a–b). In addition, the observed mean SLP estimated from the National Centers for Environmental Prediction NCEP Reanalysis data [Kanamitsu *et al.*, 2002] rises in the east and lowers in the western Pacific (Fig. 1.13b) while the resulting west-east pressure gradient drives the southerly cross Equatorial winds.

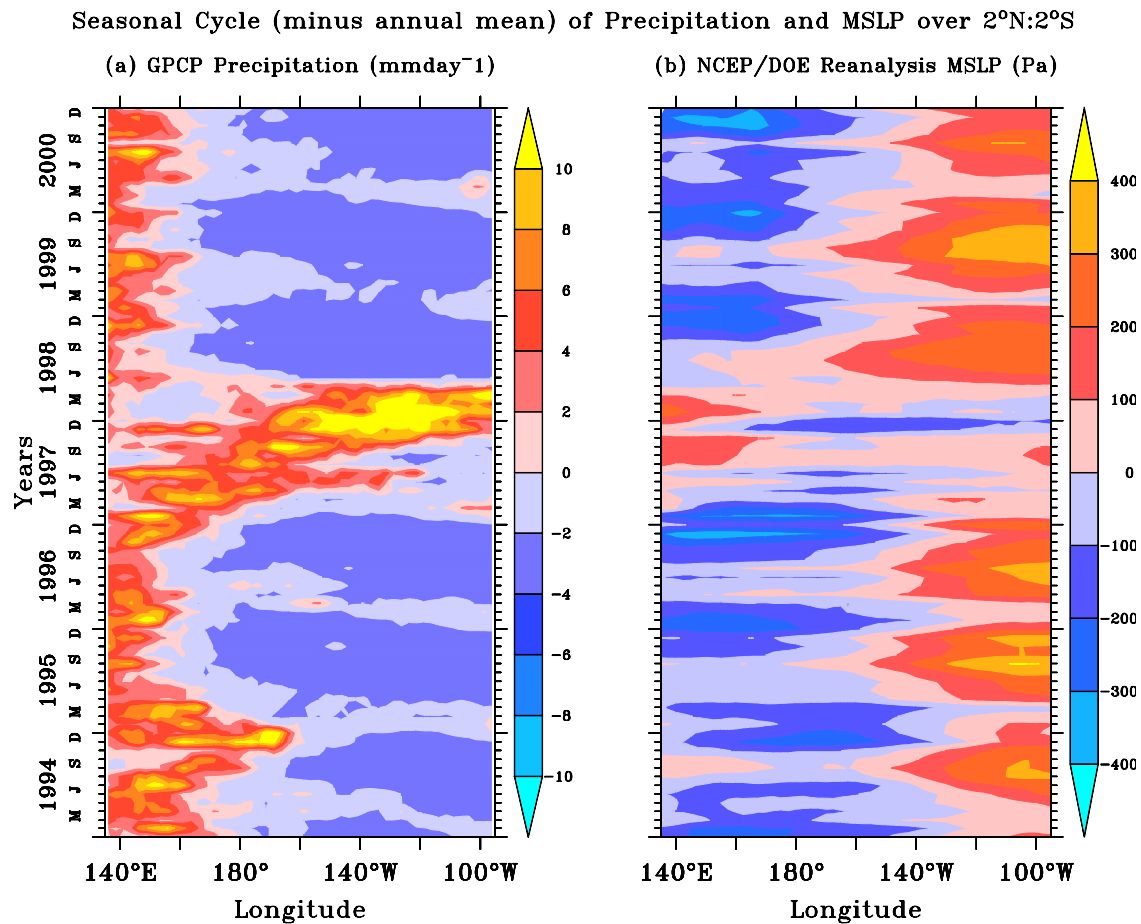


Figure 1.13: Hovmoeller diagrams of the interannual variability in the data from the (a) National Oceanic and Atmospheric Administration (NOAA) Global Precipitation Climatology Project (GPCP) monthly Precipitation (1994-2000) (mmday^{-1}) and (b) National Centers for Environmental Prediction/Department of Energy (NCEP/DOE) AMIP II Reanalysis (2) monthly averages of the Mean Sea Level Pressure, MSLP (1994-2000) (Pa) over 2°N:2°S. The anomalies in (a, b) are defined as departures from the annual cycles. The precipitation data is from the Global Precipitation Climatology Project (GPCP version 2.2). Note the changes in direction of y-axis compared to figures 1.11 and 1.12. (Data source: <http://www.esrl.noaa.gov/psd/data/gridded/tables/monthly.html>)

The El Niño Condition

The above characteristics of a La Niña condition reverses during an El Niño event. The El Niño-like mean state is associated with eastward extension of the warm pool as the thermally-induced WC and the trade winds weaken in the eastern Pacific (Fig. 1.14). This creates anomalously high SSTs in the east while the western Pacific cools (Fig. 1.12a) partly because of the evaporative heat loss and the mixing of subsurface cold water [McPhaden, 1999]. The changes in the SST result in shifting of the region of strong convection eastward toward the central Pacific (Fig. 1.13a), causing a reduction in the west-east SST contrast as the west-east Z20 gradient weakens over the Tropical Pacific (Fig. 1.14, Fig. 1.11c) [Latif and Keenlyside, 2009]. An intensification of El Niño strength is accompanied with the weakening (strengthening) of the mean SLP in the eastern (western) Pacific while the SSH increases (reduces) in the region as revealed by the 1997/1998 El Niño event (Figs. 1.12c). Due to the positive

feedback induced by the air-sea interaction, the resulting instability increases as the Z20 depth goes deeper in the east with further weakening of the west-east SST gradient [Neelin *et al.*, 1998, Collins *et al.*, 2010]. In general, the interactions between the mean SST, Z20 depth and the mean wind stress seem to dominate the development of both cold and warm phases of the ENSO event [Latif and Keenlyside, 2009].

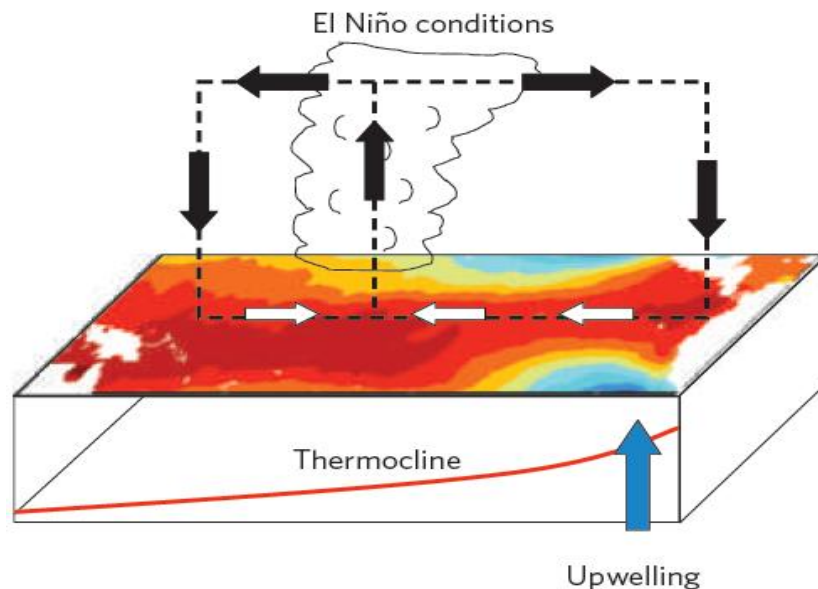


Figure 1.14: The schematic representation of the mean atmospheric and oceanic conditions of the Tropical Pacific and their interactions during an El Niño event [source: Collins *et al.*, 2010]; description as in Figure 1.8.

The ongoing efforts to shed more lights on the mechanisms governing ENSO variability has produced some important theories including Bjerknes feedback, recharge-discharge oscillator and delayed oscillator which are briefly discussed below.

Bjerknes Feedback

This is a theory formulated by *Bjerknes* [1969] to link the mechanisms involved in the El Niño and southern oscillation. It is a positive feedback loop which suggests that the west-east SST contrast is maintained by easterly trade winds across the Tropical Pacific, the associated surface zonal current and the upwelling in the east (Fig. 1.15). An intensification of the easterlies over the Tropical Pacific results in the amplification of upwelling of cold SST in the eastern Pacific as the Z20 depth shoals in the east while the west warms with deepening of the Z20 depth in the region. There is westward displacement of the atmospheric convection as the trade winds strengthen under the influence of increasing WC and rising west-east SST gradient. Under a La Niña-like mean state in the Tropical Pacific, the instability increases with shoaling of the Z20 depth in the east while the west-east SST contrast further intensifies [Neelin *et al.*, 1998, Collins *et al.*, 2010]. The feedbacks may change in

response to global warming-induced by changes in the mean state, leading to different ENSO dynamics [Latif *et al.*, 2009]. For instance, during an El Niño-like mean state in the Tropical Pacific, the positive feedback operates in the opposite direction such that the Z20 depth deepens in the eastern Pacific due to weakening of the easterlies while the west-east SST gradient lowers.

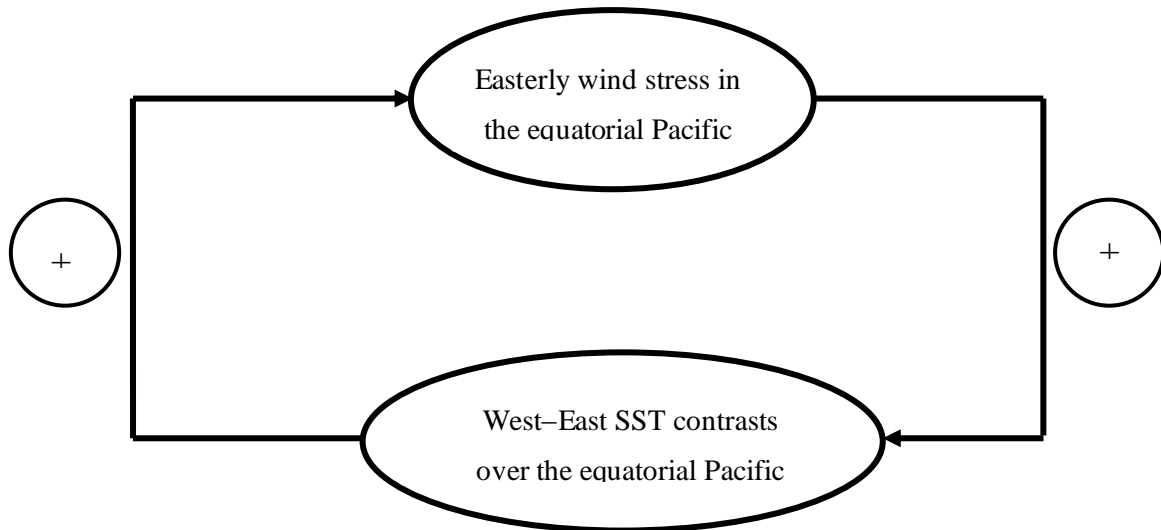


Figure 1.15: Schematic illustration of the Bjerknes feedback. It is a positive feedback - the positive signs on the arrows indicate that an intensification of the easterly wind stress lead to an increase in the west-east contrast and vice versa.

The Recharge-discharge Oscillator

As shown in Figure 1.16a, an initial positive SST anomaly (SSTA) in the eastern Pacific raises the westerly wind stress (τ) anomaly over the western and central Pacific. This initiates the ENSO warm phase (El Niño) in accordance with the Bjerknes [1969] feedback as the Z20 depth (h) goes deeper in the east compared to the west where it slightly shoals. At the peak of the event, transport of water masses out of the Equatorial region is maximum, marking the height of the discharge of Equatorial heat content due to a decrease in the zonal mean Z20 depth and reduced meridional circulation over the Tropical Pacific. The Cold SSTA starts to build over time as the thermocline depth adjusts toward the transition phase (Fig. 1.16b) with attenuation of the positive SSTA in response to reduction of the Z20 depth in the east in addition to latent heat loss to air-sea heat exchange. The decrease in the thermocline depth over the eastern Pacific results in discharge of ocean heat content and the initiation of transition into the normal state as the wind stress amplifies to the normal strength in the east [Ströh, 2007] (Fig. 1.146).

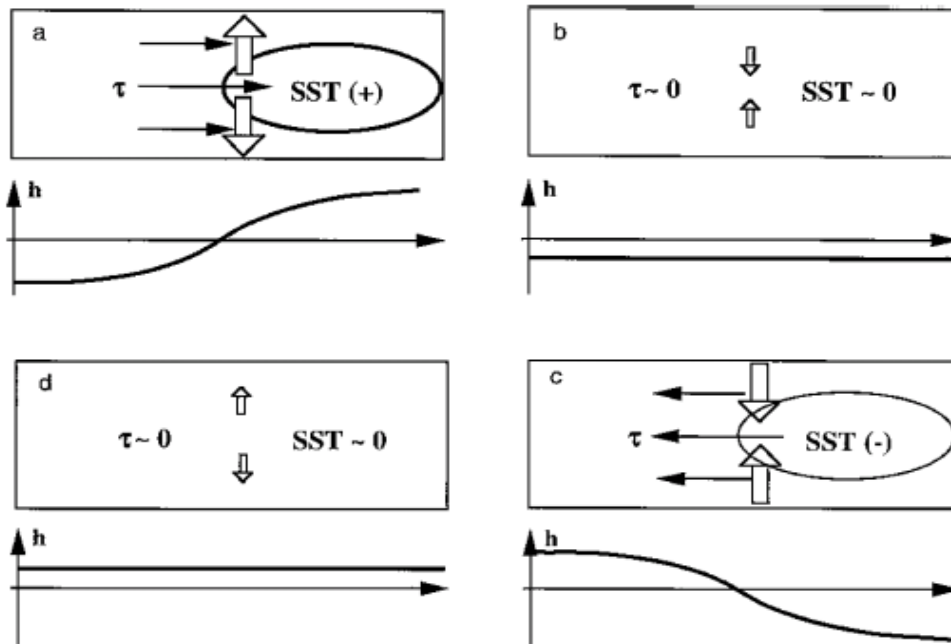


Figure 1.16: Schematic representation of the four phases of the recharge-discharge oscillation mechanism in the Equatorial Pacific: the (a) warm phase, (b) transition from warm to cold phase, (c) cold phase, and (d) the transition from cold to warm phase. The thin filled arrows are the wind stress (τ) anomaly while the thick empty arrows represent the recharge/discharge of Equatorial heat content. The elliptical cycle stands for the SST anomaly and graph shows the distribution of thermocline depth anomaly (h , positive downward) [Source: Jin, 1997].

The initial instability is amplified under Bjerknes feedback. The amplification is associated with the strong cooling over the Equatorial Pacific due to increase in the upwelling in the east and evaporative cooling while the easterlies intensify with an influx of warm surface water (Fig. 1.16c). This finally leads to the cold phase as the SST cools below the normal temperature. After the cold phase is fully developed, the deepening of the Z20 depth in the western Pacific brings the system to normal SST due to the recharge of warm water, reduction in the upwelling and weak trade winds over the Equatorial Pacific (Fig. 1.16d). A fully established normal phase prepares the system for the next instability, thus suggesting that the discharging and charging of the thermocline heat over the Equatorial Pacific favours transition between the ENSO phases [Ströh, 2007].

The Delay Oscillator Mechanism

The theory explains that the accumulation of ocean heat content in the western Pacific leads to an El Niño event [McPhaden, 1999] while the westward flow of the trade wind in the normal state is reversed during the El Niño event. The accompanying warming of the eastern Pacific SST during El Niño is linked to the eastward propagating Kelvin wave that brings the warm water from west to the east (Fig. 1.17, top), the Z20 depth deepens in the east and the west is affected by cold water from the westward flowing Rossby wave [Stute *et al.*, 2001; McPhaden *et al.*, 1998, McPhaden, 1999; Wyrki,

1975; McCreary, 1976; Hurlburt *et al.*, 1976]. The Kelvin wave is a type of gravity wave within the equator while the Rossby wave is produced by changes in the Coriolis force, both interacts to generate oscillation on time scale of several years [Stute *et al.*, 2001]. According to Dommenges, [2010], the magnitude of the initial SSTA in the eastern Pacific rises and propagates westward along the equator with increasing strength. The amplification of the SSTA is maintained by the air-sea interaction [Stute, 2001; Dommenges, 2010] until the easterly trade winds strengthen to normalize the situation. This tends to happen as the signal starts to decay after reflection of the Rossby wave from the west, leading to termination of the El Niño event (Fig. 1.17 bottom) [Stute *et al.*, 2001]. This leads to the cold phase on arrival of the Rossby wave in the east as a cooling Kelvin wave (after about 6 months of its initiation) (Fig. 1.17, bottom) [Stute *et al.*, 2001; Battisti and Hirst, 1989].

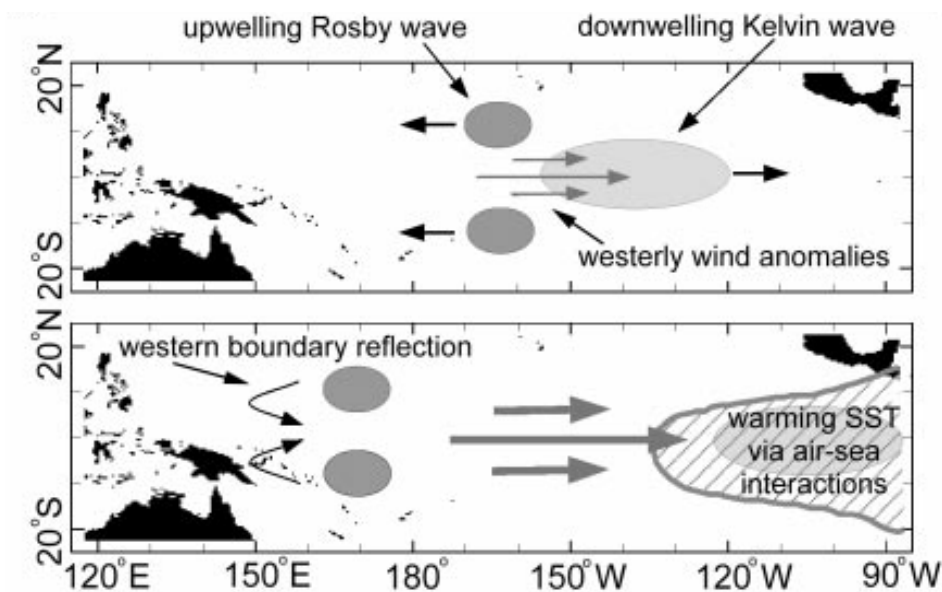


Figure 1.17: The schematic representation of the El Niño and La Niña events (Source: Stute *et al.*, 2001]. It shows eastward propagation of the Kelvin wave with warming SST signal as the trade winds weaken during an El Niño event while the Rossby wave travels in the opposite direction with cooling and weaker speed compared to the Kelvin wave (top). The warming signal is amplified by air-sea interactions on arrival of the Kelvin wave in the eastern Pacific and the reflected Rossby wave from the west helps to terminate the resulting El Niño event on reaching the east as a cooling Kelvin wave.

1.5 Research Objectives

Despite the improvements made in the understanding of ENSO mechanisms, many questions concerning the source of the variability in the ENSO development remained unanswered. Also, in spite of the confirmed influence of the Tropical Pacific on the global climate, the paleo modelling studies of the region are still insufficient [Clement *et al.*, 1999]. The assessment of the changes in the future climate requires better understanding of the natural variability in the ENSO phenomenon as it occurred in the past. Similarly, reliable projections of ENSO characteristics under different future greenhouse gas emission scenarios are highly desirable. Recently, the state-of-the-art coupled

atmosphere-ocean general circulation models (AOGCMs) are becoming better at reproducing observed patterns of interannual climate variability, including ENSO for which the driving physical mechanisms are increasingly well understood [Guilyardi *et al.*, 2009]. However, future projections of both ENSO amplitude and frequency for the 21st century are also highly uncertain [Collins *et al.*, 2010; Guilyardi, 2006]. In their report, Clement *et al.* [1999, 2000] argued that the orbital modification of the seasonal solar irradiance can change the frequency of ENSO events. Hence, part of the objectives of this study is to investigate the following:

1. How did the insolation induced annual mean SST evolve over the Eemian and Holocene towards the present day orbital conditions?
2. How did the orbitally-induced changes in the mean state of the Tropical Pacific affect the ENSO variability?

The climatic evidence from spectral analysis of SSTs derived from marine sediment ($\delta^{18}\text{O}$) within SH (in Indian Ocean) reveals major periodicities of 100,000, 43,000, 24,000 and 19,000 years which correspond closely to the Milankovitch cycles [Hays *et al.*, 1976; Imbrie and Imbrie, 1979, Buchdahl, 1999]. In view of this, the study is designed to examine the influence of orbital forcing on the Holocene and Eemian periods that have comparable orbital configurations [Braconnot *et al.*, 2008]. Thus, this investigation will also address the following questions:

3. What mechanisms come into play when using similar external forcing with varying amplitudes to induce changes in the Tropical Pacific mean state and what are the effects of the modifications on ENSO? What forcing can best explain the simulated ENSO variability?
4. Can models reproduce observed climate variations?

Answering these questions required accurate assessment of the history of ENSO event and what ENSO suggests for the future changes in the ENSO behaviour. Therefore, this study will test the sensitivity of the ENSO variability to orbitally-induced changes in the Tropical Pacific mean state as it occurred during the Holocene and the Eemian warm periods.

To investigate the relationship between ENSO and the mean climate state in the Tropical Pacific across the different warm climate intervals, the present study was carried out using a state-of-the-art AOGCM that is forced by changes in the orbital parameters (eccentricity, obliquity, precession) as occurred during the Holocene and the Eemian. **Chapter Two** of the thesis describes the model (KCM), the configuration of the simulations and comparison of the control simulation with observations so as to establish the suitability of the KCM for the present study. The model performance and sensitivity to external forcing, as well as the mechanisms that control the changes in ENSO variability are described in **Chapter Three** while the comparisons of the results with observations and other model studies are presented in **Chapter Four**. **Chapter Five** is devoted to the general discussion and major conclusions.

“You have to know the past to understand the present.”

Dr. Carl Sagan.

CHAPTER TWO

Model and Experimental Set Up

2.1 Description of the Kiel Climate Model (KCM)

The Kiel Climate Model (KCM) used in this study is described in this chapter, the description includes the control simulation and the other five experiments performed. The KCM is a sophisticated coupled atmosphere-ocean general circulation model (AOGCM) [Park and Latif, 2008; Park et al., 2009]. The atmospheric component is ECHAM5, the Hamburg (Max Planck Institute for Meteorology) atmospheric general circulation model version 5 [details in Roeckner et al., 2003], with a T31 resolution (3.75°x3.75°) horizontally and 19 vertical levels (Fig. 2.1). The ECHAM5 is coupled to the Nucleus for the European Modelling of the Ocean, NEMO [Madec et al., 1998] ocean-sea ice general circulation model through the Ocean Atmosphere Sea Ice Soil version 3, OASIS3 [Valcke, 2006] coupler as shown in Figure 2.1.

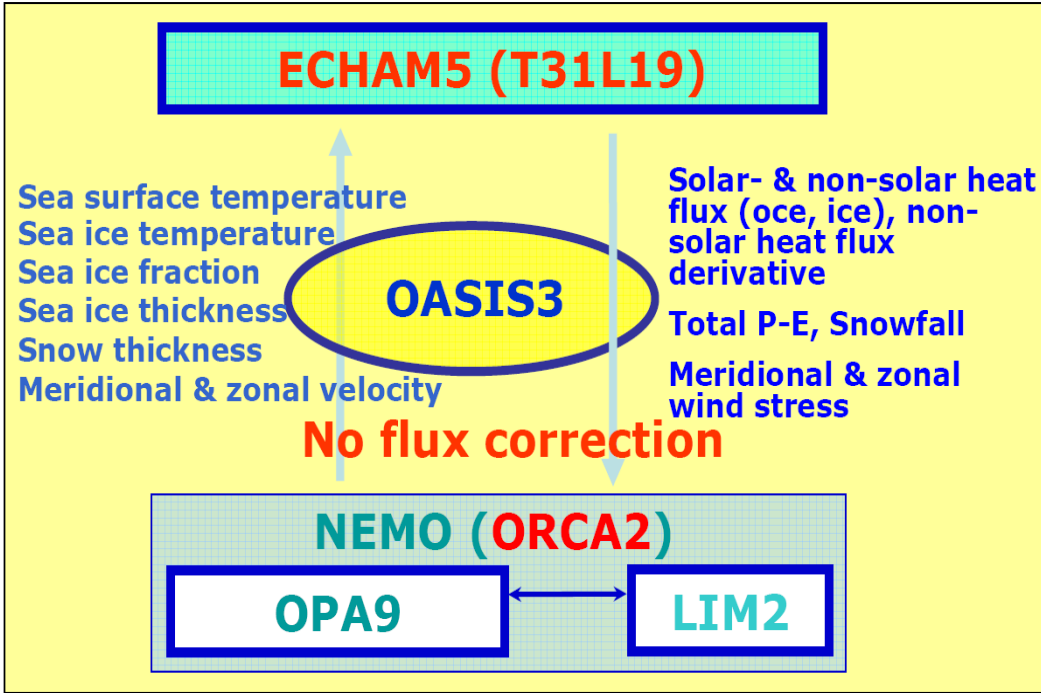


Figure 2.1: The schematic representation of the components of the KCM system [Park et al., 2009].

The ECHAM5 is a spectral model with state-of-the-art physics which was developed at the Max Planck Institute for Meteorology (MPI) as the latest version of the ECHAM models. It has been

used in the scenario simulations for the Intergovernmental Panel on Climate Change (IPCC) fourth assessment report (*IPCC AR4*, 2007), the version used in the KCM is updated with the new cloud scheme from *Tompkins* [2002]. Also, the NEMO [*Madec et al.*, 1998; *Madec*, 2008] contains the Océan Parallélisé version 9 (OPA9) ocean general circulation model (OGCM) and the Louvain-la-Neuve Ice Model version 2 (LIM2) sea ice model (Fig. 2.1). The OPA9 [*Madec*, 2008] is the current version of the OPA model from the Laboratory of Oceanography and Climatology (LOCEAN), Institut Pierre Simon Laplace (IPSL). The OPA9 is run here on a 2-degree Mercator mesh with enhanced meridional resolution of 0.5 degrees in the Equatorial region. Also included is the LIM, a 3-level dynamic-thermodynamic sea ice-snow model developed at Louvaine-la-Neuve [*Fichefet and Morales Maqueda*, 1997] which is coupled to the OPA9 and run on the ocean grid. Both the LIM and OPA models were used in the IPCC AR4 as part of the global coupled models [*Solomon et al.*, 2007].

The KCM has 182 points along the longitude, 149 points in latitude and 31 vertical levels. The 31 vertical levels are unevenly spaced with a grid distance ranging from 10 m in the upper 100 m to 500 m below. The first level represents the sea surface while the ocean floor is near the 5000 m depth. The higher resolution used at the sea surface and within the Equatorial region is necessary for capturing details of ENSO variability. The coupled model does not use flux correction, and the coupling frequency between the ocean and atmosphere is once per day [*Park et al.*, 2008]. Studies suggested that the influence of SST biases on the mean climate is minimized by using heat flux adjustment [*Turner et al.*, 2005] which removes climate drift [*Cubasch et al.*, 2006]. However, this may reduce the efficiency of the model to simulate the important atmosphere-ocean feedbacks over the Tropical Pacific [*Spencer et al.*, 2007; *Brown et al.*, 2008]. The vernal equinox date was fixed to March 21 at noon while January 1st corresponds to the initial state of the atmosphere in the simulation. The greenhouse gases were kept at pre-industrial levels (e. g. CO₂: 286 ppm; *Petit et al.*, 1999) and the effects of changes in the orbital parameters were quantified by running the model until the equilibrium forcing is reached between the surface and the middle Ocean.

2.2 The Control Experiment

The control experiment is performed with prescribed orbital configurations for eccentricity (0.0167°), obliquity (23.4°) and precession (102°) that are analogous to the preindustrial climate (or late-Holocene, 0K). The simulation follows the standard protocol of the Paleo-Modelling Intercomparison Project (PMIP) [*Joussaume and Taylor*, 1995; *Braconnot et al.*, 2008], where the orbital parameters were computed according to *Berger* [1978]. The simulation was initialized with the World Ocean Atlas (WOA) climatology [*Conkright et al.*, 2002] for temperature and salinity and integrated for 1000 years under constant preindustrial greenhouse gas concentrations (e. g., CO₂: 286 ppm; *Petit et al.*, 1999). The last 500 years of the model integration provide stable climate conditions that are used in the analyses and also eliminate the existing drifts in the initial part of the record. The climatological

mean values and the anomalies, in which the long-term monthly means are removed, are calculated for key climate variables from the control simulation.

The study is focused on the Tropical Pacific (Fig. 2.2), a region which is important for the ENSO development. The Pacific Ocean deserves a major consideration due to its areal extent, the energetic importance of the upwelling from the EEP and the strong impacts of the vast warm pool on the global climate. As a natural interannual climate fluctuation in the Tropical Pacific Ocean, the choice of the ENSO mode is associated with the strong and high spatial extent of the regional and global effects of the event through its atmospheric teleconnections. Averaged values over key regions such as those commonly called Niño3 box (150°W - 90°W , 5°S - 5°N), Niño4 box (160°E - 150°W , 5°S - 5°N) and across the Equatorial Pacific (120°E - 80°W , 5°N - 5°S) are used for characterizing the mean state and for calculating the ENSO indices. The west-east gradients of all the important variables are estimated from the difference between the Niño4 box and the Niño3 box (Niño4 minus Niño3). All the variables are linearly detrended to make sure that a potential model drift, which is very small especially in the Tropical Ocean, is largely removed. The mean climate of the control simulation is compared with data to confirm the reliability of the model outputs for studying ENSO event.

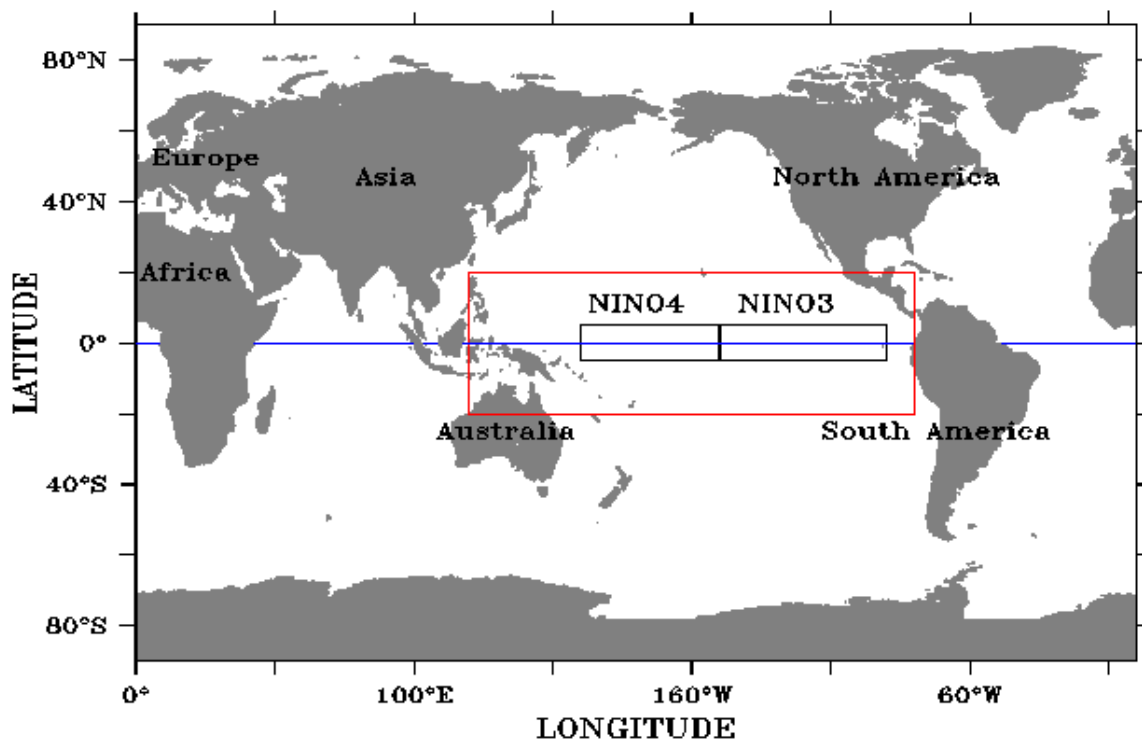


Figure 2.2: The World map showing the global oceans and the continents. The areas under the two small black boxes are commonly referred to as the Niño4 (160°E : 150°W , 5°N : 5°S) and Niño3 (150°W : 90°W , 5°N : 5°S) regions while the larger red box (120°E : 80°W , 20°N : 20°S) represents the main study area in the Tropical Pacific. The blue line stands for the Equator.

2.3 Tropical Pacific Climate in the Preindustrial Control Simulation and Observation

2.3.1 SST - The Annual Mean State

To assess the baseline model configuration for the present study, the SSTs from the preindustrial control simulation (0K) are compared with the observed SSTs from the Hadley Centre Sea Ice data, HadISST [Rayner *et al.*, 2003] over the period of 1950-1999 (Figs. 2.3a - f). The mean state shows the typical SST pattern with warm pool in the western Pacific and a colder eastern Pacific compared to the west in both 0K and the HadISST data (Figs. 2.3a, b). The simulated annual mean Equatorial Pacific SSTs (averaged over 120°E-80°W, 5°N-5°S) are about 2°C colder compared to the data (Table 2.1). This discrepancy is due to the cold-biased simulated over the Equatorial Pacific (Fig. 2.4a) and the too far westward extending cold tongue in the region (Fig. 2.3a) [see also Park *et al.*, 2009]. The transient climate response (TCR), the temperature change at the time of CO₂ doubling, is 2.9°C in the KCM, which is stronger than in other CMIP3 models (1.2°-2.6°C) [Park *et al.*, 2009].

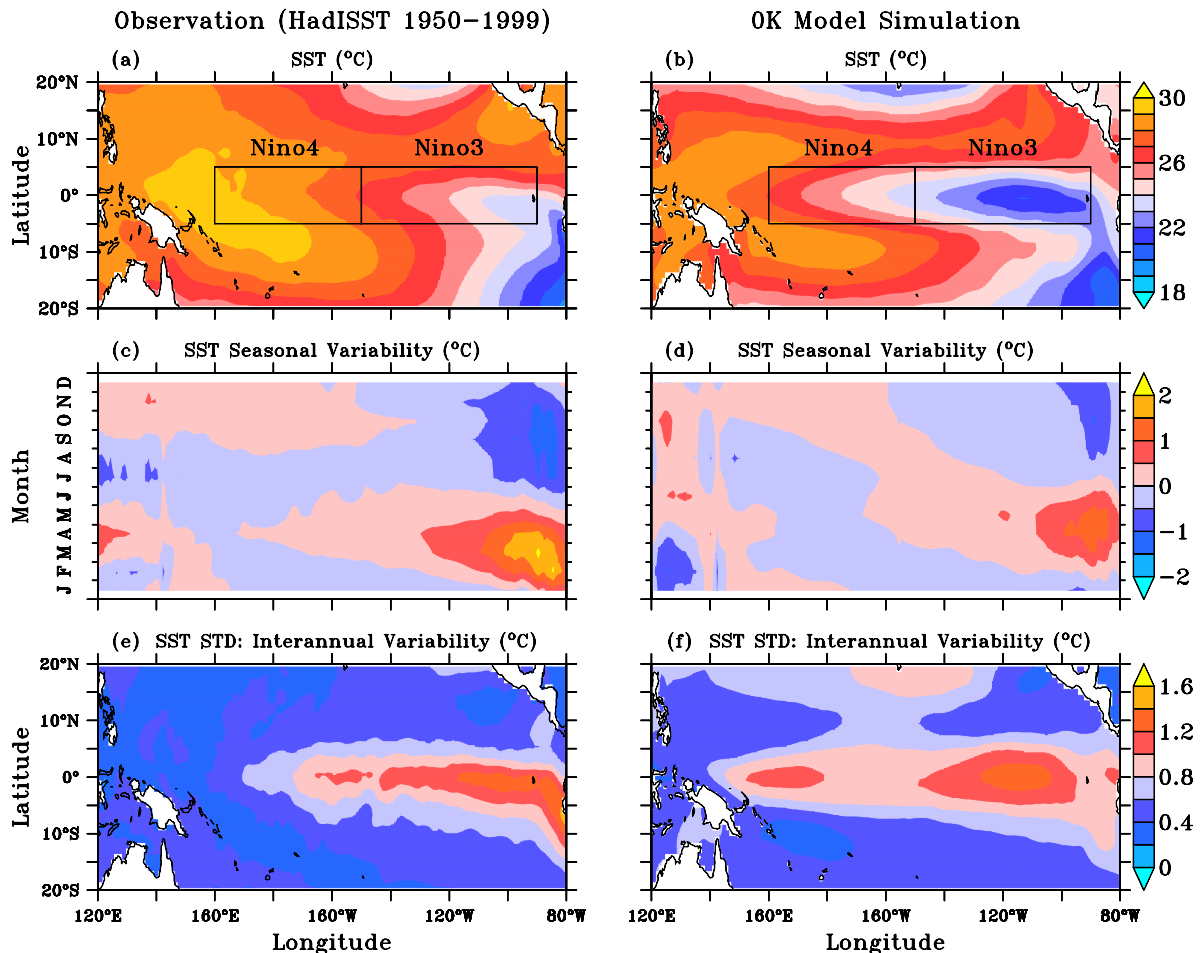


Figure 2.3: Spatio-temporal variability of SST in the Tropical Pacific (120°E-80°W, 20°N-20°S) from HadISST (1950-1999) data (left column) and the preindustrial control simulation (0K; right column): (a, b) annual mean SST; (c, d) Hovmoeller diagram of seasonal SST anomalies; (e, f) standard deviation of the de-seasonalized monthly SST anomalies.

Table 2.1: The annual mean SST over the Tropical Pacific (120°E-80°W, 5°N-5°S), Niño3 and Niño4 boxes. The SST gradient is obtained from Niño4 minus Niño3 SST, the ENSO amplitude is the standard deviation of the Niño3 SST anomaly (SSTA) while the Skewness and Kurtosis are estimated from the Niño3 SSTA.

Variables	0K Simulation	HadISST (1950-1999)
Annual Mean SST, °C	25.14	27.31
Niño4 SST, °C	25.69±0.03	28.44±0.09
Niño3 SST, °C	22.99±0.02	25.65±0.09
SST Gradient, °C	2.70±0.01	2.79±0.05
ENSO Amplitude, °C	0.91±0.03	0.89±0.08
Skewness	0.12	0.88
Excess Kurtosis#	0.10	1.31

The attached errors are one standard error for the data binned into 50 year blocks. #Excess Kurtosis= Kurtosis -3; where 3 is the kurtosis for standard normal distribution. The definition is used so that the standard normal distribution will have a kurtosis of zero.

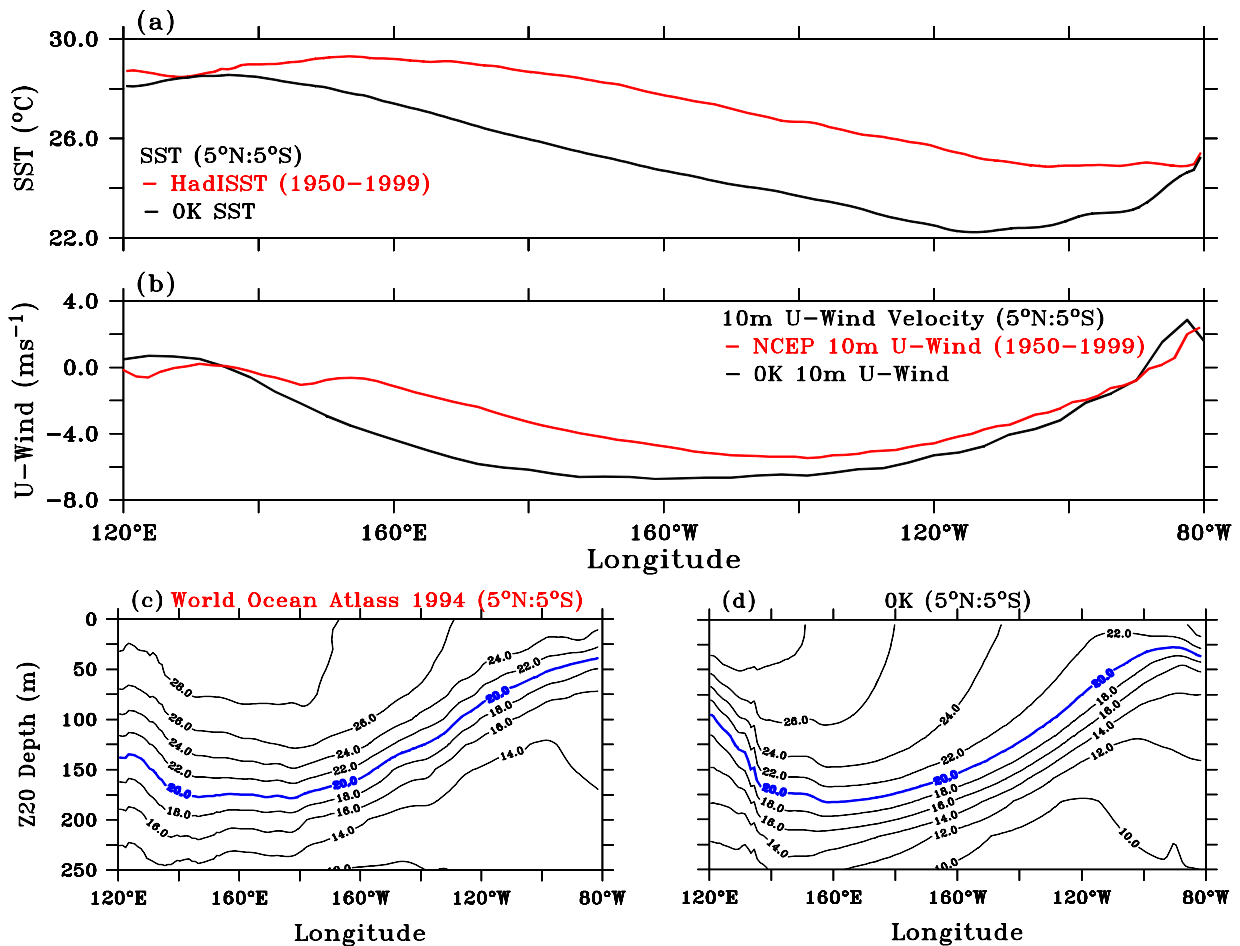


Figure 2.4: The (a) annual mean SST (°C), (b) 10m U-wind velocity (ms^{-1}), and (c, d) change in temperature with depth (m) overlay with Z20 depth (blue) within 5°N:5°S latitudes. The 10m U-Wind is estimated from the NCEP (1950-1999) data while the Z20 depth is from the World Ocean Atlas, WOA (1994) observation. (<http://www.esrl.noaa.gov/psd/data/gridded/tables/monthly.html>).

The cold bias is a common problem of non-flux corrected climate models, and possibly due to overly strong trade winds [Guilyardi, 2006; Neelin *et al.*, 1992; Latif *et al.*, 2001] and/or too strong vertical mixing in the ocean. For instance, the annual mean Niño4 zonal wind stress of -0.056Pa (Nm^{-2}) from the 0K is stronger compared with the -0.03Pa estimated from the European Centre for Medium-Range Weather Forecasts (ECWMF) Re-Analysis, ERA40 (1950-2000) data [detail in Guilyardi *et al.*, 2009]. Like in the SST (Fig. 2.4a), the magnitude of the 10m trade wind in the 0K over the Equatorial Pacific is slightly higher compared to that from the NCEP (1950-1999) observation (Fig. 2.4b) [Kalnay *et al.*, 1996]. The intensified trade wind brings the Z20 depth close to the Sea surface in the eastern Pacific in the 0K than in the WOA temperature (1994) data [Monterey and Levitus, 1997] while the observed depth deepens more in the west in response to the enhanced warming than in the 0K (Figs. 2.4c, d). Despite the Equatorial cold bias, the zonal SST gradient (Niño4 minus Niño3 SST) is comparable to the observation (Table 2.1) [see also Liu 1998]. This is mainly explained by the influence of the cold bias over the Tropical Pacific which tends to cancel out in the estimation of the annual mean west-east SST gradient (Fig. 2.4a).

2.3.2 SST - The Seasonal Cycle and the Interannual Variability

As shown in Figures 2.3(c, d), the seasonal cycle of the SST (averaged over 20°N - 20°S) is plotted as deviations from the annual mean SST over the Tropical Pacific. The annual SST cycle in the eastern Tropical Pacific, the westward propagation of the SST signal, and the semi-annual cycle of the SST in the western Tropical Pacific are clearly reproduced by the model. The existence of an annual cycle of the SST in the east is associated with the upwelling-induced dampening of the mean SST in the region, the annual cycle in the eastern Pacific is strongest in March while the strength is least in September (Figs. 2.3c, d) [see also Xie *et al.*, 2007]. However, the amplitude of the simulated annual cycle of the SST is underestimated in the eastern Tropical Pacific and it has its peak delayed by about 1-2 months due to phase lag in the ocean's response. Similarly, the underestimated SST signal in the far west occurred within the first six months while an overestimation happened between July-October in the west and part of the Central Pacific. Model studies showed that a high meridional resolution in the ocean components with a properly resolved coastal and Equatorial upwelling is a necessary condition for simulating the realistic annual SST cycle in the eastern Pacific [Latif *et al.*, 2001]. In addition, an improvement in the simulation of the low-level stratus cloud has also been suggested by Mechoso *et al.* [1995] as needed for producing better annual SST cycle in the east.

The simulated interannual variability in the SST derived from the standard deviation of the long-term SST anomaly is in good agreement with the observation in the eastern Pacific in terms of both the strength and location of maximum variability (Figs. 2.3e, f). In both cases, the variability is generally higher in the eastern Pacific compared to the west where the variation in the year long SST

warming is generally low than in the east. However, the model overestimates the interannual SST variability in the WPWP as indicated by the spatial pattern of the long-term standard deviation of the SST. These disagreements with observation could be expected given the Equatorial cold tongue extends too far to the west.

2.3.3 Precipitation - The Annual Mean State

The assessment of the changes in the annual mean state, seasonal variability and interannual variability is further extended to the simulated and observed precipitation (Figs. 2.5a - f). The annual mean changes in the precipitation pattern show good agreement with the observation (Figs. 2.5a, b). The regions of higher downpour are found along the ITCZ position (in the NH) and also restricted to the WPWP compared to the east in the OK and in NOAA GPCP precipitation (1980-2009) data [Adler *et al.*, 2003] (Figs. 2.5a, b). In accordance with the simulated SST, the annual mean precipitation in the Niño3 box, Niño4 box and over the entire Equatorial Pacific (120°E:80°W, 5°N-5°S) are generally lower in the OK compared to the observation (Table 2.2). In addition, the magnitude of the west-east precipitation gradient is higher in the observation compared to the OK while there is overestimation of the spatial coverage within the ITCZ position and over the Indo-Pacific region. This disagreement might be linked to the comparison of modern observation with a preindustrial simulation.

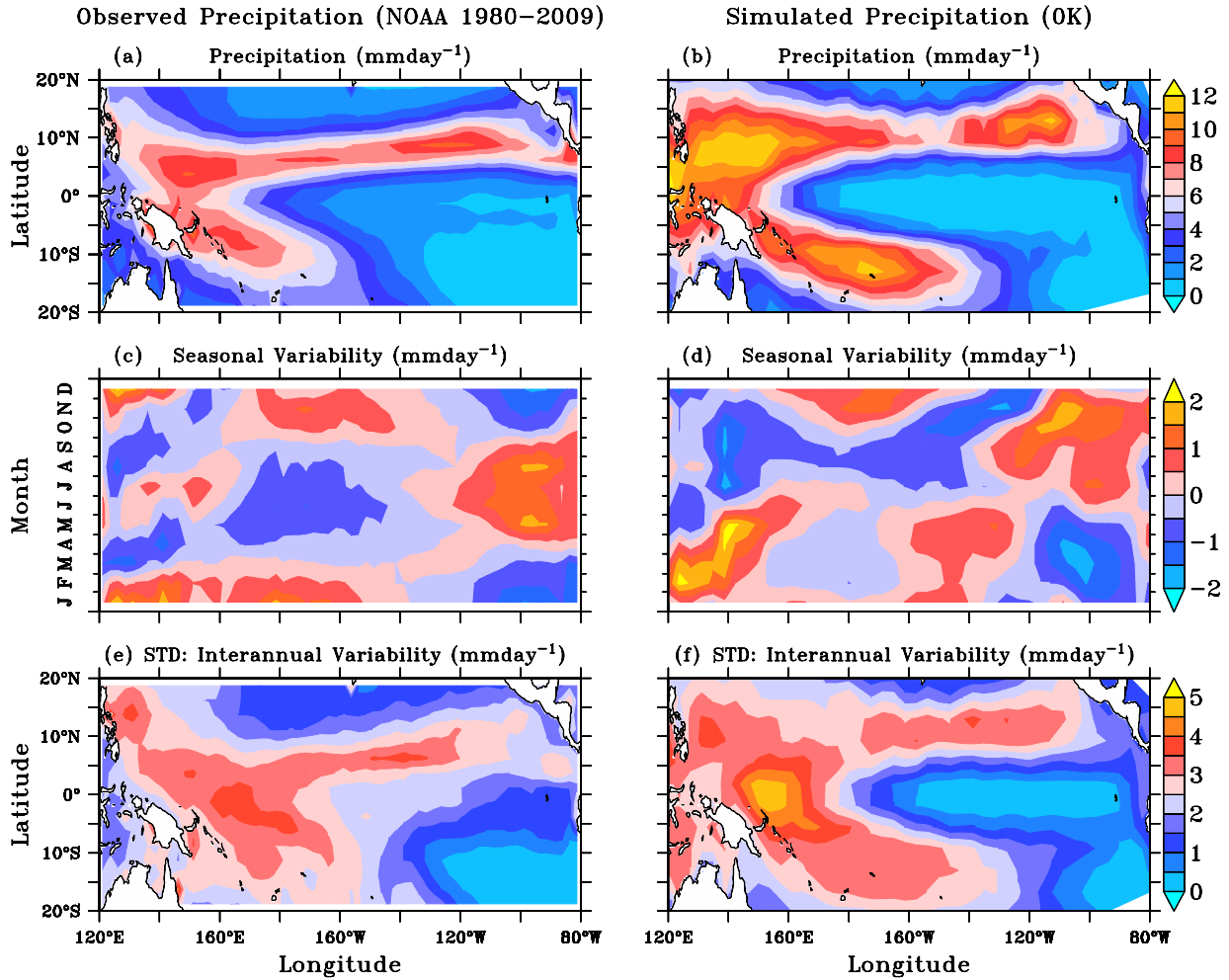


Figure 2.5: Spatio-temporal variability of precipitation in the Tropical Pacific (120°E-80°W, 20°N-20°S) from NOAA GPCP monthly precipitation (1980-2009) data (left column) and the preindustrial control simulation (0K; right column). The figure shows the (a, b) annual mean precipitation, (c, d) Hovmoeller diagram of seasonal precipitation anomalies, (e, f) standard deviation of the deseasonalized monthly precipitation anomalies. The precipitation is the combine monthly mean observations and satellite data from the GPCP version 2.2 (Data source: <http://www.esrl.noaa.gov/psd/data/gridded/tables/monthly.html>).

Table 2.2: The annual mean values of precipitation over the Equatorial Pacific (120°E-80°W, 5°N-5°S), Niño3 and Niño4 boxes. The precipitation gradient is obtained from Niño4 minus Niño3 values.

Precipitation (mmday ⁻¹)	0K Simulation	NOAA (1980-2009) Data
Annual Mean	3.11	3.69
Niño4 Box	1.80	4.20
Niño3 Box	0.59	1.57
West-East Gradient	1.21	2.63

2.3.4 Precipitation - The Seasonal Cycle and the Interannual Variability

The annual cycle of the precipitation (averaged over 20°N-20°S) is reproduced in the eastern Tropical Pacific while the semi-annual cycle in the western Pacific is in agreement with the observation (Figs. 2.5c, d). However, the strong signal centered in boreal summer over the eastern Pacific in the observation is shifted to late boreal summer-fall in the OK. In addition, the magnitude of the annual cycle is underestimated in the eastern Pacific in February-June. The overestimations in boreal spring and late boreal summer-fall over the western Pacific are alternated by underestimated signal of the seasonal cycle. Also, the intensity of the seasonal cycle of the precipitation in the Central Pacific is weaker in the OK compared to the observation within September-October and during late boreal winter while the model overestimates the seasonal signal between May-August. The interannual variability of the precipitation is in better agreement with the observation in the western Tropical Pacific in terms of the locations of maximum changes as shown by the long-term standard deviation of the precipitation anomaly (Figs. 2.5e, f). The model overestimates the interannual variability in the precipitation over the WPWP and within the ITCZ position in the NH while the variability is underestimated in most parts of the eastern Pacific.

2.4 Changes in the Simple Indices

The ENSO amplitude in the OK, defined as the standard deviation of the de-seasonalized monthly SST anomalies (SSTA), is 0.91°C. This is in good agreement with the 0.89°C from the HadISST data (Table 2.1) which corresponds to about 2.2% increase in the simulated value when compared to the observation. However, the low skewness and kurtosis indicate that the Niño3 SSTA distribution is too broad and too symmetric. In particular, the model underestimates the observed tendency towards warm SST anomalies, which is shown by the higher positive skewness in the HadISST data compared to the OK (Table 2.1). The spectra of the Niño3 SST anomalies peak between 3-4 years, which is at slightly shorter period compared to the observation (Fig. 2.6).

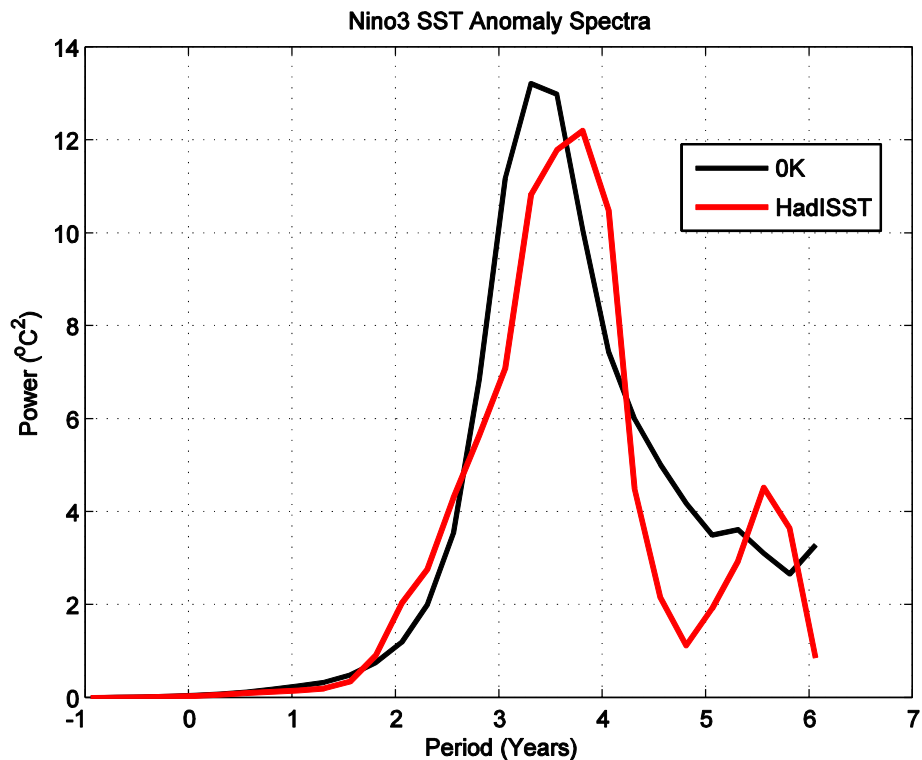


Figure 2.6: The spectra ($^{\circ}\text{C}^2$) of the de-seasonalized monthly Niño3 SST anomalies for the late-Holocene (OK, black line) and the HadISST 1950-1999 data (red line).

In spite of the differences, which in part may result from the use of 500 years of model outputs in contrast to 50 years of HadISST (1950-1999) data, the preindustrial control simulation (OK) represents the important aspects of the mean Tropical Pacific climate and ENSO reasonably well. The KCM has previously been shown to realistically reproduce the present day climate and global ocean circulation [Park *et al.*, 2009; Park and Latif, 2008]. In particular, the annual mean state, semi-annual and annual cycle, and the interannual variability are well simulated in the Tropical Pacific [Park *et al.*, 2009]. The KCM also simulates the characteristics of the internal climate variability such as the Pacific Decadal Variability and the Atlantic Multidecadal Variability comparable to the observation in terms of spatial and temporal structures [Park and Latif, 2010]. The response of the KCM to periodic multi-decadal and centennial solar forcing is examined by Park and Latif [2011]. More details including the KCM's performance of the modern mean state and variability, and the model's response to enhanced CO_2 can be found in Park *et al.* [2009].

2.5 The Experiments

In the present study, six quasi-steady state (time-slice) experiments are performed with prescribed orbital configurations for the parameters eccentricity, obliquity and precession, representing distinct time periods during two warm climates (Holocene and Eemian). For the Holocene, these include the

early Holocene (9.5 kyr BP), mid Holocene (6 kyr BP) and the preindustrial (0 kyr BP) simulations while the Eemian consists of the early Eemian (126 kyr BP), mid Eemian (122 kyr BP) and the late Eemian (115 kyr BP) (Table 2.3; Fig. 2.7) [see also *Braconnot et al.*, 2008; *Schneider et al.*, 2010; *Khon et al.*, 2010]. Both warm periods underwent similar transient changes of the orbital parameters. For example, obliquity decreased over time while the precessional index increased during both epochs. Overall, eccentricity was about two times higher during the Eemian compared to the Holocene, the eccentricity slightly increased during the Eemian, whereas it decreased in the Holocene (Table 2.3).

Table 2.3: Characteristics of the Kiel Climate Model (KCM) used in this study.

Time Period	0 K	6 K	9.5 K	115 K	122 K	126 K
Experiment Name	H0K	H6K	H9K	E15	E22	E26
Eccentricity (°)	0.0167	0.0187	0.0194	0.0414	0.0407	0.0397
Obliquity (°)	23.4	24.1	24.2	22.4	23.2	23.9
Precession ($\omega-180$)°	102	1	303	111	356	291
CO ₂ Concentration (ppm)*	286.2	286.2	286.2	286.2	286.2	286.2

*ppm = part per million (volume).

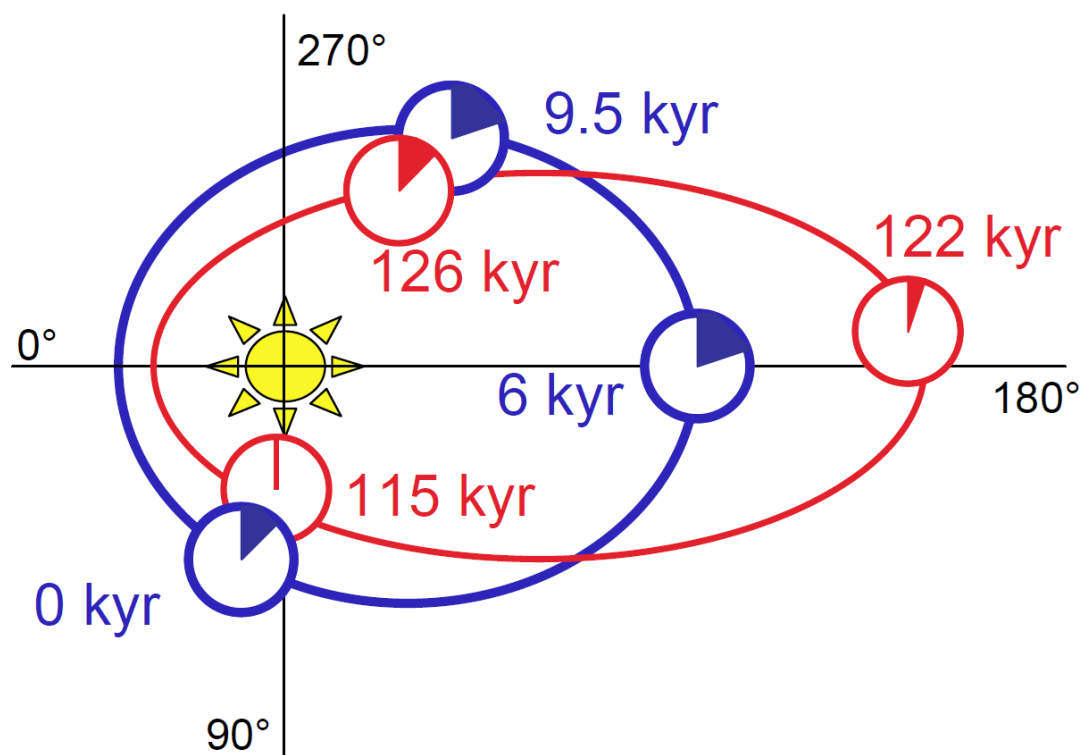


Figure 2.7: Sketch illustrating the solar constellations of the different time periods used in the present study [adapted from *Braconnot et al.*, 2008]. Shown is the location of the vernal equinox on the Earth's orbit around the Sun (first day of the Spring; March 20 in the NH). Blue and red orbits are the Holocene and Eemian epochs, respectively. The wedges roughly sketch relative changes in obliquity.

Since the time of maximum insolation in a year and length of seasons depends on the precession, the time slices were therefore chosen so as to allow similar changes in the precession and the resulting seasonality across the Holocene and the Eemian [Braconnot *et al.*, 2008, Berger, 1988]. Precessionally pair-wise similar experiments are performed for the respective early, middle and late phases of both periods (Fig. 2.7). Although the global annual mean insolation remained virtually constant for all time periods, the resulting seasonal and latitudinal insolation changes during the Eemian were about twice as large as during the Holocene (Table 2.3). This is in accordance with the observed temperature anomaly from Vostok (78.24°S, 106.54°E) ice core (Figs. 2.8a, b) where the temperature patterns are similar across both periods but with higher amplitude in the Eemian when compared to the Holocene climate [Lorius *et al.*, 1995].

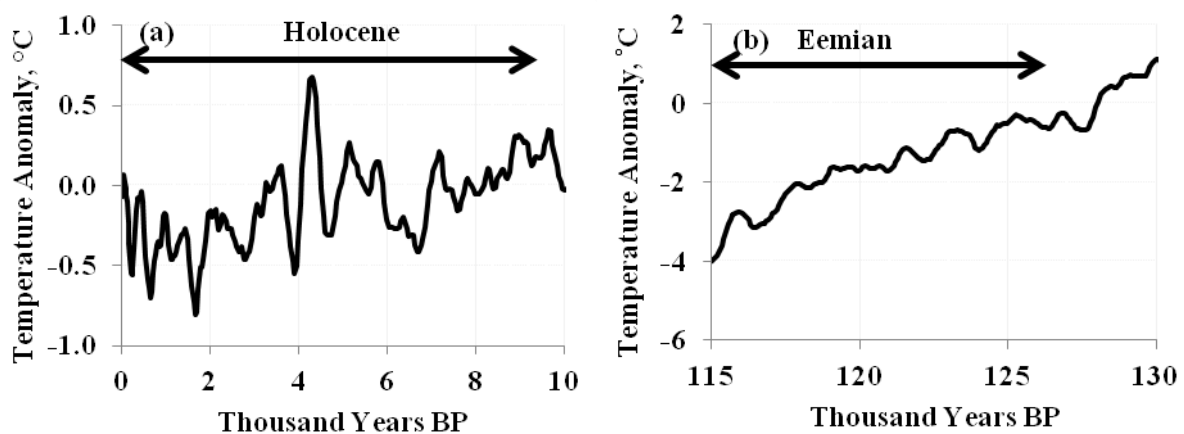


Figure 2.8: Same as in figure 1.6 except for showing the temperature anomaly relative to present over the (a) Holocene and (b) Eemian as estimated from the Vostok (78.24°S, 106.54°E) ice core data [Lorius *et al.*, 1995]. The arrows show the periods covered in this study. Note the differences in the scales.

The simulation follows the standard protocol of the PMIP [Joussaume and Taylor, 1995; Braconnot *et al.*, 2008], where the orbital parameters were computed according to Berger [1978]. During the Holocene, factors other than orbital forcing are assumed to be of minor importance. The orbital forcing is probably the major climate driver enabling us to directly compare our model results with proxy data. However, for the Eemian, the neglect of changes in the sea level and ice sheet extent is probably oversimplifying [Otto-Bliesner *et al.*, 2006], while the role of dynamic vegetation during the mid-Holocene is still under debate [Ganopolski *et al.*, 1998; Zeng and Neelin, 2000; Cuffey *et al.*, 2000; IPCC, 2007]. Consequently, the investigation is rather a sensitivity study, testing the response of a climate model to changes in the orbital configurations including sea-ice feedbacks. Our focus is on the mechanisms that come into play when using similar external forcing with varying amplitudes to induce changes in the Tropical Pacific mean state that may influence ENSO.

All simulations were initialized with the WOA climatology [Conkright *et al.*, 2002] of temperature and salinity and integrated for 1000 years under constant preindustrial greenhouse gas concentrations (e.g. CO₂: 286 ppm) [Petit *et al.*, 1999] (Table 2.3). As in the control simulation, only the last 500 years of each experiment provide stable climate conditions in the upper ocean and were used for all the analyses. All variables were linearly de-trended to remove the remaining small model drift. Monthly climatologies and monthly deseasonalized anomalies were then calculated for selected variables. Finally, the variables were averaged over key regions such as the Niño3 (150°-90°W, 5°S-5°N) and Niño4 (160°E-150°W, 5°S-5°N) boxes to obtain the mean state and the ENSO indices.

"The farther backward you can look, the farther forward you are likely to see."

-Winston Churchill

CHAPTER THREE

The Impacts of Orbital Forcing

The simulated mean climates of the Holocene and the Eemian generated by changing the orbital forcing are reported in this chapter. The aim of the study is to investigate the influence of the orbitally-induced changes on the annual mean state, on the seasonal variability and on the interannual variability over the Tropical Pacific while the changes in the heat budget are also analysed. In addition, the impacts of the simulated mean state changes of the Tropical Pacific on ENSO variability and the relationship with the variations in the atmospheric circulation are reported.

3.1 Changes in the Tropical Pacific Mean Climate

3.1.1 SST - The Annual Mean State

The changing orbital configurations during both the Holocene and the Eemian result in an annual mean increase in the top of the atmosphere (TOA) insolation and the corresponding rise in the annual mean SST in the Tropical Pacific over time due to the decreasing obliquity (Table 3.1). The warm pool-cold tongue structure of the SST along the Equatorial Pacific is well simulated by the KCM in all the time slices (Figs. 3.1a-f) and clearly revealed by the longitudinal variations of the SSTs (averaged over 5°N-5°S latitudes) (Figs. 3.2a-b). Based on the 28°C definition [Zhang and Chen, 2008; Ho et al., 1995], the spatial coverage of the WPWP increases over time with the least coverage in the 9.5K and 126K while the magnitude is higher in the Eemian compared to the Holocene where the applied forcing is lower. The westward extension of the cold tongue is strongest in the 9.5K (126K) and slightly decreases thereafter in both epochs (Figs. 3.1a-f). In clear agreement with the intensified SST in the Niño4 region with respect to the Niño3 box, the annual mean west-east SST gradient increases over time during the Holocene and the Eemian climates (Table 3.1). However, the rising trend of the annual mean SST in the Niño3 box is interrupted by the strong cooling in both 6K and 122K (Table 3.1) due to the enhanced upwelling of cold water (see 120°W-100°W, Figs. 3.1c, d, Figs. 3.2a, b) caused by the stronger easterlies in both cases when compared to the other time slices (Table 3.1).

Table 3.1: The annual mean values of the TOA insolation, surface insolation, SST and trade winds for all the time slices (including 0K for comparison). The SST gradients are obtained from Niño4 minus Niño3 SST while the ENSO amplitude is the standard deviation of the SST anomaly. The errors are one standard error obtained using data binned into 50 years blocks.

Time Period	0 K	6 K	9.5 K	115 K	122 K	126 K
*TOA Insolation, Wm^{-2}	416.8	415.9	415.7	418.6	417.5	416.4
*Surf. Insolation, Wm^{-2}	235.0	235.7	236.2	234.3	237.2	237.4
*Mean SST, $^{\circ}\text{C}$	25.14	24.62	24.57	25.55	24.91	24.76
Niño4 SST, $^{\circ}\text{C}$	25.69 \pm 0.03	25.07 \pm 0.03	24.91 \pm 0.02	26.15 \pm 0.02	25.34 \pm 0.03	25.02 \pm 0.02
Niño3 SST, $^{\circ}\text{C}$	22.99 \pm 0.02	22.49 \pm 0.02	22.54 \pm 0.02	23.40 \pm 0.02	22.78 \pm 0.02	22.81 \pm 0.02
SST Gradient, $^{\circ}\text{C}$	2.70 \pm 0.01	2.58 \pm 0.01	2.37 \pm 0.01	2.75 \pm 0.01	2.56 \pm 0.01	2.21 \pm 0.01
*Trade Winds, Nm^{-2}	-0.0359	-0.0382	-0.0382	-0.0352	-0.0391	-0.0386
ENSO Amplitude, $^{\circ}\text{C}$	0.91 \pm 0.03	0.86 \pm 0.02	0.81 \pm 0.03	0.94 \pm 0.03	0.84 \pm 0.02	0.77 \pm 0.03

The asterisked (*) variables are averaged over 120°E - 80°W , 5°N - 5°S of the Equatorial Pacific. The strength of the trade wind increases as it becomes more negative.

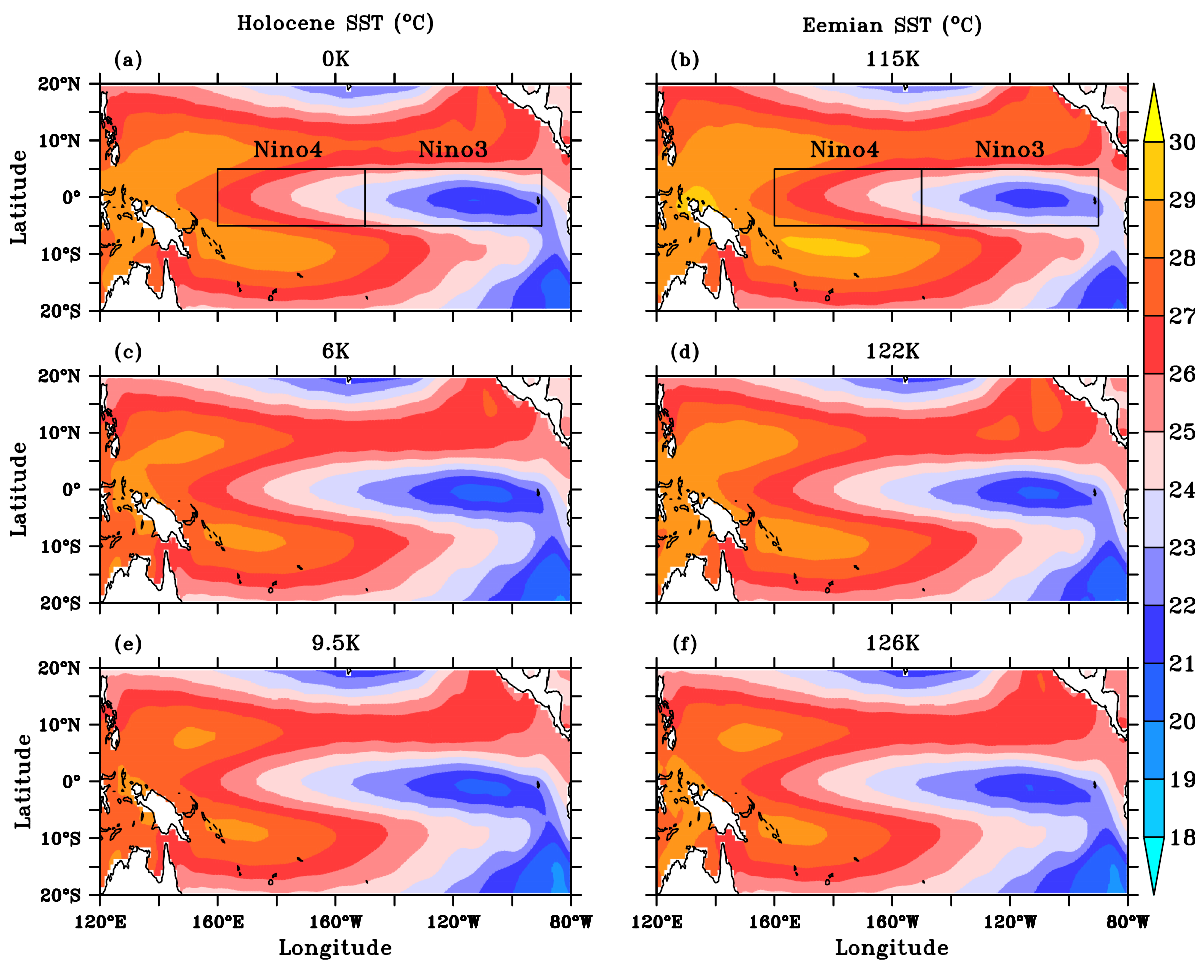


Figure 3.1: The spatial distribution of the simulated SST ($^{\circ}\text{C}$) over the Tropical Pacific from the Holocene and Eemian climates.

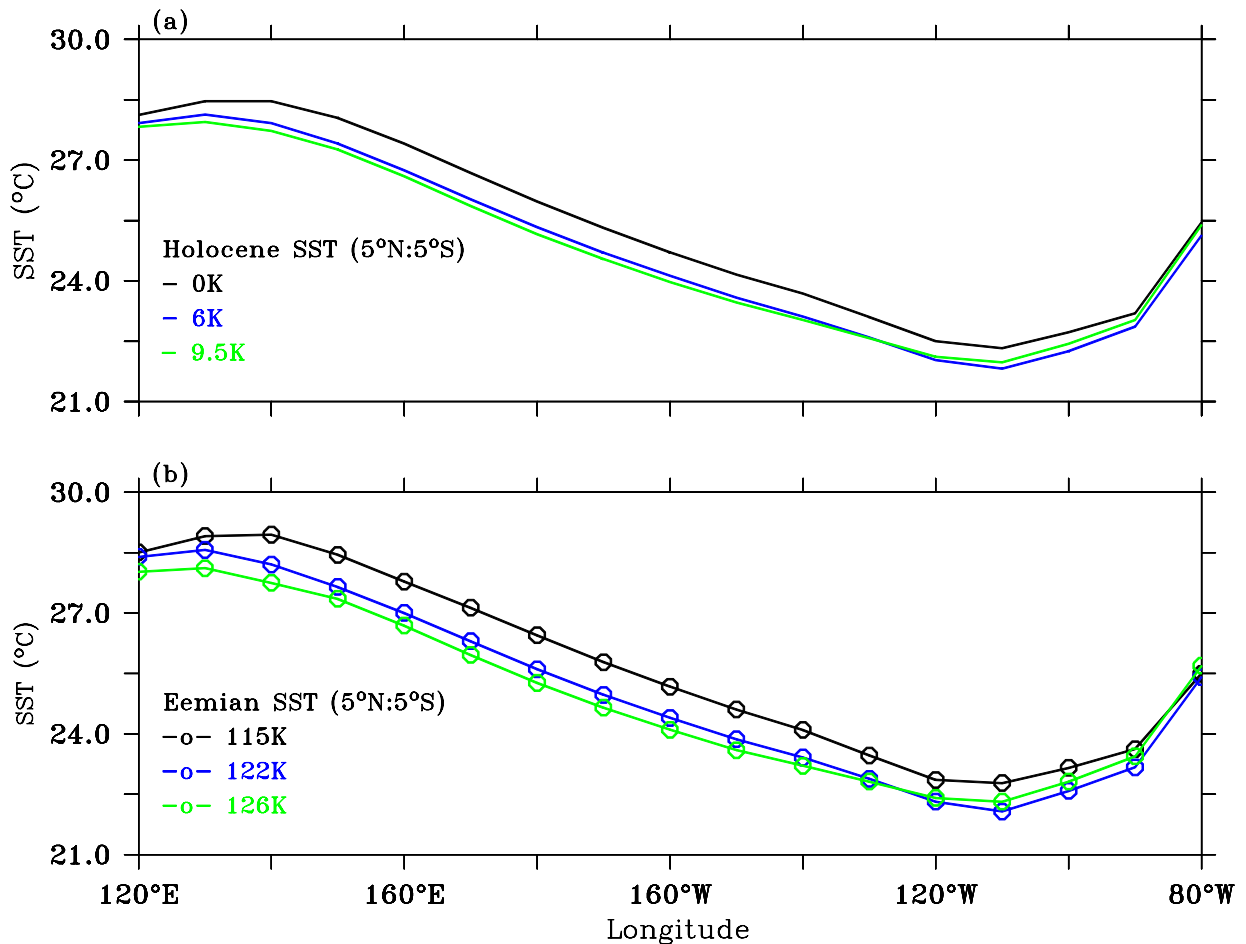


Figure 3.2: The annual mean SST (°C) along the Equator, averaged over 5°N-5°S latitudes.

3.1.2 SST - The Seasonal Cycle

The seasonal cycle of the simulated SST (estimated over 20°N-20°S) displayed a semi-annual cycle of the SST in the western Pacific with a weaker magnitude in the 0K compared to the 115K (Figs. 3.3a, d). An annual cycle of the SST is seen in the other time slices with stronger magnitude in the 9.5K (126K) compared to the 6K (122K) (Figs. 3.3b, c, e, f). The magnitudes and the spatial extents of the seasonal cycles are higher in the Eemian compared to the Holocene which has reduced forcing. The result further shows the predominance of annual cycle in the cold tongue in the 115K (as also seen in the 0K) and a more semi-annual cycle pattern is simulated in the other time slices. There is westward extension of the warm SST signal within the first 5 to 6 months in the 0K and 115K, and in the boreal summer-autumn in the other simulations (Fig. 3.3). The exception to the above pattern is seen in the 122K where the westward SST warming is delayed till boreal autumn-winter (Fig. 3.3) probably due to prolonged periods of westward flow of cold SST caused by the strong trade wind in the 122K (Table 3.1). The cold signal spreads westward in the second half of the year in the 115K while this occurred within January-April in the middle and late periods of both Holocene and Eemian.

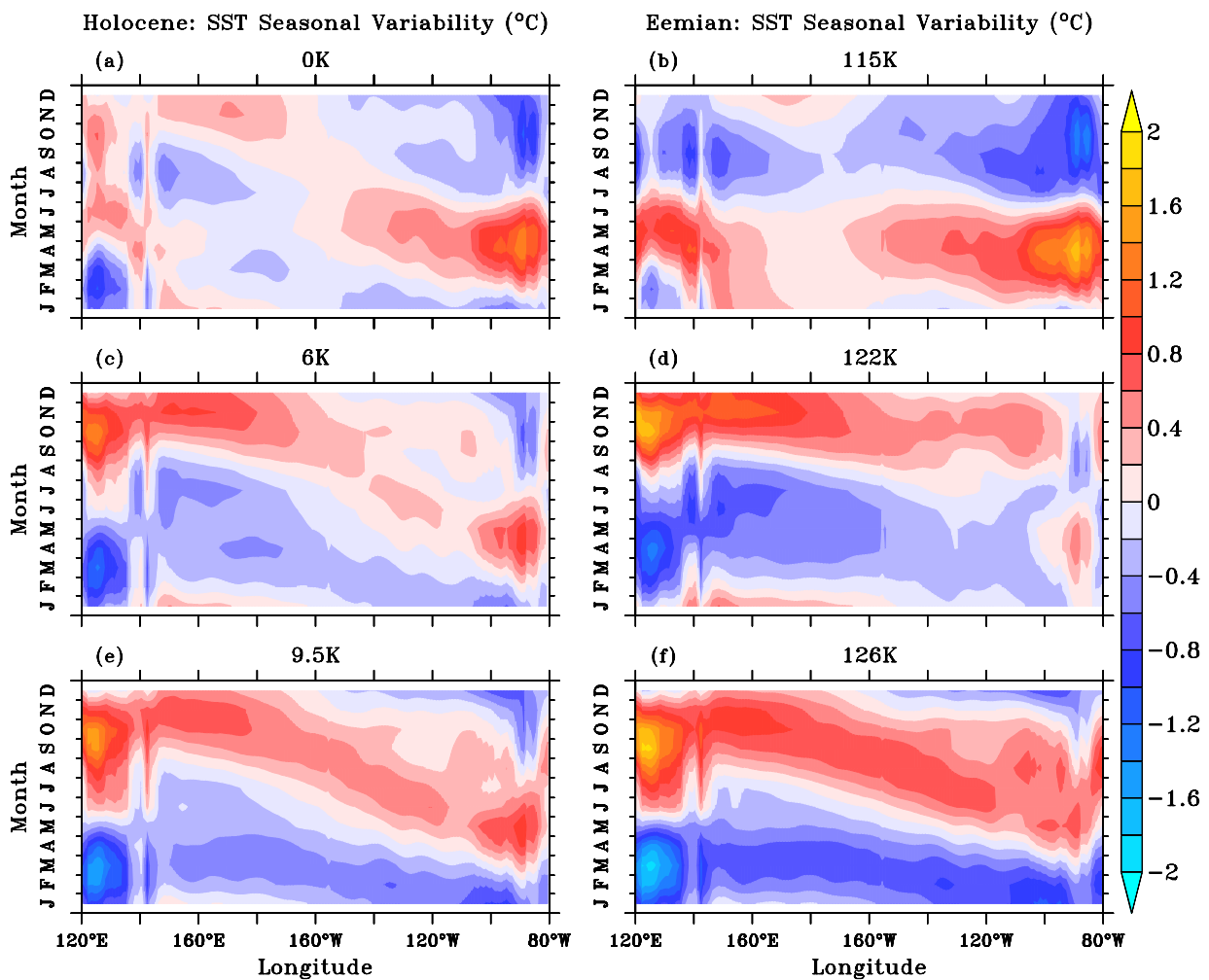


Figure 3.3: The seasonal cycle (minus the annual mean) of the simulated SST ($^{\circ}\text{C}$) averaged over the $20^{\circ}\text{N}:20^{\circ}\text{S}$ latitudes.

3.1.3 SST - The Interannual Variability

According to Figures 3.4 (a-f), the spatial pattern of the estimated interannual variability from the long-term standard deviation of the SSTA reveals high variability in the eastern Pacific which increases over time reaching the maximum in the warmer climates, 0K and 115K. Similarly, the westward extension of the variability is weak in the 9.5K and 126K simulations while it increases thereafter in both epochs. The strongest westward extension of the variability is seen in the 115K which is consistent with the higher forcing in the Eemian compared to the Holocene. However, the magnitude of the westward extending signal is slightly reduced in the other Eemian periods compared with the corresponding Holocene climates. The westward shift in the SST variability is expected given the Equatorial cold tongue extends too far to the west in both epochs (see Fig. 3.1).

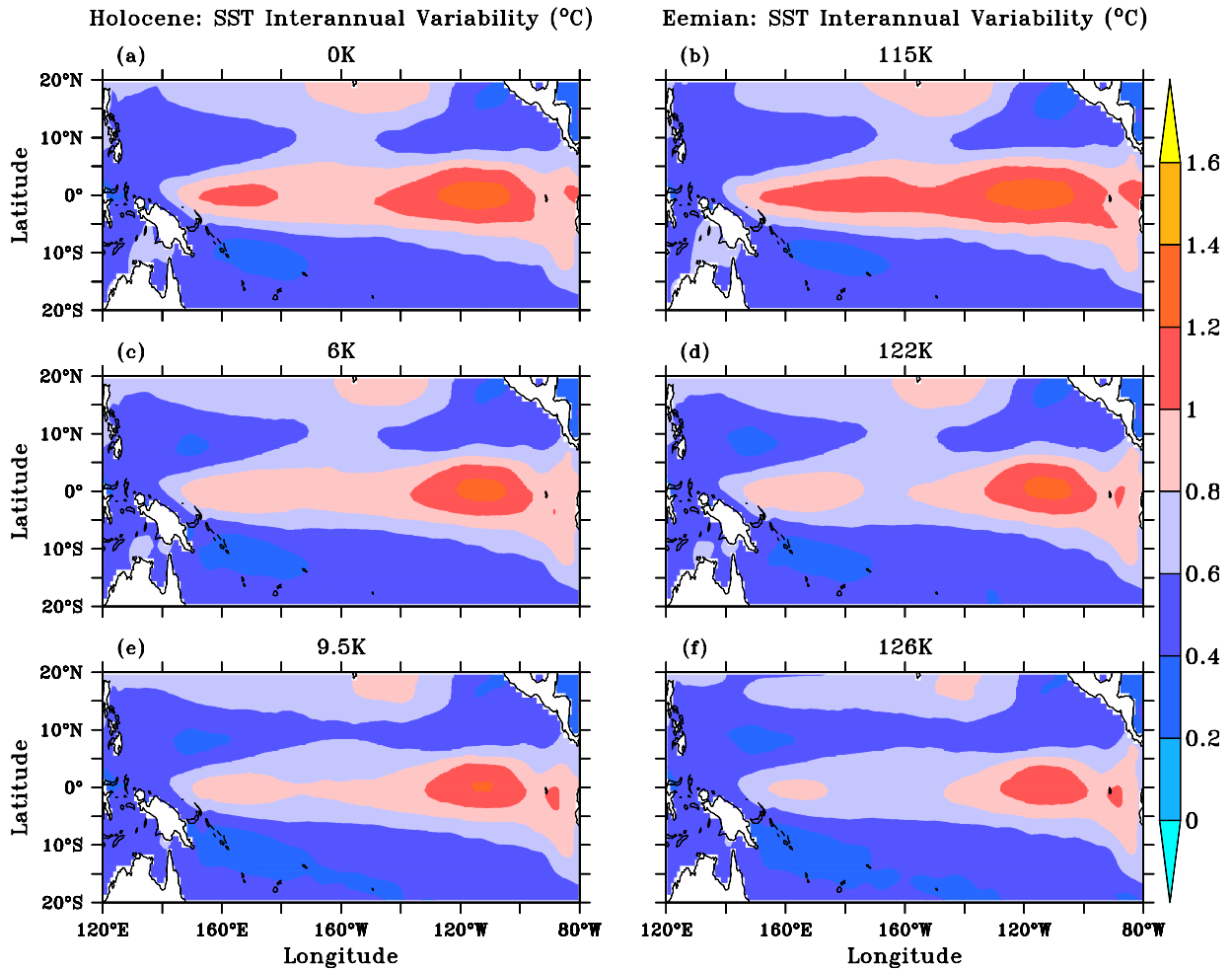


Figure 3.4: The interannual Variability estimated from the standard deviation of the SST anomaly ($^{\circ}\text{C}$) averaged over $20^{\circ}\text{N}:20^{\circ}\text{S}$ of the Tropical Pacific.

3.1.4 The Semi-annual and Annual cycles

The annual mean SSTs averaged over the Equatorial Pacific ($120^{\circ}\text{E}-80^{\circ}\text{W}$, $5^{\circ}\text{N}-5^{\circ}\text{S}$) largely follow the obliquity forcing [Liu *et al.*, 2003; Timmermann *et al.*, 2007] with a minor warming trend ($\sim 0.1^{\circ}\text{C}$) during the early and a considerably stronger warming trend ($\sim 0.5-0.7^{\circ}\text{C}$) during the late phases of both epochs, respectively. Furthermore, there is a precession-induced shift in the semi-annual insolation cycle, which has its insolation maximum in boreal fall (September-October) from the beginning to the middle of both periods, shifting towards boreal spring (March-April) in the late Holocene and Eemian, respectively (Fig. 3.5a).

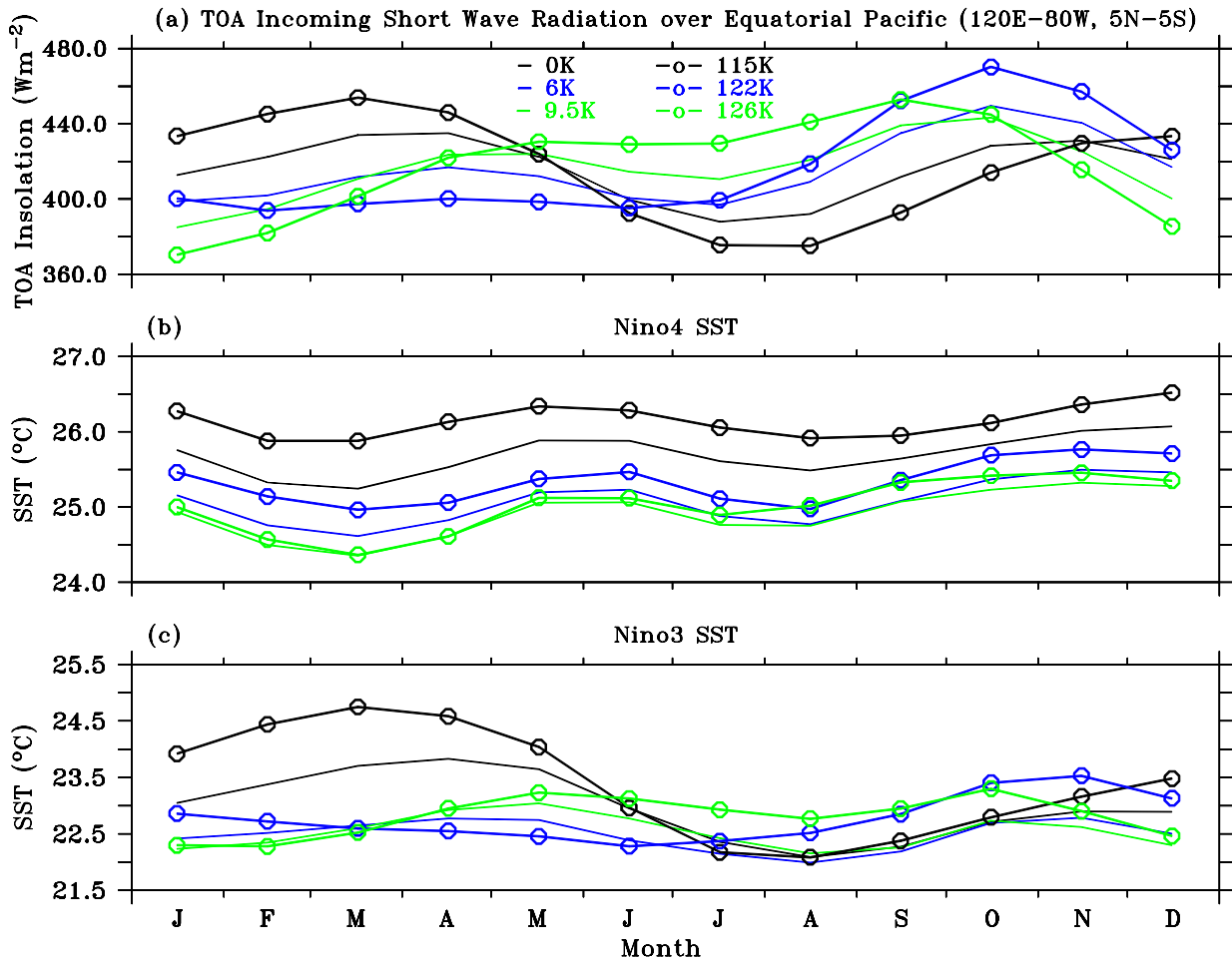


Figure 3.5: Monthly averages over the Equatorial Pacific (120°E-80°W, 5°N-5°S) of (a) top of atmosphere (TOA) incoming short wave radiation (Wm^{-2}), (b) Niño4 SST ($^{\circ}C$) and (c) Niño3 SST ($^{\circ}C$). Note the difference in the scales for the SST in (b) and (c). Line and colour code as in Figure 3.

The semi-annual cycle of the Tropical insolation forcing translates into a semi-annual cycle of the SST in the Niño4 region (Fig. 3.5b) with a phase-lag of about 1-2 months in all the simulations [see also *Timmermann et al., 2007; Braconnot et al., 2008*]. In the EEP (Niño3 region), the same forcing results in an annual SST cycle in the late Holocene and late Eemian runs (Fig. 3.5c), presumably due to strong coupling in ocean-atmosphere interactions [see e. g., *Neelin et al., 1994; Philander, 1999*]. An indicator for increasing coupling strength over time is given by the linear fit of Niño4 zonal wind stress anomalies against the Niño3 SST anomalies [see also *Guilyardi, 2006*] where a slight increase of the regression slope over the Holocene and Eemian suggests an intensification of the air-sea coupling (Fig. 3.6). For instance, the percentage increase in the coupling strength between the extreme climates (0K vs 9.5K; 115K vs 126K) is 1.2% in the Holocene (Figs. 3.6a, c) and 12.3% in the Eemian (Figs. 3.6b, d) where more forcing is applied. However, it is not obvious whether the lack of a clear seasonal cycle in the Niño3 region over both epochs is a model artifact due to too weak air-sea coupling or constitutes a real signal, since paleo data resolving the seasonal cycle are missing.

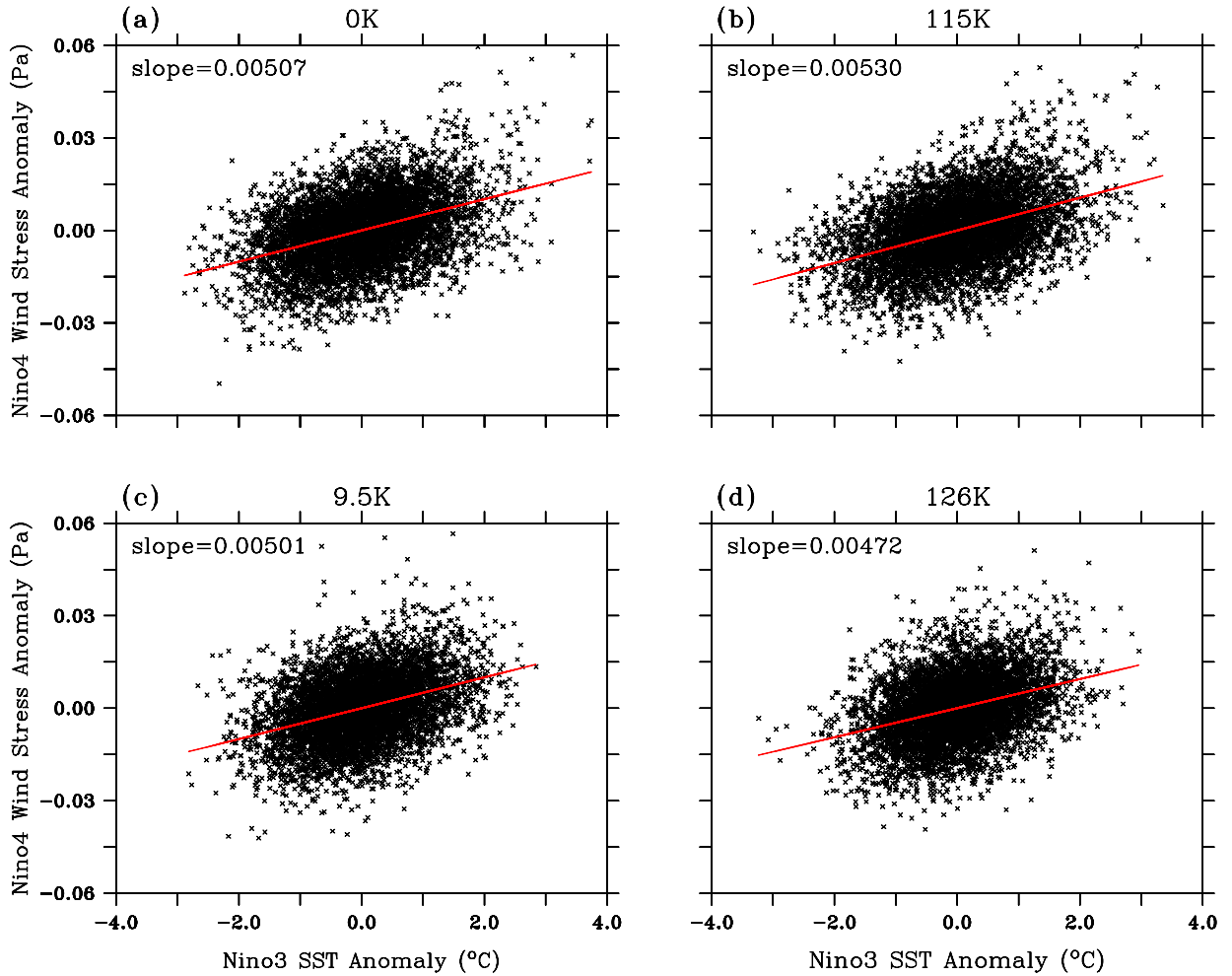


Figure 3.6: Scatter plots and linear regressions of Niño4 wind stress anomaly (Pa) against Niño3 SSTA (°C) for the investigation of air-sea coupling between the extreme climates.

3.1.5 Changes in the Surface Heat Flux and the Ocean Heat Transport

Differences in the net surface heat flux (Q_{net}) between the respective early and late stages of both warm periods (Holocene, Eemian) reveal anomalous cooling over the warm pool and anomalous warming in the east (Figs. 3.7a, b). This suggests that the surface heat flux cannot explain the stronger warming in the west compared to the east (Table 3.1), but rather represents a damping. This implies that the cause of the warming in the west during the two warm epochs must be explained by ocean dynamical processes. Following *DiNezio et al.* [2009], the contributions of the vertically integrated meridional (Q_v), vertical (Q_w) and zonal (Q_u) ocean dynamical heatings are investigated in the upper 300m (H) using equations 3.1, 3.2 and 3.3 respectively:

$$Qv = \rho c \int_{-H}^0 v \frac{\partial T}{\partial y} dz \dots\dots\dots 3.1$$

$$Qw = \rho c \int_{-H}^0 w \frac{\partial T}{\partial z} dz \dots\dots\dots 3.2$$

$$Qu = \rho c \int_{-H}^0 u \frac{\partial T}{\partial x} dz \dots\dots\dots 3.3$$

where $\rho c = 4.1 \times 10^6 \text{ J m}^{-3} \text{ K}^{-1}$, c the specific heat capacity of water, and ρ the density of water.

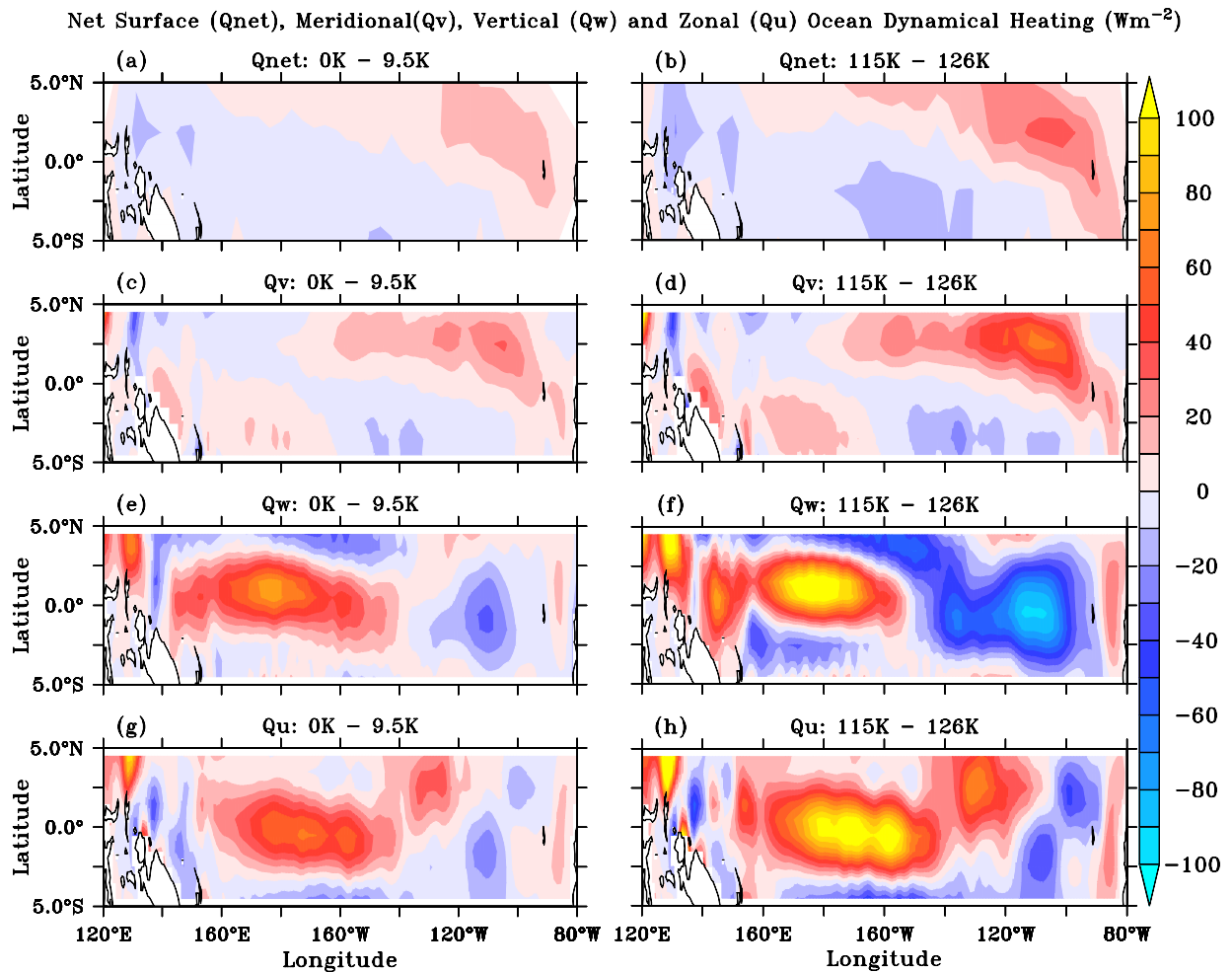


Figure 3.7: Holocene (left) and Eemian (right) trends of the (a, b) net surface heat flux (Q_{net}), (c, d) Meridional (Q_v), (e, f) vertical (Q_w) and (g, h) zonal (Q_u) ocean dynamical heating (Wm^{-2}) over water in the Tropical Pacific. Positive values are directed into the ocean.

The spatial patterns of the net surface heat flux (Figs. 3.7a, b) and Q_v (Figs. 3.7c, d) are similar and do not depict strong changes along the Equator. Thus both cannot explain the enhanced Equatorial zonal temperature gradient change. The term Q_w shows stronger ocean dynamical cooling through vertical advection in the EEP and a warming tendency to the west in the 0K (115K) when

compared to the 9.5K (126K) (Figs. 3.7e, f). Further, the distribution of Qu is similar to that of Qw (Figs. 3.7g, h). Therefore, the conclusion is that it is the zonal heat advection (Qu) in concert with the vertical heat advection (Qw) that cause the west-east asymmetry in the SST-trends during the two warm periods. The effect is stronger during the Eemian compared to the Holocene, which is consistent with the stronger insolation forcing during the Eemian.

In order to investigate the changes in the upper ocean in more detail, the analyses of the temperature and vertical velocity structure in the vertical plane parallel to the Equator are carried out (Fig. 3.8). The upper two panels (Figs. 3.8a, b) show the mean temperature in the x-z section along the Equator for 0K and 115K, respectively. The middle two panels (Figs. 3.8c, d) depict the temperature anomalies (0K minus 9.5K and 115K minus 126K, respectively). No clear signal in the thermocline structure along the Equator is found. However, the vertical velocity shown in the lower two panels (Figs. 3.8e, f) displays a clear pattern, with enhanced vertical velocity in the east and reduced vertical velocity in the west. This supports the development of an enhanced Equatorial zonal SST gradient. The major contribution to the latter is from the west, where the temperature increase is on the order of 1°C , whereas the surface ocean warms considerably less to the east. The conclusion is that the increase in the WPWP SST is the main reason for the increasing ENSO variability over time, because the diabatic heating in this region is strongly dependent on the mean SST [Zebiak and Cane, 1987]. For instance, the regression of Niño4 zonal wind stress anomalies on Niño3 SST anomalies amounts to about $0.0053 \text{ Pa}^{\circ}\text{C}^{-1}$ in 115K, while it is reduced to $0.0047 \text{ Pa}^{\circ}\text{C}^{-1}$ in 126K (Fig. 3.6b, d). This indicates a stronger wind stress sensitivity to SST anomalies with higher mean temperatures in the 115K compared to the 126K. The corresponding change in the SST variability between the two time slices as expressed by the standard deviation of the Niño3 SST anomalies is of the order of 20% (see Table 3.1). Although the change in the wind stress sensitivity cannot account for all the changes in ENSO variability, it is obviously a major contributor.

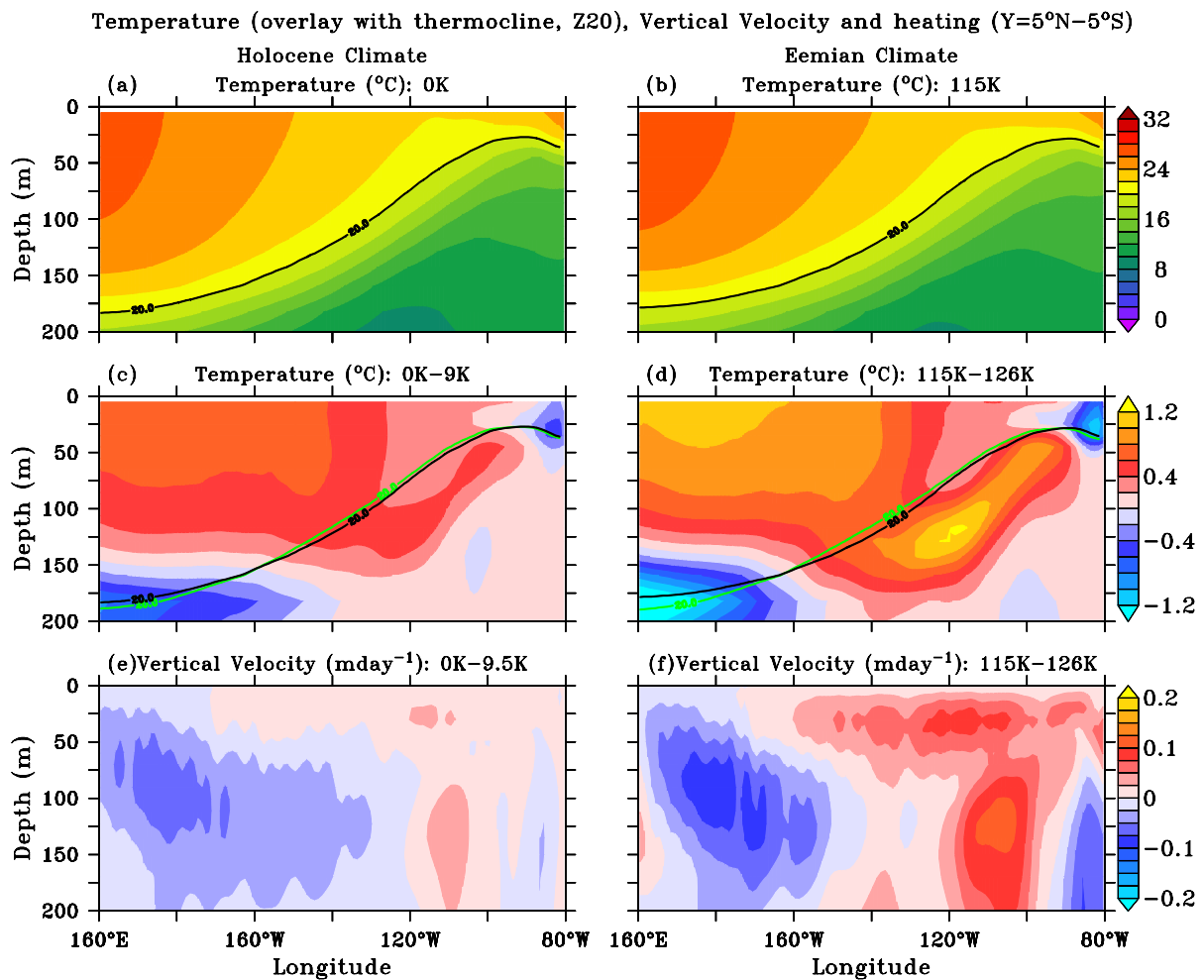


Figure 3.8: Holocene (left) and Eemian (right) depth-longitude variations in the (a, b) mean temperature (0K, 115K), (c, d) the trends of the temperature overlay with the Z20 depths and (e, f) trends of vertical velocity with positive values indicating upward anomalies. The Z20 lines with green and black colours represent the early and late Holocene (Eemian), respectively.

3.2 Changes in the Simulated ENSO

3.2.1 Changes in the Simple Indices

The spectral power of the Niño3 SST anomalies varies only slightly among the time slice simulations, keeping the peak within the 3–4 years frequency band, as in the observation (Fig. 3.9). Also, higher statistical moments such as skewness and kurtosis exhibit only minor variations amongst the different simulations (Table 3.2). The ENSO amplitude increases with time during both periods with larger amplitude in the Eemian simulations where the applied forcing is higher compared to the Holocene. According to a Student's t-test using 50-year chunks, the changes between the respective early and late phases (Holocene and Eemian) are statistically significant at the 95% level. Consequently, the representation of ENSO in our time slice experiments is rather stable with regard to frequency, but a clear trend towards increasing amplitudes over the course of the Holocene and the Eemian is simulated (Table 3.2). While there is no awareness of any robust paleo data for the Eemian ENSO at the time of this study, this result is in good agreement with HadISST (1950-1999) data (Fig. 3.9).

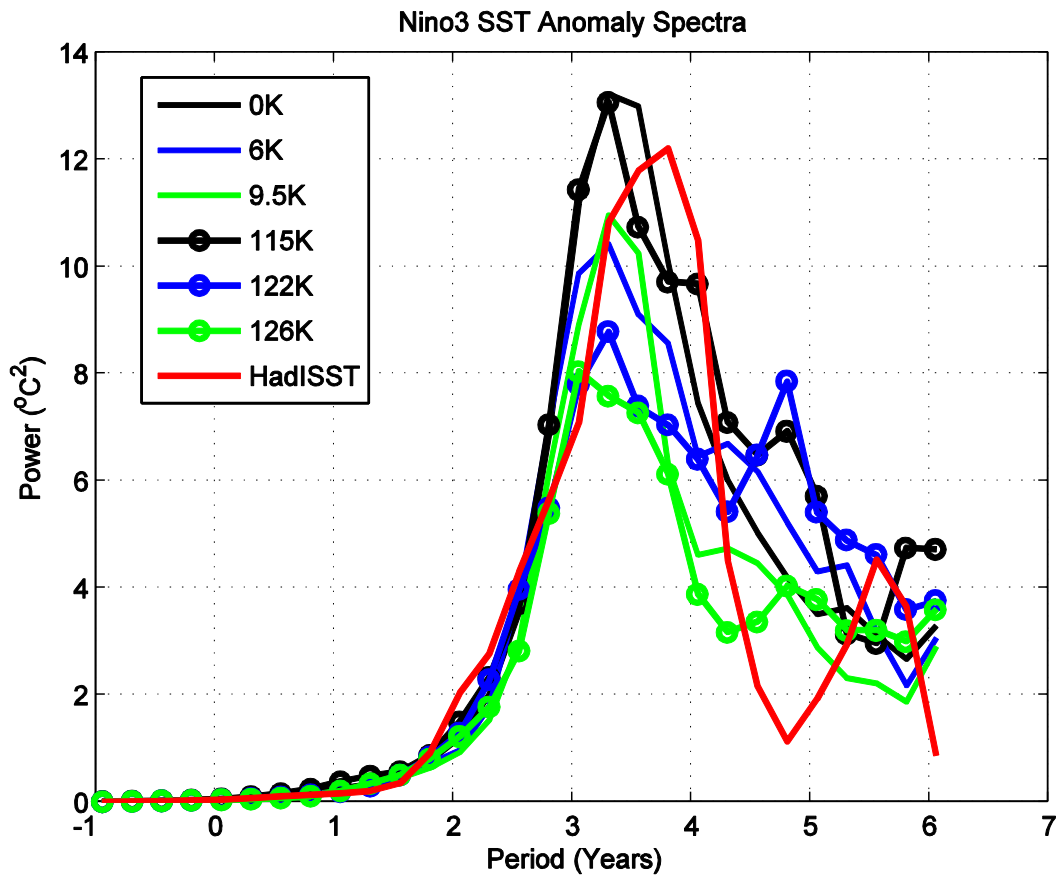


Figure 3.9: The spectra ($^{\circ}\text{C}^2$) of de-seasonalized monthly Niño3 SST anomalies. The Holocene climates are shown by full lines while circles are included in the Eemians for the respective early (green), middle (blue), and late (black) phases; the red line stands for the HadISST data.

Table 3.2: The annual mean values of excess kurtosis, skewness and ENSO amplitude (as in Table 3.1) from Niño3 SSTA and the annual mean Sea level Pressure (SLP) over the Tropical Pacific ($120^{\circ}\text{E}:80^{\circ}\text{W}$, $5^{\circ}\text{N}:5^{\circ}\text{S}$). Attached errors are one standard error obtained using 50 years chunk.

Time Period	0 K	6 K	9.5 K	115 K	122 K	126 K
#Excess Kurtosis	0.10	-0.07	0.03	0.09	0.41	0.20
Skewness	0.12	0.04	0.11	0.02	0.11	0.04
ENSO Amplitude, $^{\circ}\text{C}$	0.91 ± 0.03	0.86 ± 0.02	0.81 ± 0.03	0.94 ± 0.03	0.84 ± 0.02	0.77 ± 0.03
Sea Level Pressure, Pa	100898	100910	100914	100896	100915	100920

#Excess Kurtosis = Kurtosis - 3; where 3 is the kurtosis for standard normal distribution. The definition is used so that the standard normal distribution will have a kurtosis of zero.

3.2.2 Link to the Mean State Change

The ENSO amplitude and the Tropical Pacific mean state depict a clear linear behavior, the ENSO amplitude increases with (1) rising annual mean SST averaged over both the Niño3 and Niño4 regions

(Fig. 3.10a), (2) with an increased west-east (Niño4 minus Niño3) annual mean SST gradient (Fig. 3.10b), and (3) with an enhanced amplitude of the seasonal SST cycle in the Niño3-box (Fig. 3.10b). Furthermore, the ENSO amplitude intensifies with reduced annual mean zonal easterly wind stress in the Niño4-box (Fig. 3.10c) and with increased zonal wind stress in the Niño3-box. However, there is no clear relationship with the Equatorial Pacific upper ocean heat content, as expressed by the depth of the 20°C-isotherm (Fig. 3.10d, see also Figs. 3.8a, b). This indicates that in the KCM simulations, the ENSO amplitude changes mostly originate from surface layer processes. This is in accordance with *Guilyardi* [2006], where most of the reported models were locked in the surface (SST-) mode [*Neelin et al.*, 1998] while it also agrees with the general notion that ENSO is best described as a mixed subsurface/surface layer mode [see *Neelin et al.*, 1994].

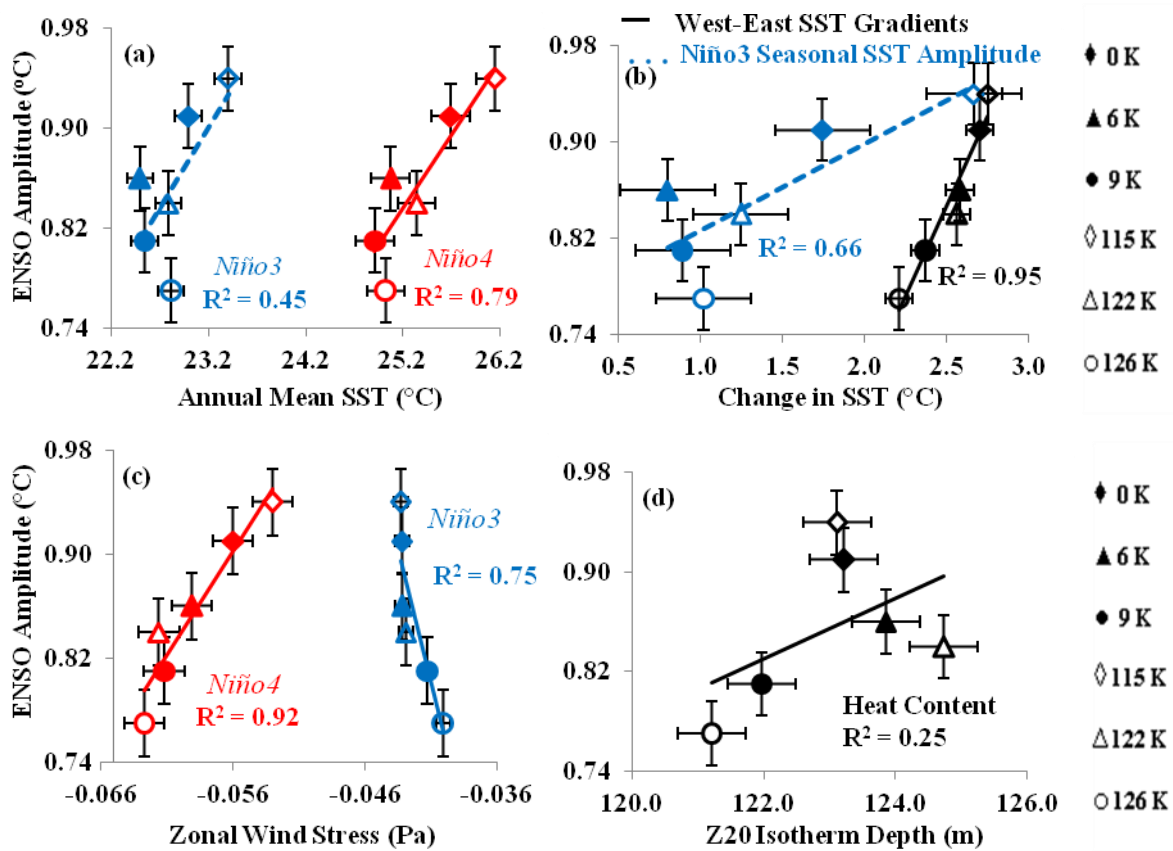


Figure 3.10: Relationships between the ENSO amplitude (°C) (y-axis) and (a) the annual mean Niño3 (blue) and Niño4 (red) SSTs, (b) SST zonal gradient (Niño4-Niño3; black) and Niño3 SST seasonal amplitude (maximum-minimum Niño3 SST; blue), (c) Niño3 and Niño4 zonal wind stress, and (d) the averaged Niño3 and Niño4 Z20 depth (as approximation for heat content), respectively. Filled diamonds, triangles and circles stand for the early-, mid- and late-Holocene periods, respectively, while the corresponding periods in the Eemian are represented by open symbols. The error bars correspond to 1 standard error while the easterly wind stress is stronger as it becomes more negative.

Also, the ENSO amplitude increases as the Z20 depth deepens (shoals) in the eastern (western) Pacific in response to eastward extension of the warm pool while the overall west-east Z20 gradient

weakens over time (Fig. 3.11a). A strengthening of ENSO amplitude is accompanied by weakening of SLP, the SLP is stronger in the eastern Pacific compared to the west (Fig. 3.11b, Table 3.2). However, the overall results show that the absolute temperature in the Equatorial Pacific seems to be a key parameter controlling the ENSO amplitude in the KCM (Fig. 3.10a). The stronger positive correlation between the ENSO amplitude and the Niño4 SST ($r=0.89$) compared to the correlation of ENSO amplitude with the Niño3 SST (Fig. 3.10a) suggests that the WPWP region is a suitable area to reconstruct ENSO strength during the past. One reason for the higher SST sensitivity to orbital forcing in the Western Equatorial Pacific (WEP) relative to the EEP is that in the latter the insolation-induced SST warming is damped by increased upwelling [Zebiak and Cane, 1987] while there is enhancement of the initial seasonal SST warming in the west [Liu, 1998; Liu et al., 2003]. As a consequence, the zonal west-east SST gradient increases over both the Holocene and the Eemian and this yields an even higher correlation with the ENSO amplitude ($r=0.97$) than with the Niño4 SST only (Figs. 3.10a, b).

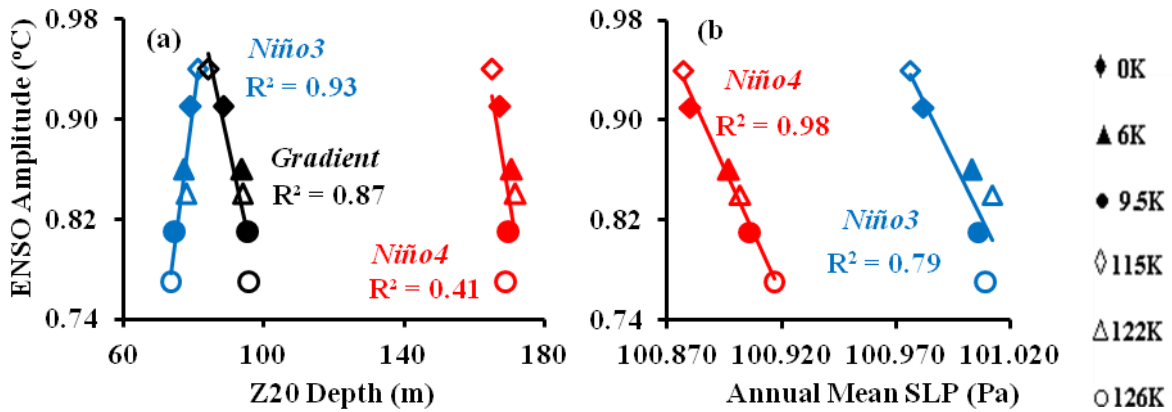


Figure 3.11: The relationship between the simulated ENSO amplitude and the Niño3, Niño4 (a) Z20 depth (m), west-east Z20 gradient and (b) annual mean sea level pressure, SLP (Pa). Colour codes as in Figure 3.10.

3.3 Relationship between the Mean State and Changes in the Atmospheric Circulation

3.3.1 Relationship with seasonal changes in the SST and Zonal Wind Stress

The variations in the mean state is further investigated by comparing the SST and zonal wind stress changes on the seasonal time-scale (Figs. 3.12a-d) which linked the basin-scale anomalies of the SSTs to the corresponding changes in the surface radiation balance (Figs. 3.13a-d) [Liu et al., 2003]. Against the negative insolation anomalies during the 0K (115K) boreal summer (Figs. 3.13a-c, b-d), the model shows a warming trend in the central Pacific with respect to the 9.5K (126K) (Figs. 3.12a, c). The rise in the SST in the 0K (115K) might be due to the weaker wind stress (Figs. 3.12b, d) and reduced evaporative cooling in the central Pacific in the 0K (115K) compared to the 9K (126K). Also, there are extremes of positive (negative) SST changes in the western and eastern Pacific during the boreal winter-spring (summer-autumn) (Figs. 3.12a, c). The changes are induced by variations in the seasonal

strength of trade winds across the Pacific with strongest changes in the western part (Figs. 3.12b, d). Thus, the positive relationship between the SST and zonal wind (*Bjerknes*, [1969] feedback) indeed operates on the seasonal time-scale. Similarly, the increased trade winds in the eastern Pacific in the 0K (115K) with respect to the 9.5K (126K) result in a stronger evaporative cooling and lower SST in the eastern Pacific from the 0K (115K) compared to the 9.5K (126K). This effect together with the equatorward Ekman heat transport might also favour the increased west-east SST gradient in the 0K (115K) compared to the 9.5 K (126K).

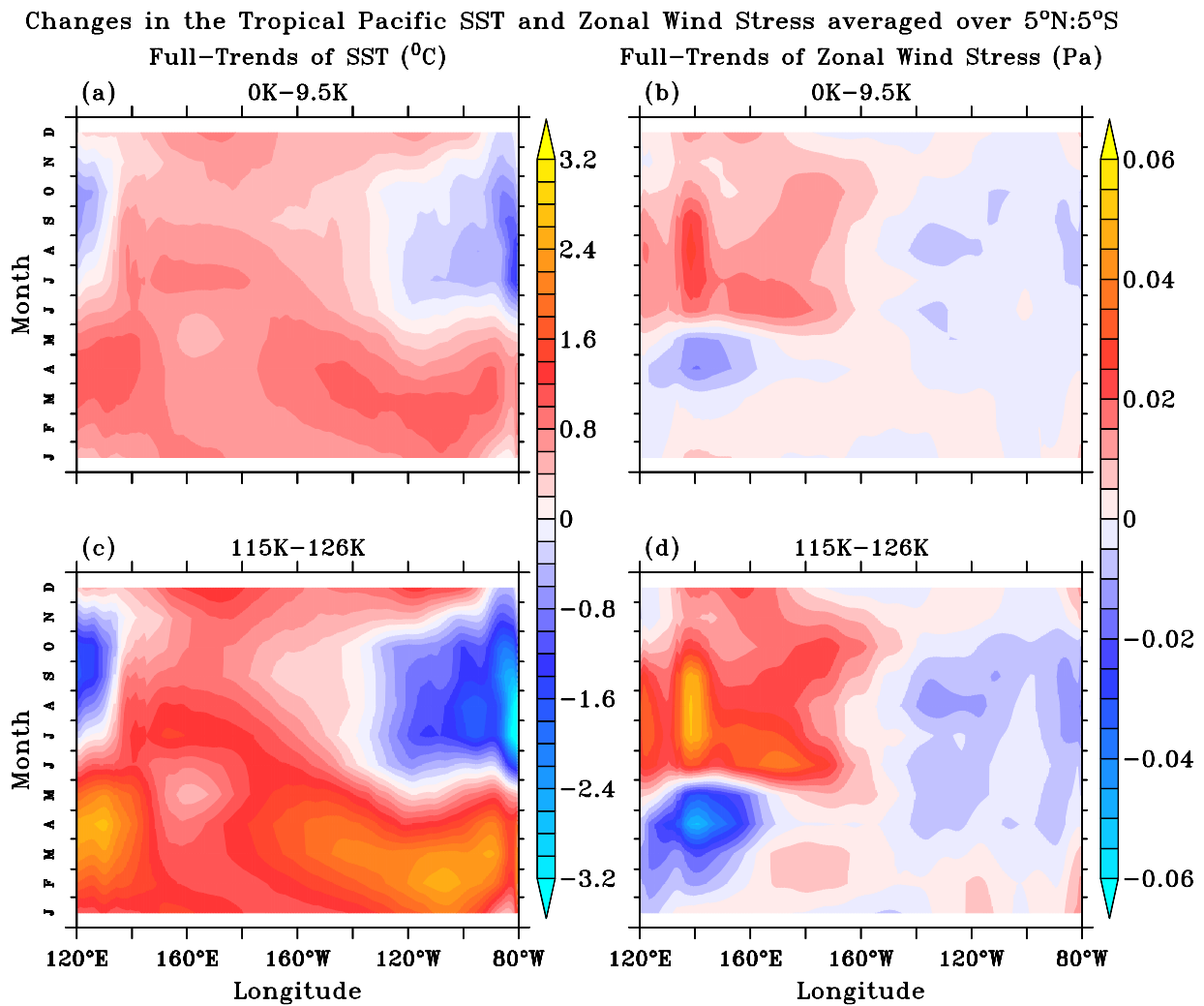


Figure 3.12: Hovmoeller diagram of the full-Holocene trend (FHT) and full-Eemian trend (FET) for the intra-annual variations of SST (°C; a, c) and zonal wind stress (Pa; b, d) averaged along the Equator (5°N:5°N).

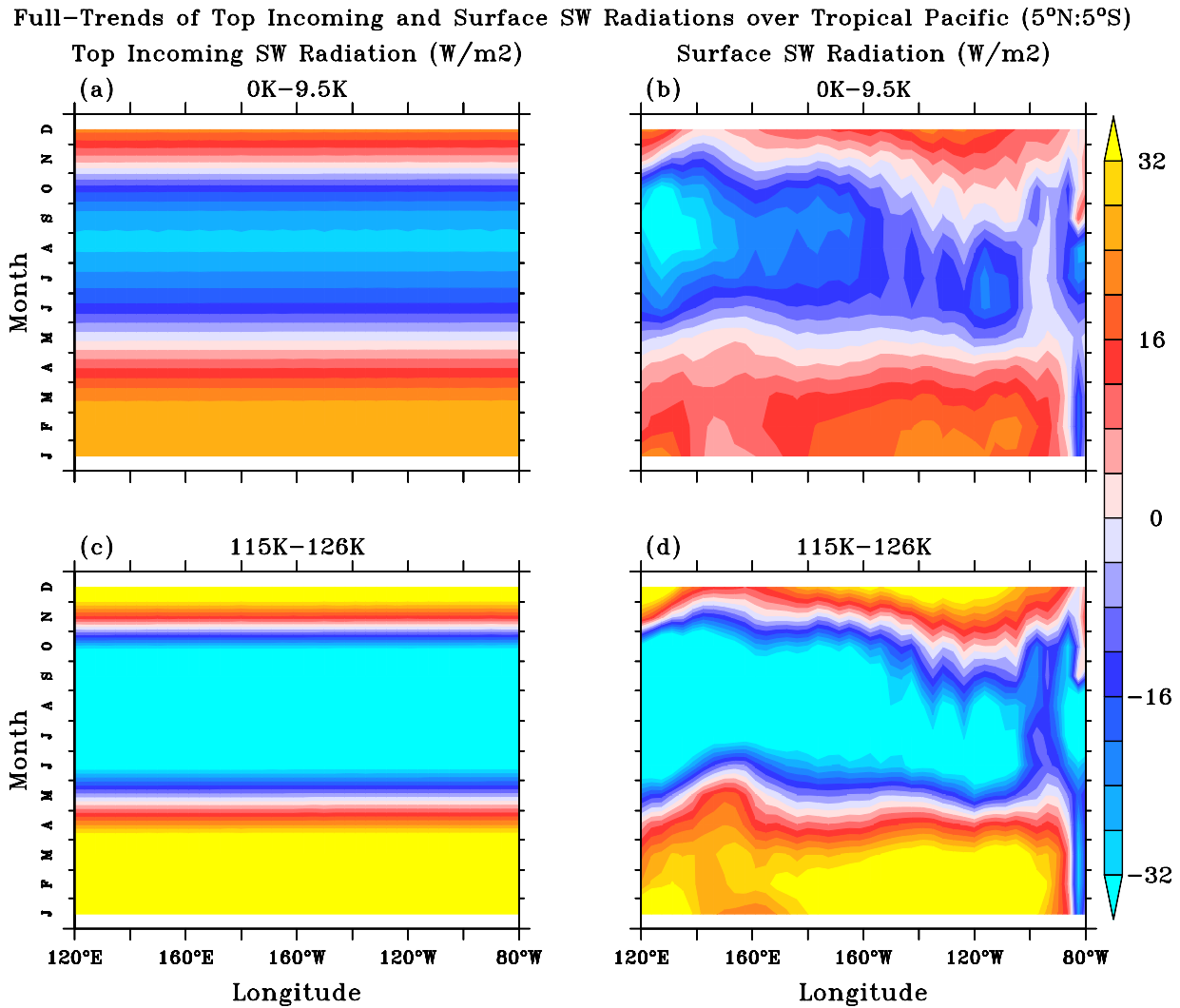


Figure 3.13: Hovmoeller diagram of the FHT and FET for the TOA short wave radiation (a, c), and the Surface Short Wave Radiation which has been modified by ocean dynamic through air-sea coupling (b, d) averaged along the Equator (5°S-5°N).

3.3.2 Changes in the Velocity Potential and Walker Circulation

The strengthening of the west-east SST gradient over time is further analysed through the simulated changes in the atmospheric circulation. The wind stress response pattern during the Holocene (0K minus 9.5K; Fig. 3.14a) and the Eemian (115K minus 126K; Fig. 3.14b) indicates a strong meridional (Ekman) convergence of warm surface waters in the western half of the upper Equatorial Pacific. The low-level velocity potential simulated in the 0K is shown in Fig. 3.15a, depicting, as expected, a strong convergence of air masses in the WPWP region as, indicated by the strong maximum there. In contrast, the EEP features a divergence of air masses. Differences of the velocity potential during the Holocene (0K-9.5K; Fig. 3.15c colour shading) and the Eemian (115K-126K; Fig. 3.15e colour shading) are consistent with the corresponding SST changes shown in Figure 3.14a and 3.14b, respectively. The changes in the velocity potential include an anomalous convergence in the Central

Pacific peaking at about 160°W in both cases (Figs. 3.15c, e colour shading). The changes in SST and velocity potential are stronger during the Eemian (Fig. 3.14b; Fig. 3.15e) compared to those during the Holocene (Fig. 3.14a; Fig. 3.15c). This is due to the pronounced influence of the higher eccentricity during the Eemian on the strength of the precession forcing, whereas the spatial response patterns remain very similar. The anomalous convergence in the Central Pacific is mainly due to an eastward expansion of the WPWP in both 0K and 115K (Figs. 3.15c, e; black contours), very much as during El Niño events.

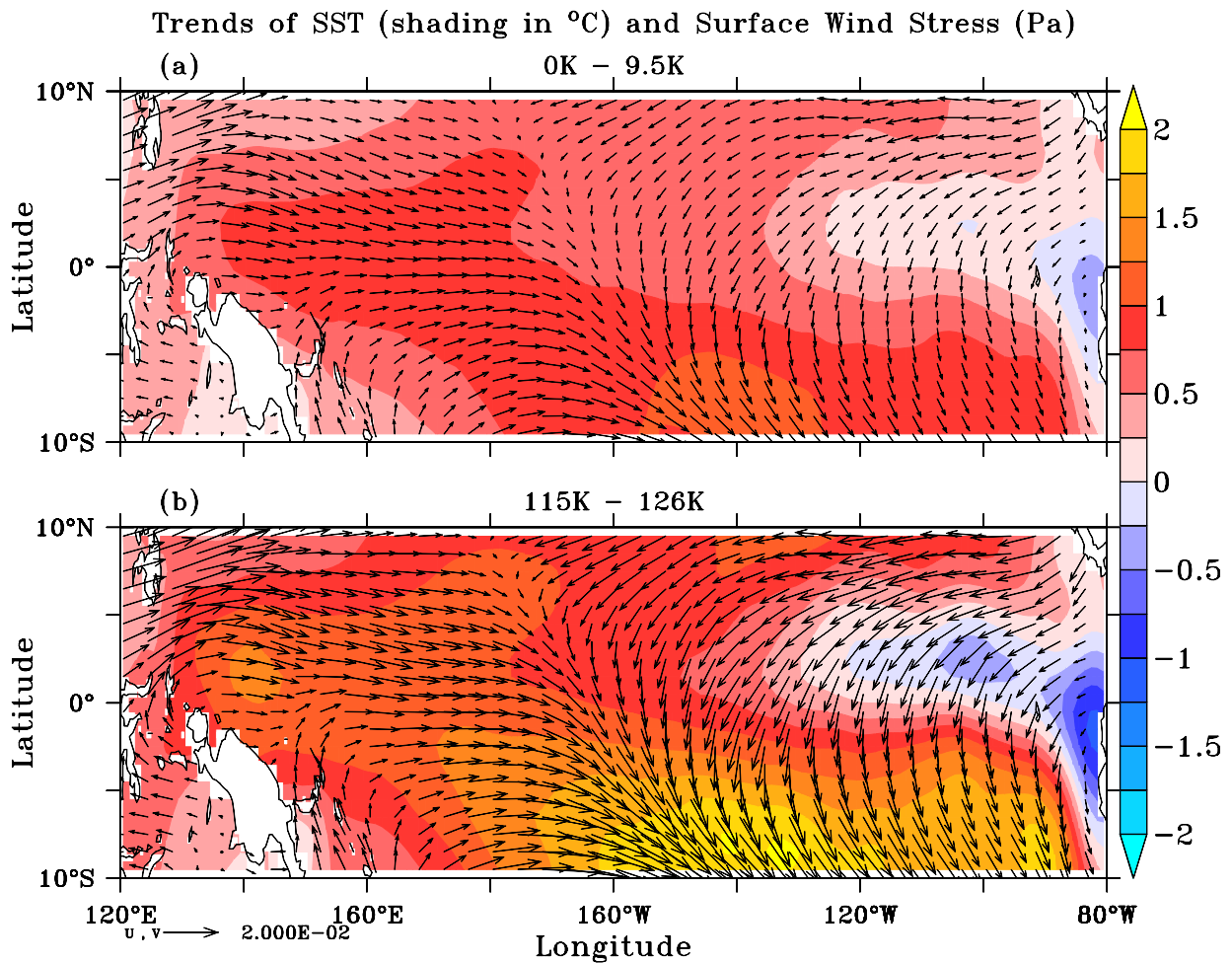


Figure 3.14: Difference of SST (°C) (shading) and surface wind stress (Pa) between two periods in (a) the Holocene (0K minus 9.5K) and (b) the Eemian (115K minus 126K).

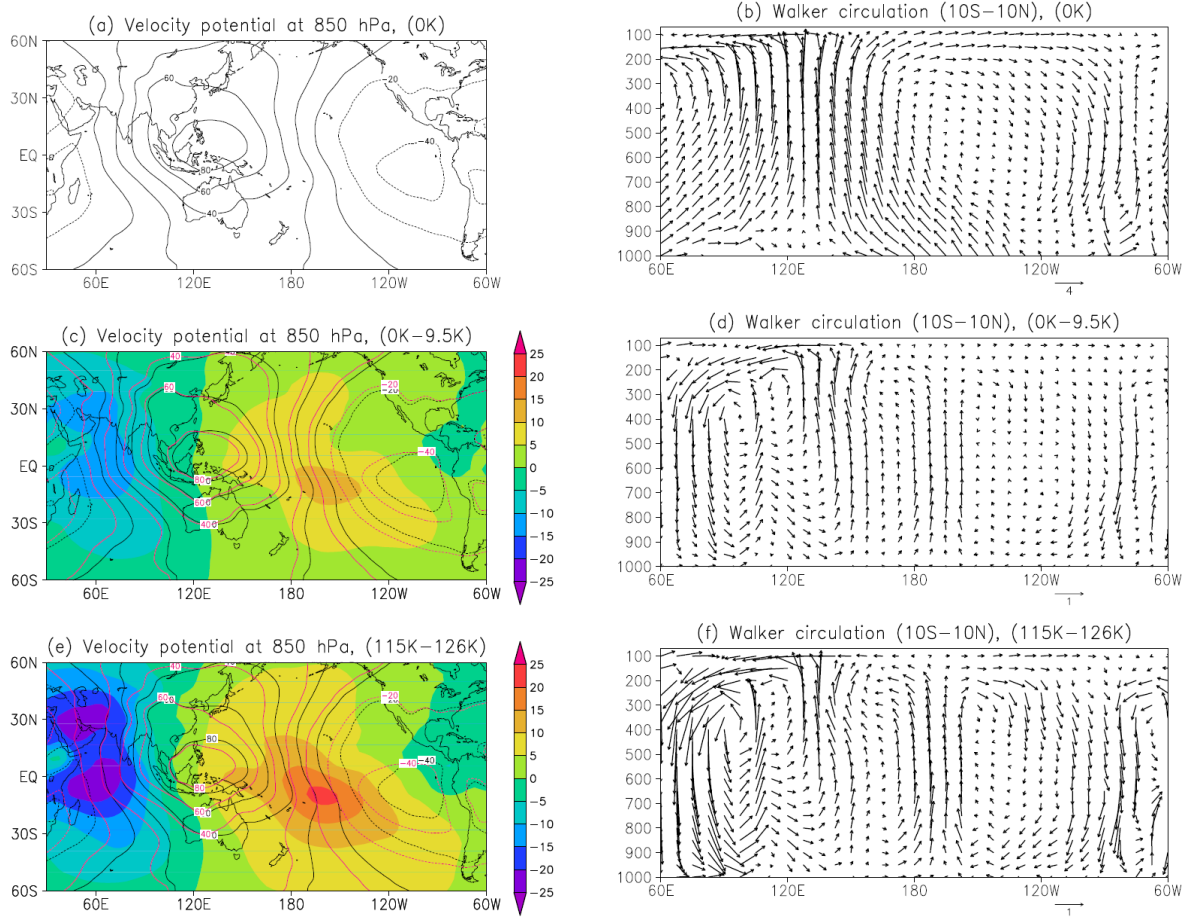


Figure 3.15: Annual mean 850hPa velocity potential [$10^6 m^2 s^{-1}$] and (b) zonal-vertical circulation for the preindustrial simulation (0K). The zonal-vertical circulation is shown by averaging divergent wind [$m s^{-1}$] and vertical velocity [$10^{-4} hPa s^{-1}$] between $10^\circ S$ and $10^\circ N$. (c) Holocene trend (0K minus 9.5K; shaded) of the mean 850 hPa velocity potential, overlay by the annual mean contours of the preindustrial (0K; black) and early Holocene (9.5K; red), and (d) that of the zonal-vertical circulation. (e) Eemian trend (115K minus 126K; shaded) of the mean 850 hPa velocity potential, overlay by the contours of the late Eemian (115K; black) and early Eemian (126K; red), and (d) that of the zonal-vertical circulation.

The associated zonal (Walker) circulation changes are shown as averages over the Equatorial region ($10^\circ S$ - $10^\circ N$). They depict in 0K the familiar pattern with upward motion over the WPWP centered at about $130^\circ E$ and subsidence further to the east (Fig. 3.15b). The estimate of the Walker circulation (WC) strength (based on the maximum value of the velocity potential over the western Pacific) does not show strong changes from the early to the late Holocene (Eemian) (Figs. 3.15c, e). However, there is a substantial eastward shift of the area of strong upward motion (seen as anomalous upward motion in Figs. 3.15d, f), which is indicated by the shift of the zero-contours in Figures 3.15c and 3.15e. This implies a reduction of the easterlies in the Western Pacific and a corresponding strengthening in the Eastern Pacific (Figs. 3.15d, f), while the total strength of the Walker circulation remains rather constant, exhibiting changes of less than 5%.

3.3.3 Changes in the Tropical Pacific Mean State and the North-South Migration of ITCZ

These KCM results indicate that the simulated ENSO amplitude increases over time as the precession-induced northernmost mean positions of the ITCZ in the 9.5K and 126K migrate southward over both epochs. The southward shift of the ITCZ in 0K (115K) over the Equatorial Pacific (120°E-80°W) is accompanied by a reduction in the annual mean meridional gradient of SST (12°N-5°N minus 12°S-5°S) (Table 3.3) [see also *Timmermann et al.*, 2007]. The corresponding changes in the meridional SST gradients are stronger in the Eastern Pacific compared to the values in the west and over the entire Equatorial Pacific (Table 3.3), however, the meridional SST gradient is strongly correlated with ENSO amplitude in both cases (Fig. 3.16a). The higher meridional SST gradient in the east compared to the west is due to the more northern position of the ITCZ in the east, favouring an intensification of cross Equatorial southerlies over the EEP [*Mitchell and Wallace*, 1992; *Xie*, 1994] and more upwelling (Fig. 3.16b). The southward shift of the mean northern position of the ITCZ is also supported by the reduction in the SST over the NH in the 0K and 115K, where boreal summer occurs at aphelion.

Table 3.3. The meridional SST gradient estimated from the annual mean SST over the NH (12°N-5°N) minus SH (5°S-12°S) and averaged over 120°E-80°W. Also shown are the annual mean values of the cloud cover, precipitation over the Tropical Pacific (120°E-80°W, 5°N-5°S) and within the Niño3 and Niño4 boxes along with the west-east gradient of atmospheric water vapour, AWV (kgm⁻²).

Time Period	0 K	6 K	9.5 K	115 K	122 K	126 K
Meridional SST Gradient, °C	0.591	0.654	0.788	0.386	0.626	0.854
Cloud Cover, %	0.594	0.580	0.575	0.600	0.573	0.568
Precipitation, mm/day	3.122	2.872	2.860	3.273	2.825	2.920
Niño3 Precipitation, mm/day	0.585	0.568	0.632	0.589	0.537	0.686
Niño4 Precipitation, mm/day	1.799	1.517	1.498	1.974	1.485	1.579
West-East AWV, Kgm ⁻²	4.81	4.22	3.53	5.45	4.66	3.24

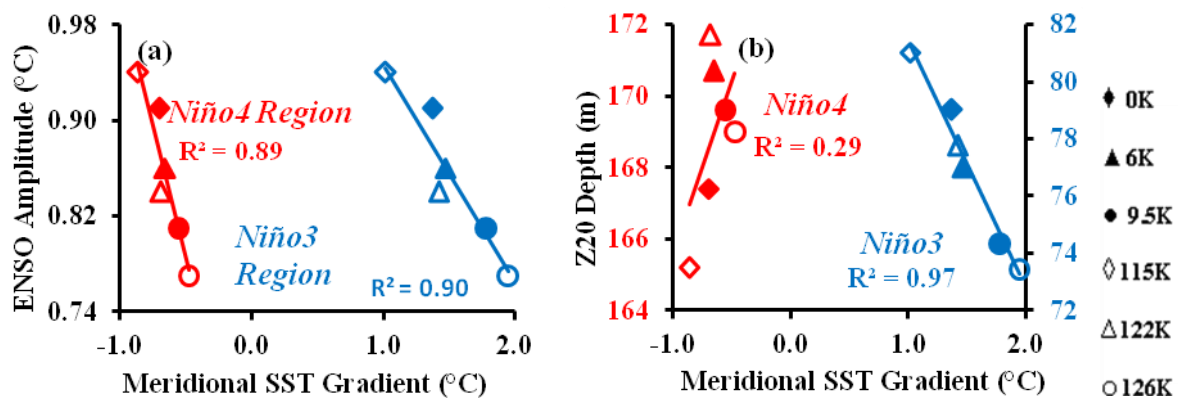


Figure 3.16: The (a) ENSO Amplitude, (b) Niño3 and Niño4 Z20 depth plotted against the annual mean meridional SST gradient (12°N:5°N-5°S:12°S) averaged over the (a) Niño3 (150°W:90°W), Niño4 (160°E:150°W) regions.

As a band with the maximum SST (Figs. 3.17a, b), the spatial distribution of the ITCZ shows that the more Northern position in the Eastern Pacific is sustained by the enhanced heating from the larger land mass in the region compared to the west where the expansion of the land mass is more southward. The SST distribution has a wider spatial coverage of the ITCZ in the warmer 0K (115K) compared to that of the 9.5K (126K) which also has its ITCZ enclosed within that of the former. Along the latitude, the mean position of the ITCZ migrates north and south following the Sun, lagging the Sun by about two months with the Northern (Southern) extreme occurring in September (March) (Figs. 3.17c, d) [see also Xie *et al.*, 2007]. In addition, the ITCZ reaches more Northern (Southern) positions in the 9.5K and 126K (0K and 115K) during September (March) period. The southward migration of the mean Northern position of the ITCZ rises (reduces) as the SST lowers (enhances) in the NH in both 0K and 115K (9.5K and 126K) where the perihelion occurred in boreal winter (late summer) (Fig. 3.17e). Hence, the southward shift of the ITCZ location over time in both epochs is in favour of the intensification of the annual mean SST in the Eastern Pacific while the resulting ENSO variability strengthens.

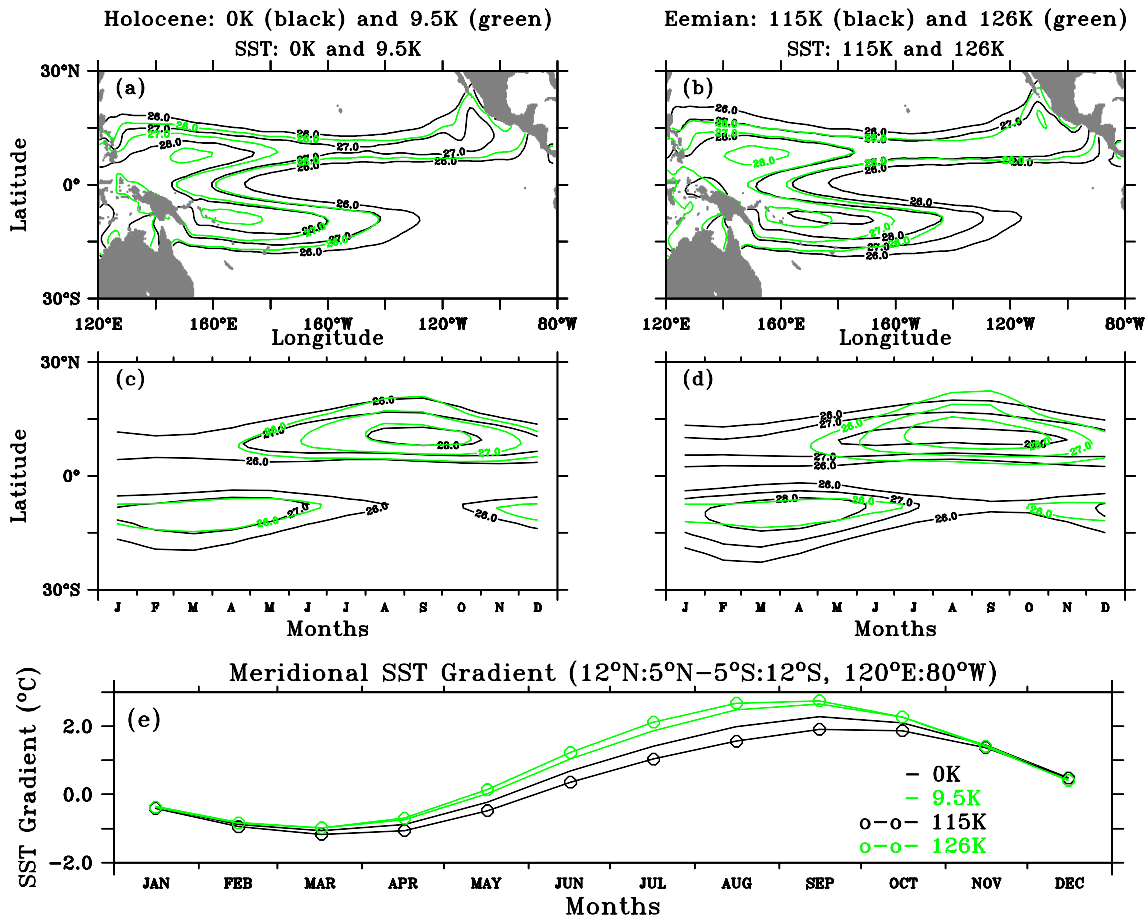


Figure 3.17: The figure shows the spatial distribution of the SSTs between 26°C to 30°C (contour interval 1°C) as an indicator for the ITCZ position along the (a-b) latitude-longitude, (c-d) latitude-time, and (e) the annual cycle of the meridional SST gradient over the Tropical Pacific (120°E:80°W) using the extreme climates in the Holocene and Eemian for clarity.

3.3.4 Simulated Changes in the Cloud Cover, Precipitation and Water Vapour

A linear relationship is simulated between the north-south SST asymmetry and the annual mean meridional cloud cover (Fig. 3.18) while the accompanying ENSO amplitude weakens [see also *Timmermann et al.*, 2007]. Also, the meridional precipitation gradient mainly increases with the corresponding increase in the meridional SST gradient, however, the correlation is weaker compared with that from cloud cover (Fig. 3.18). This is consistent with the similarity between the annual cycle of the meridional SST gradient and that of the cloud cover over the Tropical Pacific (not shown). In agreement with changes in the meridional SST contrast and the overall SST distribution, low magnitudes of the cloud cover (contour) and the precipitation (shading) are simulated in the north-eastern Equatorial Pacific from the 0K (115K) compared to the 9.5K (126K) (Figs. 3.19a, c). On the other hand, both the mean cloud cover and the precipitation intensify in the 0K and 115K above the respective magnitudes in the 9.5K and 126K over the SH, near the equator and strongly in the warmer western Pacific where deep convection is higher compared to the east (Figs. 3.19a, c).

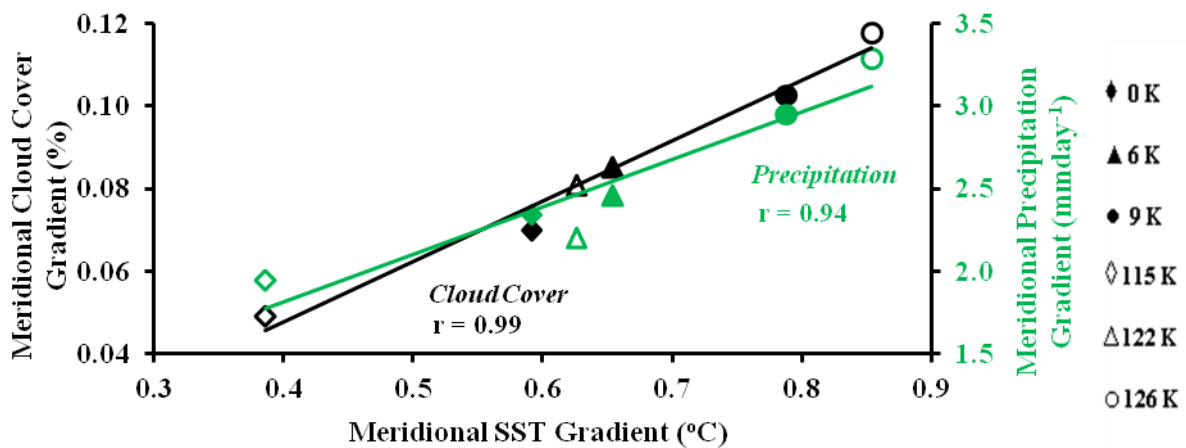


Figure 3.18: The relationship between meridional (12°N - 5°N minus 5°S - 12°S) SST gradient and both cloud cover and Precipitation (mmday^{-1}) averaged over the Tropical Pacific (120°E - 80°W).

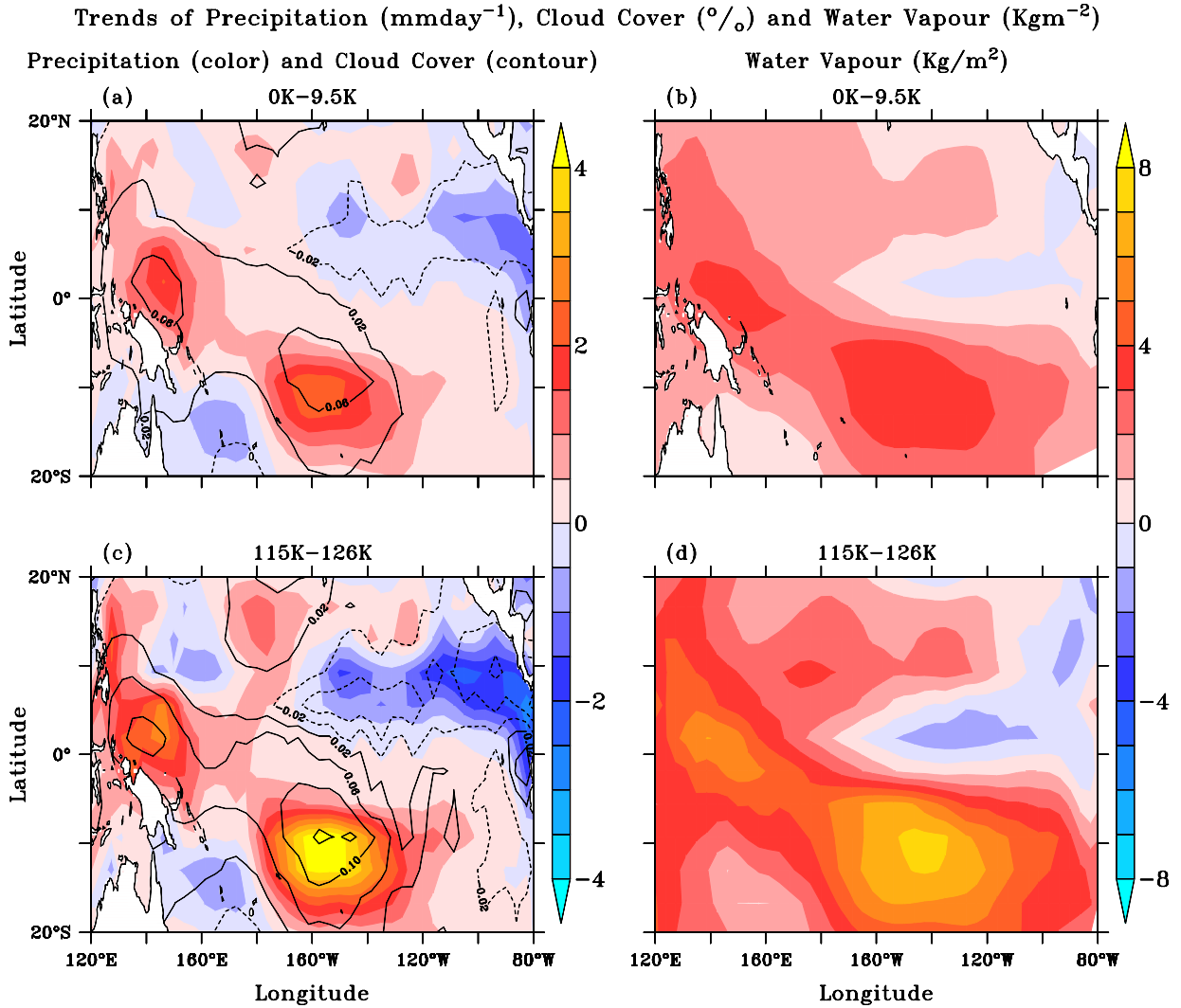


Figure 3.19: The (a) FHT and (c) FET of the simulated precipitation (in mmday^{-1} ; colour shading) and cloud cover (contour, interval=0.04) while FHT and FET for water vapour (Kgm^{-2}) are shown in (b) and (d) respectively.

A linear relationship is obtained between the ENSO amplitude and the annual mean atmospheric water vapour (AWV) over the entire Equatorial Pacific (not shown) and with the west-east gradient of the AWV where the correlation is also high ($R^2=0.90$) (Table 3.3). The spatial coverage of the SST over the warm pool (Figs. 3.14a, b) is well mirrored by the simulated AWV (Figs. 3.19b, d). With an increase in the SST, the water vapour acts to amplify the initial warming by trapping more heat, the SST further increases with an exponential increasing water holding capacity of the atmosphere [Trenberth, 1998]. For instance, the potential of the AWV feedback to raise the global warming under increased greenhouse gas concentration has been reported by Hall and Manabe [1999]. The latent energy in the evaporated water is released during the cloud and precipitation formation [Buchdahl, 1999]. Thus, the percentage increase in the annual mean SST over the Tropical Pacific ($120^\circ\text{E}:80^\circ\text{W}$, $5^\circ\text{N}:5^\circ\text{S}$) during the transition from early to middle periods in the Holocene (2.3%) and

Eemian (3.2%) comes as heavier rainfall with an annual mean value of 9.2% and 12.1% respectively (Table 3.3). The results show that the SST, cloud cover, precipitation and water vapour share common characteristics in terms of their spatial patterns and magnitudes, their annual mean values are generally higher in the west compared to eastern Pacific where deep convection is low (Table 3.3). Overall, their magnitudes increase as the ENSO amplitude amplifies over time, the strength of the change is larger in the Eemian where the applied forcing is stronger compared to the Holocene (Figs. 3.19a-d).

3.4 Phase Locking of the ENSO Variability to the Annual Cycle

The next analysis is focused on the observed and the simulated Seasonal Phase Lock (SPL) index (amplitude of the monthly stratified standard deviation of Niño3 SSTA). A strong mean SPL index will favour an El Niño development under a weak trade wind while the growth of the El Niño is more hindered as the SPL index reduces [Zheng *et al.*, 2008]. In response to the insolation changes, the result reveals a continuous increase in the monthly ENSO amplitude from November to March with the least amplitudes in the 9.5K (126K) in all cases (Fig. 3.20). The ENSO amplitude declines in April under a low air-sea coupling induced by a more uniform atmospheric heating of the Tropical Pacific when the ITCZ is close to the equator (Fig. 3.16e) [see also Clement *et al.*, 1999]. The amplitude further reduces in May-June (except in 122K and 6K) before a moderate increase in the boreal summer during which the conditions are more favourable for the developments of ENSO event under a high air-sea coupling (see also Fig. 3.12) [Zebiak and Cane, 1987; Otto-Bliesner *et al.*, 2003; Liu *et al.*, 2000]. Afterward, the amplitude attenuates in late boreal summer before strengthening in the late boreal fall through boreal winter to complete the annual cycle.

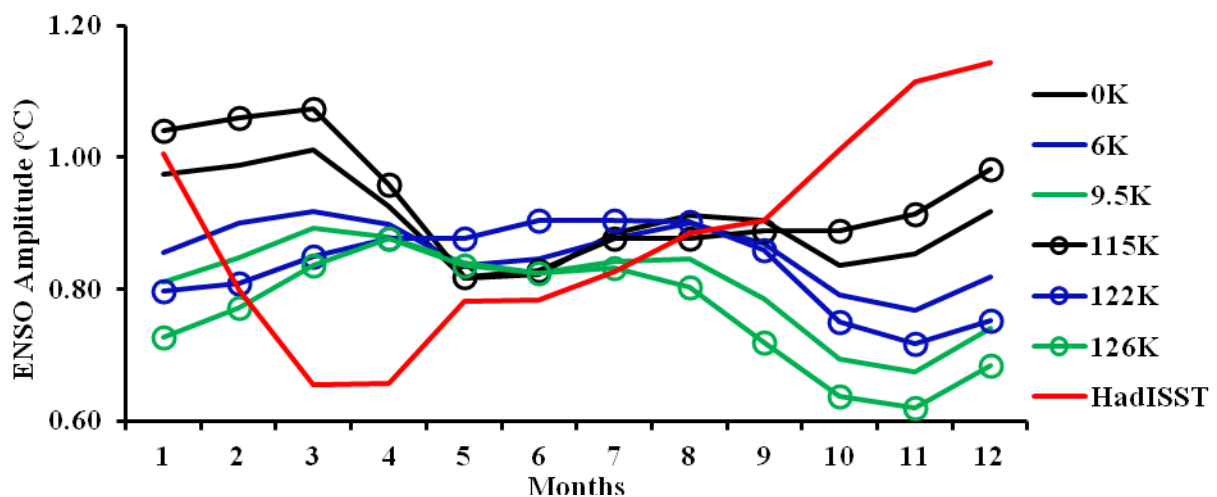


Figure 3.20: The observed (red) and simulated annual cycles of the ENSO amplitude. The early, middle and late Holocene are represented by the black, blue and green colours while the corresponding periods in the Eemian climates are shown with small circles.

In general, the intensification of the anomalous boreal summer warming (cooling) of the eastern Pacific tends to weaken (strengthen) the ENSO amplitude while the amplitude increases during boreal winter warming (Fig. 3.20, Fig. 3.5) [Clement *et al.*, 2000]. Also, an increase in the coupling strength during boreal autumn (when the ITCZ shifts northward) tends to cool the eastern Pacific more than in the west. The condition results in a La Niña-like mean state under amplification of the coupled system by the associated strong easterlies (Bjerknes Feedback). Overall, this result reveals that the weakest (strongest) variability shifts from May (March) in the 0K and 115K to November (March-April) in the other simulations with the exception of 122K which has the peak in June (Fig. 3.20). In comparison with observation (HadISST, 1950-1999) where the variability is lowest in March and highest in December, the simulated ENSOs are not sufficiently phase locked to the end of the calendar year (Fig. 3.20) [see also Park *et al.*, 2009].

3.5 Effect of individual Orbital Parameters on the Mean Climate

When relating the reorganizations in the Tropical Pacific to the individual forcing components (obliquity, precession), the result shows that the overall warming of the Tropical Pacific can be well explained by the decreasing obliquity (Fig. 3.21a) while the ENSO is most sensitive to precessional forcing (Fig. 3.21b). In the WPWP, the warming is also strongly correlated with changes in the precessional index while the ocean dynamical processes also play the key role in the enhanced warming in the west. In general, the simulated changes in the mean state over the Tropical Pacific are similar in the Holocene and the Eemian climates, however, the amplitude of the response is larger in the Eemian due to enhanced impacts of the precession forcing and the increased eccentricity applied compared to the Holocene. The results indicate that the annual mean ENSO amplitude strengthens with shift in the time of perihelion from late boreal summer-autumn to boreal winter-spring over time during both Holocene and Eemian. The absence of irregular response in the ENSO amplitude over both epochs supports the similarities in the evolution of the mean Tropical Pacific climate and the variability in the Holocene and Eemian under the influence of the orbital forcing only.

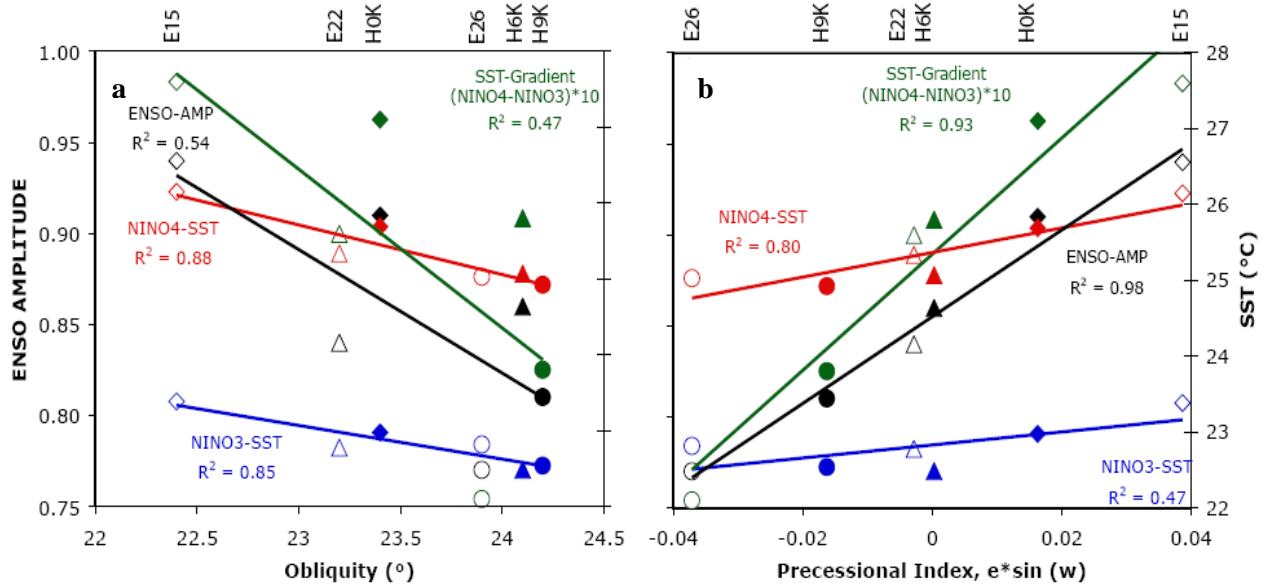


Figure 3.20: Changes in the characteristics of the Tropical Pacific mean state and ENSO versus the individual forcing components: (a) obliquity and (b) precession: ENSO amplitude (black; left scale in both cases), Niño4 SST (red; right scale), Niño3 SST (blue; right scale). Note that the west-east SST gradient (green; right scale) is multiplied by 10 times to match the scale.

3.6 Summary

The KCM simulations have shown that the ENSO amplitude does increase with rising SST over the Tropical Pacific as a result of orbitally-induced insolation changes. The ENSO amplitude also increases with rising equatorial west-east SST gradient and with an enhanced seasonal cycle of the SSTs in the EEP. Overall, the amplified warming of the western Pacific leads to a larger atmospheric heating in the west compared to the east where deep convection is suppressed in response to a cooling feedback from the enhanced upwelling. The intensification of the west-east SST gradient over the Holocene and the Eemian reveals a La Niña-like mean state over the Tropical Pacific. Consequently, the mean state in a cool NH summer can be expected to be more El Niño-Like, which may also be linked to a weak Asian summer monsoon over the Tropical Pacific [see also Liu *et al.*, 2000 and the references therein]. The results shows that the ENSO is best described as a mixed subsurface/surface layer mode while the frequency remains almost constant, peaking at 3-4 years. The higher positive correlation between the SST and the ENSO amplitude in the western Pacific compared to the east suggest that the WPWP region might be a good area to reconstruct ENSO strength during the past.



“Climate change is real. The science is compelling. And the longer we wait, the harder the problem will be to solve.” Senator John Kerry

CHAPTER FOUR

Comparison with other Studies

Recent efforts have been directed towards the synthesis of paleoclimate records so as to provide extensive data coverage for the evaluation of model capacity in capturing the response of climate system to orbital forcing [Jansen *et al.*, 2007]. The data-model comparisons are playing major role in improving model development with increased accuracy. Hence, the comparisons between the simulated Holocene and the Eemian climates with all available observations and model studies are presented in this chapter. The aim is to obtain a clearer understanding of the changes in the simulated mean states and to establish the level of agreements of the KCM results with the observations and other model studies. The chapter has two divisions which feature the comparison of the KCM simulation with observations in the first section while the comparison with other model studies occupied the second part.

4.1 Comparison of KCM Result with Paleo-reconstruction

The simulated mean temperature trend largely agrees with alkenone reconstructions that show a Tropical warming over the Holocene [Kim *et al.*, 2004; Leduc *et al.*, 2010; Schneider *et al.*, 2010]. The mid-Holocene cooling of about 0.6-1.1°C in the EEP has been reported in the SST reconstruction from Mg/Ca ratios in foraminifera [Koutavas *et al.*, 2002; see Otto-Bliesner *et al.*, 2003]. However, the paleo-temperature estimated over the Indo-Pacific warm pool from Makassar Strait [Visser *et al.*, 2003] is shown to be similar in the early-Holocene compared to the present [Otto-Bliesner *et al.*, 2003]. The increasing trend in the ENSO variability is in agreement with observations from the oxygen isotopic $\delta^{18}\text{O}$ composition of coralline aragonite from Papua New Guinea, which shows higher amplitude variability in 118 kyr (std 0.08 permil) than in 128 kyr (0.05 permil) [Tudhope *et al.*, 2001]. According to the report, Tudhope *et al.* [2001] attributed the changes in the ENSO statistics to variations in the seasonal distribution of solar radiation due to fluctuations in the precessional cycle. Also, the highlights of the Tudhope *et al.* [2001] for the past 130 kyr reveal that the intensity and frequency of the ENSO event was reduced in the past compared to the modern time [Cole 2001].

The KCM result on the ITCZ is in agreement with Koutavas *et al.* [2006] who concluded from Mg/Ca thermometry near the Galapagos Islands that a more southward displaced ITCZ in the late Holocene would favour higher El Niño-like instability. Reduced southeasterly trade winds, increased SST and heavy rainfall has been linked to southward shift of the ITCZ in the Holocene reconstruction

from lake sediment in the El Junco part of the Galápagos Islands, the patterns are reversed as the ITCZ moves northward [Conroy *et al.*, 2008]. An enhanced ENSO strength has been found to accompany a decade with anomalously weak Asian monsoon in the observations obtained from locations in India [Krishnamurthy and Goswami, 2000]. Increasing ENSO amplitude reconstructed over the Holocene period from a large numbers of paleo proxies are consistent with the KCM result [Rodbell *et al.*, 1999; Tudhope *et al.*, 2001; Moy *et al.*, 2002; Gagan *et al.*, 2004; Conroy *et al.*, 2008]. These include the paleo reconstructions from the eastern Pacific within Laguna Pallcacocha in Ecuador [Rodbell *et al.*, 1999; Moy *et al.*, 2002], data from Papua New Guinea in the western Pacific [Tudhope *et al.*, 2001] and from locations in the western and eastern Pacific reported by Gagan *et al.* [2004]. In addition, the simulated (KCM) frequency range of 3-4 years lies between the observed 2.5-7 years reported by Meehl *et al.* [2001] and Deser *et al.* [2006].

4.2 Comparison of the KCM Results with Model Studies

The increasing trend in the annual mean temperature over the simulated Holocene climates has been confirmed by other climate models [see Voss and Mikolajewicz, 2001; Lorenz and Lohmann, 2004; Lorenz *et al.*, 2006]. The lower mean SST simulated over the eastern and central Pacific during the mid-Holocene compared to today [Otto-Bliesner, 1999; Liu *et al.*, 2000] is consistent with the fewer strong El Niño events during the mid-Holocene than today as seen in the observation [Rodbell *et al.*, 1999] and in the present study. Likewise, the ENSO amplitude rises over the Holocene in the model studies reported by Zheng *et al.* [2008] and Liu *et al.* [2000] which also linked the damped ENSO variability in the mid-Holocene to the intensification of Asian Monsoon. The result agrees with the strong precessional-related sensitivity of the ENSO in the model studies reported by Clement *et al.*, [1999], Zebiak and Cane [1987] while Zheng *et al.*, [2008] and Timmermann *et al.*, [2007] also linked the changes to variations in the seasonal distribution of solar radiation through fluctuations in the precessional cycle. In addition, the simulated frequency range of 3-4 years is consistent with other model findings [Meehl *et al.* 2006; Zebiak and Cane, 1987]. The overall accuracy of the KCM in simulating ENSO amplitude is revealed by the control simulation (OK) which shows good agreement with the observation (Fig. 4.1). In addition, the KCM performed creditably well among the other complex coupled global circulation models (CGCMs) that have good agreement with the observation in the simulation of ENSO characteristics.

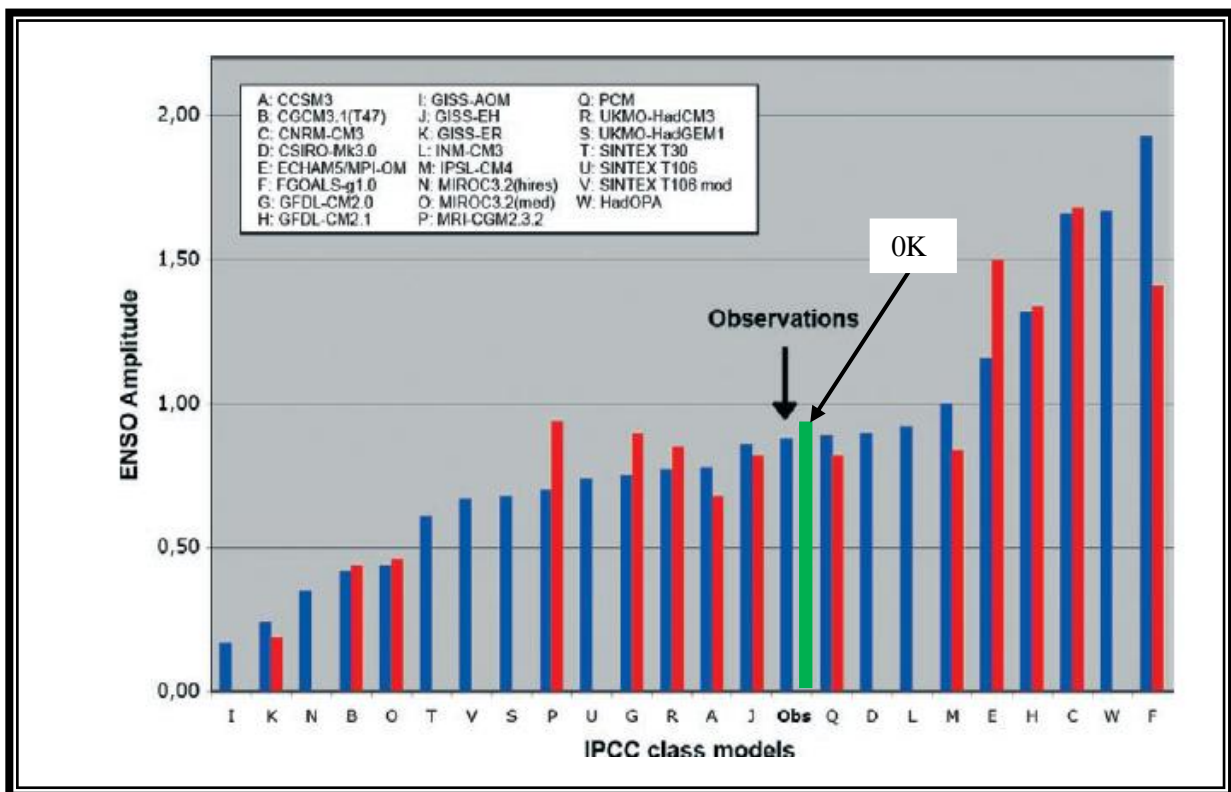


Figure 4.1: The ENSO amplitudes from 0K (green) and other 23 coupled CGCMs (including those used in IPCC AR4). The preindustrial simulations are in blue colour while the red colour stands for the equilibrated $2x$ CO_2 scenarios (adapted from Guilyardi *et al.*, [2009]; Figure 5).

The changes in 6K-0K show that a reduction (increase) in the annual mean Niño3 SST in the 6K (0K) where the Niño4 mean zonal wind stress intensifies (weakens) is in accordance with that presented by Zheng *et al.* [2008] from several model results (Fig. 4.2a). In addition, the strengthening of the zonal wind stress in the WEP from the 6K simulation is accompanying by attenuation of the El Niño amplitude while the El Niño variability increases in the 0K under the weak Niño4 mean zonal wind stress (Fig. 4.2b) [Zheng *et al.*, 2008; Guilyardi *et al.*, 2006]. This conforms with variations in the simulated west-east zonal wind stress and that of the SST which shows that a strengthening of the west-east annual mean zonal wind stress, lowers the corresponding annual mean SST gradient and the resulting ENSO amplitude over both epochs (Fig. 4.2c). Also, the strong linear correlations ($R^2=0.89$) between the west-east gradients of the wind-SST and wind-thermocline depth pairs (not shown) are similar, however their correlation coefficients are negative and positive respectively. This might explain the importance of the interplay between the local wind stress, the SST and the thermocline depth in controlling the characteristics of the ENSO variability.

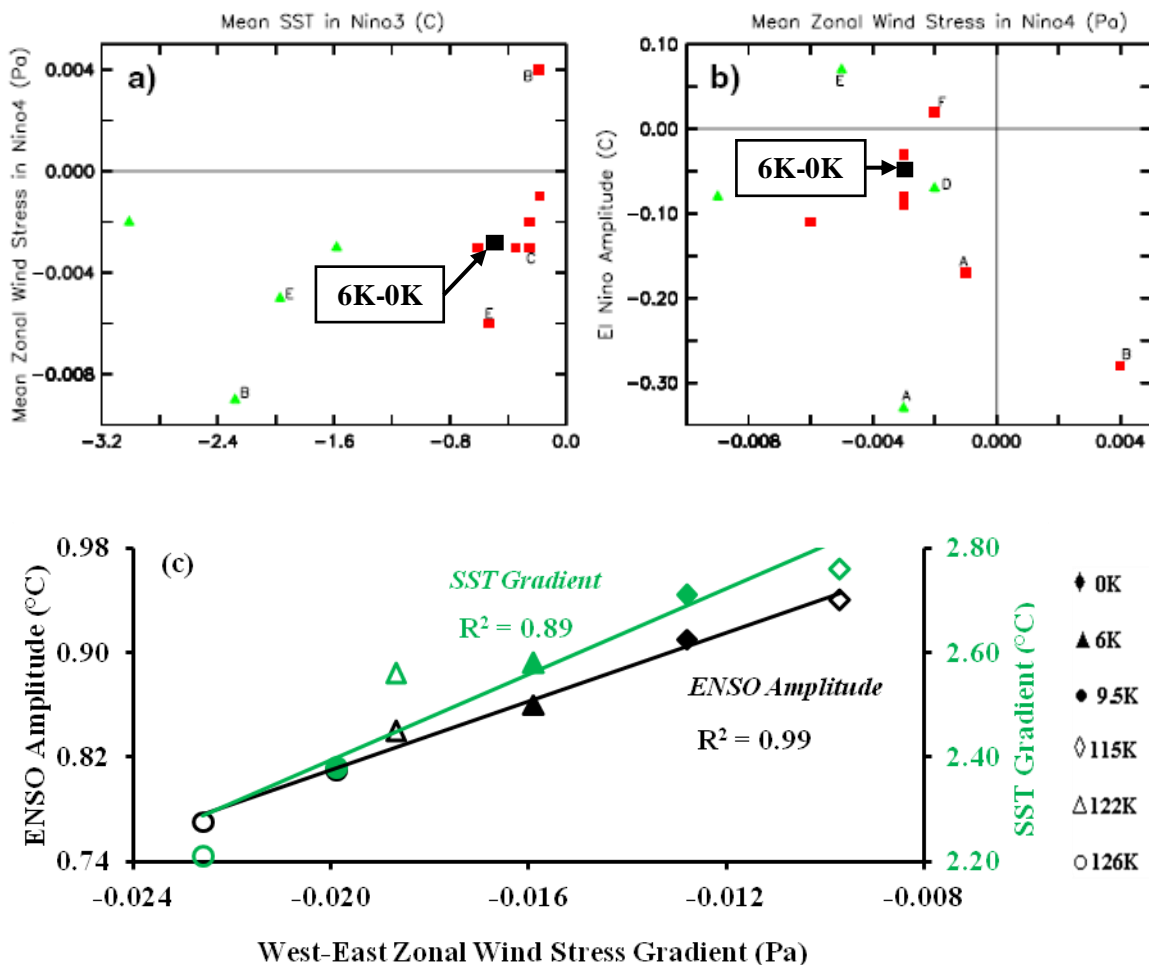


Figure 4.2: The scatter plots of changes in the middle Holocene (red squares) or Last Glacial Maximum, LGM (green triangles) with respect to the control simulation for (a) mean Niño4 zonal wind stress as a function of mean SST, (b) the El Niño amplitude as a function of the Niño4 zonal wind stress (adapted from Zheng et al., 2008, Figure 8a, b). (c) ENSO amplitude (black colours), SST gradient (green colours) as a function of the zonal wind stress gradient. The black squares (in a, b) are the changes in the KCM (6K-0K). Others are CCSM3 (A), FGOALS-1.0g (B), FOAM (C), IPSL-CM4 (D), MIROC3.2 (E), MRI-CGCM2.34fa (F) and MRI-CGCM2.34nfa (G). Note that the strength of the zonal wind stress increases as it becomes more negative.

Furthermore, the model study of Liu and Huang [2000] linked the SST warming trend in the Tropical Pacific to weakening of the trade winds and the accompanying reduction in the vertical and zonal advection of cold water in the eastern and western Pacific respectively. The enhanced amplitude of the cooling is further attributed to increased impact of heat fluxes on the mean state [Zheng et al., 2008] as suggested in this study where the eastern Pacific cools under weak vertical ocean dynamical heating (section 3.1.5). In their model result, Xie et al. [2010] attributed an increase (decrease) in the precipitation over the Tropical Pacific to enhancement (reduction) in SST, which is in accordance with the spatial coverage and the annual mean precipitation simulated by the KCM. An increasing annual mean SST over the Tropical Atlantic and low mean SST in the northern Atlantic lead to cooling within the eastern Pacific in the simulated (KCM) climates (not shown). This is in agreement with the cooling

of the eastern Tropical Pacific induced by high (low) mean SST over the Tropical (northern) Atlantic as reported by *Kucharski et al.* [2011] and on the seasonal time scale by *Xie et al.* [2007]. Also, *Gastineau et al.* [2009] has linked the strengthening of Walker cells to asymmetric warming between the Pacific and Atlantic Oceans.

Held and Soden [2006] argue by investigating an ensemble of greenhouse warming integrations that positive radiative forcing drives an intensification of the hydrological cycle which eventually slows the atmospheric circulation. This especially will lead to weakening of the WC [*Vecchi et al.*, 2006] while stronger SST warming along the Equatorial Pacific and the rapid surface warming compared with deep Ocean has also been suggested as possible mechanism for slowing of the WC [*Liu et al.*, 2005; *Gastineau et al.*, 2009]. The resulting slow WC lowers heat transport away from the equator [*Vecchi and Soden*, 2006; *DiNezio et al.*, 2009]. The dominance of vertical advection with input from anomalous upwelling in the east and the main control of central-western Pacific by zonal advection have also been suggested as responsible for the SST changes over the Tropical Pacific by *Zebiak and Cane* [1987]. In addition, *Xie et al.* [2010] indicates that the strength of the zonal SST under global warming depends on the overall magnitudes of the damping by upwelling in the eastern Pacific [see also *Cane et al.*, 1997], the associated thermocline feedback, evaporative damping and the zonal advection over the equator.

In agreement with *Liu et al.* [2000], the development of ENSO is hindered during a boreal summer warming as the ITCZ shifts northward, leading to cooling of the eastern Pacific under the strong Asian monsoon induced by increased easterly trades and intense WC [*Zebiak and Cane*, 1987; *Webster and Yang*, 1992]. The enhancement of west-east Equatorial SST gradient results in a La Niña-like mean state over the Tropical Pacific in a warm boreal summer as reported by *Clement et al.* [1999; see also *Liu et al.*, 2003; *Liu et al.*, 1998; *Liu et al.*, 2000 and the references therein]. Since the weak coriolis force near the equator strengthens with distance away from the equator, the formation of Tropical cyclones around the ITCZ is also hindered or reduced when it is close to the Equator [*Sellers et al.*, 1998], suggesting that the cyclone occurrence will decrease over time in both epochs. This also indicates that there is no occurrence of Tropical cyclone and the associated damages in the South Atlantic (where the ITCZ never goes far south) or in the southeastern Pacific (where the ITCZ remains north of the equator) all year round. However, recent model studies suggest that the marine ITCZ is also affected by high latitude processes like changes in thermohaline circulation [*Zhang and Delworth*, 2005] and ice cover [*Chiang and Bitz*, 2005] which could be influenced by future climate change [*Overpeck et al.*, 2005]. As shown in the KCM, *Codron et al.* [2001] simulated an orbitally-induced increase in the sensitivity of the central-western Pacific Equatorial wind stress to the eastern Pacific SSTA in a warm climate, which leads to the intensification of the positive SST feedback in the central-western Pacific compared to the east.

The KCM results are consistent with the findings from CO₂-induced global warming scenarios analyzed by *Meehl et al.* [2001] and *Collins et al.* [2010], which linked rising ENSO amplitude to an intensification of west-east SST gradient. Also, some robust relationships between ENSO and the mean Tropical Pacific climate state derived from the current generation of climate models showed a significant trend toward intensification of the ENSO amplitude in a CO₂-forced warmer climate [*Guilyardi* 2006; *Park et al.*, 2009]. Unlike the orbitally-induced changes in the ENSO characteristics that are associated with surface processes in this study, *Park et al.*, [2009] linked the rising ENSO variability to intensification of the equatorial thermocline [see also *Timmermann et al.*, 1999] feedback and strong atmospheric sensitivity to the SST. Also, the overall La Niña-like mean state over the Tropical Pacific in the KCM simulation is not consistent with the El Niño-like mean state obtained in some global climate models where the temperature rises with increasing concentrations of greenhouse gases [*Knutson and Manabe*, 1995; *Meehl and Washington*, 1996; *Timmerman et al.*, 1999]. Similarly, *Wang* [2007] found no significant change in the ENSO amplitude and period of variability despite a shift towards high temperature reported in their greenhouse warming simulation. However, it should be noted that the CO₂ warming scenario can differ from orbital forcing dramatically, since the former is a globally uniform forcing all year round while the latter varies with latitude and is more confined to the seasonal cycle signal. The KCM simulation shows that El Niño-like climate change might not be appropriate for describing the mean Tropical Pacific climate change on interannual timescales as earlier suggested by *Collins et al.* [2010]. Since the relationship between the ENSO amplitude and the mean Tropical Pacific SSTs agrees well with previous findings, this study suggests that especially the SST of the western Equatorial Pacific is the key factor controlling the simulated changes in the ENSO amplitude.

To assess the influence of other forcing on the mean climate and the impact of WPWP on the ENSO variability, the KCM simulations with enhanced CO₂ concentration (400ppm) and a past climate that mimics the opening of the Indonesian throughflow, ITF (≈ 3 million years ago) [details in *Krebs et al.*, 2011] are considered (Figs. 4.3a, b). The orbital parameters are set to the modern values in both cases. The investigation yields a warmer climate (27.06°C) in the CO₂ simulation compared to the ITF (24.36°C) while the respective ENSO amplitude (west-east SST gradient) are 0.98°C (2.77°C) and 0.85°C (2.51°C). The above result suggests that the linear relationships between the ENSO amplitude and the annual mean SST over the warm pool and with the west-east SST contrast might be valid in the past climate and consistent with a future warming climate induced by rising greenhouse gases (Figs. 4.3a, b). In accordance with the KCM result, enhancement of ENSO variability with rising SST has also been presented from several models and data results reported for the past millennium by IPCC [*Jansen et al.*, 2007, see also *Cane*, 2005].

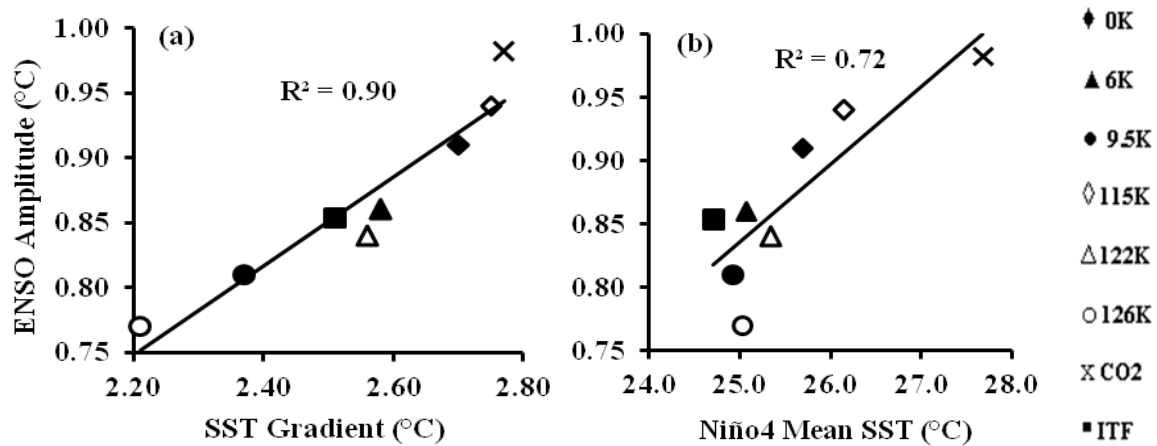


Figure 4.3: The relationships between the ENSO amplitude (°C) (y-axis) and (a) the annual mean west-east SST gradient and (b) annual mean Niño4 SST with the inclusion of the CO₂ and the ITF simulations which are represented by the cross and the filled square symbols respectively.

4.3 Summary

The comparison shows that the simulated ENSO amplitude (0K) is in good agreement with observations and with other model studies. The KCM results further confirmed that an enhancement of the ENSO strength is associated with increasing annual mean SST, weakening of the trade winds and reduction of the west-east Z20 gradient over the Tropical Pacific. The comparison favours a La Niña-like mean state in a warm boreal summer over the Holocene and Eemian periods. The linear relationship between the ENSO amplitude and the annual mean west-east SST gradient is in agreement with previous studies while the strong correlation between the ENSO amplitude and the Niño4 SST indicates that the WPWP region is suitable for reconstructing past ENSO strength. However, this assertion needs further confirmation by paleo-climatologists due to lack of suitable data from the ENSO regions (especially from the Niño4 box) for comparison at the time of this study.

“Climate change poses clear, catastrophic threats. We may not agree on the extent, but we certainly can't afford the risk of inaction.” - Rupert Murdoch

CHAPTER FIVE

Discussion

This study is designed to investigate the sensitivity of El Niño/Southern Oscillation (ENSO) to changes in the mean climate state of the Tropical Pacific. The attention is focused on the variations induced by changes in the orbital parameters, resembling the past interglacial periods of the Holocene and the Eemian that might be analogous to a future global warming condition. The discussion of the results is presented in this chapter by providing answers to the previously listed research objectives and questions in Chapter One.

5.1 Discussion of the Main Findings

5.1.1 *The link between ENSO variability and the Tropical Pacific Mean State*

This investigation with KCM reveals a linear relationship between ENSO amplitude and the annual mean SST over the Tropical Pacific, suggesting that the ENSO variability will intensify as the Sea surface temperature increases over the Tropical Pacific. The intensification of the ENSO amplitude with rising annual mean SST (in the orbitally-forced KCM experiments with seasonal signal of SST) agrees with high CO₂ global warming scenarios that show a significant trend toward increasing ENSO amplitude among models that best reproduced the observed ENSO characteristics [Guilyardi, 2006]. However, the largest changes in the ENSO amplitude occurred in models which exhibit a mode change towards a thermocline mode while the present study linked the ENSO changes to the surface layer processes. The high positive correlation between the ENSO amplitude and the warm pool SST indicates that the WPWP SST is a suitable indicator to monitor ENSO variability, probably during the past. The western Pacific SST together with the strong linear response of the ENSO amplitude to the west-east SST contrast might serve as an important index for the climate scientists in quick assessment of the strength of ENSO amplitude.

Based on the KCM results, this study implies that changes in ENSO strength are sensitive to fluctuations in the mean state of the Tropical Pacific and that the characteristics will vary in a future changing climate. This is a robust finding considering the linear changes in the response of the ENSO amplitude to the warming trends over the Holocene and the Eemian climates. The robust link to the mean climate state in the Tropical Pacific is a powerful tool to be applied to paleo reconstructions that only allow resolution of the mean state, but which do not resolve higher frequency internal climate variability. It may also be used in future climate projections that are usually assumed to be more reliably predicting the mean state than the internal variability.

5.1.2 *The Response of ENSO to changes in the mean state in other Model Experiments*

The intensification of the simulated ENSO amplitude with increasing SST over the Tropical Pacific is an important finding among similar experiments since the changes are purely induced by variations in the orbital forcing which have been identified as the main driver of climate variability during the Holocene [Lorenz *et al.*, 2006; Braconnot *et al.*, 2008; Berger, 1988; Mayewski *et al.*, 2004], and were also important factors driving climate change during the Eemian [Montoya *et al.*, 2000; Kutzbach *et al.*, 1991; Crowley and Kim, 1994]. The linear relationship between the ENSO amplitude and the annual mean SST in the KCM is preferable to the similar result in the orbitally-forced Holocene climate reported by Clement *et al.* [1999] where the ability of their model to fully simulate paleoclimate change is weakened by the restriction of the active region to the Tropical Pacific (124°E:80°W, 29°N:29°S). Similarly, model studies by Timmermann *et al.* [2007] also linked the changes in ENSO statistics to variations in the seasonal distribution of solar radiation through fluctuations in the precessional cycle. However, they partly used flux corrections which might reduce the efficiency of their model to simulate the important atmosphere-ocean feedbacks over the Tropical Pacific [Spencer *et al.*, 2007; Brown *et al.*, 2008], a problem which has been cared for in the KCM by the exclusion of the flux correction.

The KCM results are similar to the findings from intermediate ENSO model [Zebiak and Cane, 1987] presented by Clement *et al.* [1999] where the ENSO is most sensitive to precessional forcing rather than to the obliquity forcing which only dominates the mean climate change in the Tropical Pacific [Timmermann *et al.*, 2007]. Unlike the variations in the ENSO characteristics induced by fluctuations in the mean Tropical Pacific climate in the KCM, Clement *et al.* [1999] suggested that the modifications of the ENSO behaviour is responsible for changes in the mean Tropical Pacific climate. The discrepancy with Clement *et al.* [1999] might be explained by the fact that the insolation forcing is applied to the mixed layer [see also Timmermann *et al.*, 2007] while changes in the KCM are associated with top of atmosphere insolation forcing. Several studies also show that the response of the ENSO to global warming is model dependent, even in the extreme scenarios (4xCO₂) [Guilyardi *et al.*, 2009]. While the ENSO amplitude is decreasing in some model simulations, the amplitude rises in another set and remains unchanged in the others [Latif and Keenlyside, 2009; Collins *et al.*, 2010; Cane, 2005]. These inconsistencies have been attributed to causes like strong mean zonal Equatorial Pacific wind stress that limits the development of interannual anomalies while the associated seasonal cycle has been shown to be negatively correlated with the ENSO amplitude [Guilyardi, 2009].

In addressing some of the problems, Latif and Keenlyside, [2009] proposed that carefully perturbed ensemble integrations are needed in some models for better detection of ENSO statistics (like the amplitude and frequency). Model improvement with better parameterization to simulate the impacts of changes in systems including carbon cycle, biological and chemical processes has been recommended [Latif and Keenlyside, 2009]. In addition, enhanced model resolution is necessary for

capturing details of the ENSO statistics like the amplitude, frequency and the correct phase locking of the ENSO to the annual SST cycle. For instance, it has been noted that global coupled models with relatively coarse grid resolution failed to simulate all the dynamical coupled processes that are related to the observed ENSO events [Neelin *et al.*, 1992]. The current improved models with enhanced latitudinal resolution in the Equatorial Tropics have shown increased SST variability in the EEP and performed better compared to the models with coarse resolution in simulating ENSO characteristics [Meehl *et al.*, 2001, and the references therein]. As the first time of performing these series of experiments with a high resolution model over the Holocene and Eemian, this findings with KCM might help the scientific community as a guide in predicting the response of ENSO to an enhancement of SST over the Tropical Pacific since the incidences of extreme changes increase in a warmer climate in the KCM simulations.

5.1.3 The Changes in the Frequency of the ENSO Variability

Based on the KCM result, the frequency of ENSO variability will remain largely unchanged under an intensification of SST over the Tropical Pacific mean state. Several coupled GCMs have produced different time scales of ENSO variability with spectra range that include the biennial oscillation to the observed 2-7 years [Guilyardi, 2009]. However, the result presented in this study should be preferred to the similar frequency of 3-4 years obtained by Meehl *et al.* [2006] where the integrations are much shorter compared to the KCM simulation despite the avoidance of flux adjustment. The frequency of 2–4 years from the Holocene model study by Otto-Bliesner *et al.* [2003] is less plausible when compared to the present study which spanned over both the Holocene and the Eemian climates. A search into literature shows a frequency range of 2–8 years in the Holocene paleo data studied by Moy *et al.* [2002], however their method failed to capture all El Niño events which should have narrowed the frequency band.

In their future scenario forced by increasing greenhouse gas concentrations, Timmermann *et al.* [1999] found a 2 years ENSO period with preference for El Niño-like event and weaker strength compared to La Niña-like condition. This is in contrast to the La Niña-like mean state favoured by the KCM where the major changes are linked to surface processes while the main fluctuations in the analysis reported by Timmermann *et al.* [1999] are linked to strengthening of the equatorial thermocline. These discrepancies might be associated with the use of earlier version of ECHAM5 (the ECHAM4) which is coupled to a different (isopycnal) ocean model [Park *et al.*, 2009] while the use of flux correction in their study could also affect the atmosphere-ocean feedbacks over the Tropical Pacific [Spencer *et al.*, 2007; Brown *et al.*, 2008].

5.1.4 The ENSO Variability and Changes in the ITCZ Position

The present study indicates that a change in the mean position of the ITCZ has a potential impact on ENSO characteristics and could also affect the future development of ENSO event and the overall weather. For instance, the southward migration of the mean position of the ITCZ raises the instability over the Tropical Pacific with the intensification of the westerly anomalies which strengthens the ENSO amplitude and shifts the region of strong downpour eastward. This could affect the social life, agriculture, the ecosystem and the overall economy in the western Pacific where the amount of rainfall is low while eastward shift of regions of heavy rainfall might lead to flooding in the eastern Pacific with damages to infrastructures and have impact on the economy. In addition, the suppression of Tropical cyclones near the equator where the coriolis force is weak [Sellers *et al.*, 1998] indicates a reduction in the occurrence of cyclones over time during the Holocene and Eemian as the ITCZ shifts southward while more cyclones form as the coriolis force strengthened away from the Equator. The future implication is that, an increase in the La Niña-like mean state over the Tropical Pacific and the associated northward shift of the ITCZ position will raise the frequency of damaging Tropical cyclones in the Tropical Atlantic while the destructions will be less in the EEP and central Tropical Pacific [Pielke and Landsea, 1999]. The clear understanding of the direction of changes in the ENSO cycle and the ITCZ position as presented in the KCM result could help in improving weather forecast and assist the policy makers in their search for mitigations against the hazards associated with ENSO events. Such mitigations might be in the form of improvement in the infrastructures, warning systems or readiness to manage the unavoidable crises accompanying the extreme ENSO events.

5.1.5 The ENSO Amplitude and the Annual SST Cycle

The present study with KCM shows a combined increase in the magnitudes of both SST seasonal cycle and the ENSO amplitude as the Tropical Pacific warms. This contradicts the inverse relationship reported in many model studies [Fedorov and Philander 2001; Guilyardi 2006] and in the simulations described by Timmermann *et al.* [2007] and Liu [2002] where the ENSO amplitude intensifies as the seasonal cycle of SST weakens due to frequency entrainment. An accurate simulation of the annual cycle in the Tropical Pacific is important due to the tight coupling between the ENSO and the seasonal cycle. However, many models failed to reasonably simulate the annual cycle over the Tropical Pacific [Mehoso *et al.*, 1995; Latif *et al.*, 2001], with a possible erroneous estimation of the characteristics of the mean state [Jin *et al.*, 1994; Chang *et al.*, 1994; Li and Hogan, 1999]. Instead, overly strong seasonal cycles of the SST and wind stress with sometimes spurious semiannual cycles have been simulated in the eastern Pacific by several models [Guilyardi, 2006], contradicting the observed annual SST cycle [Meehl *et al.*, 2001]. One mechanism to explain the characteristics of the simulated seasonal cycle is the strong westward extension of the cold tongue and the possible reduction in the

latitudinal asymmetry which might wrongly lead to a semiannual cycle over the cold tongue in the east [Xie *et al.*, 2007]. However, there is no concrete evidence at present to show that model climatology biases could lead to biases in the simulated ENSO changes [Latif *et al.*, 1993; Luo *et al.*, 2005].

5.2 The Setbacks and Model Biases

The KCM shows good agreement with observation and models in terms of the simulated ENSO amplitude (see Chapter 4). However, the lack of sufficient data and model studies constitutes a major problem. For instance, several data for ENSO reconstructions have either insufficient lengths [Cane, 2005], or have poor resolution [Moy *et al.*, 2002] with lack of continuity [Jansen *et al.*, 2007] or are not available within the ENSO regions of the Tropical Pacific. The discontinuities in paleo-data make a precise characterization of the rate and timing of the transition to the modern climate a difficult task [Jansen *et al.*, 2007]. Also, efforts to get high resolution Holocene and Eemian paleo reconstruction data of the warm pool SST for comparison were not successful while modern observations are limited to the recent centuries. In addition, model studies and high resolution paleo reconstructions of the Eemian climate were very scarce and almost not available for comparison at the time of this study. However, despite the good agreements between the KCM and observations, there are still some errors in the KCM results like a cold biased annual mean state with westward extension of the cold tongue across the Equatorial Pacific while the peak (least) seasonal phase locking occurred outside the observed boreal winter (spring) season. In spite of these deficiencies, the performance of KCM in simulating the ENSO frequency [Meehl *et al.*, 2006; Zebiak and Cane, 1987] and the ENSO amplitude is reasonable (Chapter 4) when compared to other non-flux corrected climate models [Guilyardi *et al.*, 2006; 2009; Neelin *et al.*, 1992; Latif *et al.*, 2001].

5.3 Summary and Conclusion

This study described the performance of the newly developed Kiel Climate Model (KCM) in simulating the response of ENSO to changes in the mean state of the Tropical Pacific over the Holocene and Eemian climates. Though there are many factors involved in the real World [Rensen *et al.*, 2009] which include changes in the greenhouse gas concentrations, sea level and ice sheets, however, this study gave priority to the orbital forcing which is an important driver of climate variability in the Holocene and the Eemian climates. The model reveals useful information about the ENSO variability over the Tropical Pacific.

- The result suggests that the absolute temperature in the Equatorial Pacific is the key parameter controlling the ENSO amplitude in the KCM. The simulated ENSO amplitude increases linearly with SSTs in the Tropical Pacific and with an increased west-east Equatorial SST gradient. The changes in the surface warming (SST) are negatively correlated with the

obliquity forcing while the resulting ENSO amplitude is best explained by the precessional forcing.

- The higher damping of the SST changes in the Eastern Pacific compared to the Western Pacific is largely induced by fluctuations in the vertical ocean dynamical heating with contribution from the zonal heat transport.
- The ENSO amplitude correlates positively with the seasonal SST amplitude in the EEP and negatively with the strength of the easterly Trades over the Equatorial Pacific.
- At the same time, the ENSO frequencies remain rather constant within a broad range peaking at periods of 3-4 years, which is close to modern observations.
- A weak correlation between the ENSO amplitude and the annual mean upper ocean heat content over the Tropical Pacific indicates that the origin of the simulated ENSO changes is primarily from the surface layer processes.
- A northward shift in the mean position of the ITCZ has the potential to lower the ENSO amplitude while the amplitude strengthens as the ITCZ migrates southward. The magnitude of the west-east Z20 gradient lowers due to weakening of the associated trade winds over the Tropical Pacific during a southward shifts of the ITCZ and vice versa.
- The weakening (strengthening) of the trade winds in the western (eastern) Pacific under rising Walker circulation supports the enhancement of the west-east SST gradient and an overall La Niña-like mean state in a warm boreal summer.
- The strong correlation between the ENSO amplitude and the Niño4 SST ($r=0.89$) indicates that the warming in the WPWP is the key factor controlling the changes in the ENSO amplitude, thus suggesting that the WPWP region is a suitable area to reconstruct ENSO strength during the past.

These results with KCM provide important insights into the mechanisms that are controlling ENSO variability and they are in good agreement with paleo reconstructions and other climate model simulations for the Holocene. Hence, the mechanisms described in this thesis might serve as a guide for understanding the link between the changes in the annual mean state of the Tropical Pacific and ENSO variability.

5.4 Possible Future Research

The KCM shows a linear relationship between the ENSO amplitude and the annual mean SST over the Tropical Pacific mean climate during the Holocene and Eemian. However, more work is still needed since most results remain divergent. The accuracy of the simulated mean climate is still hindered by model imperfections ranging from forcing errors to poor estimation of the contributions of the individual signal associated with the natural variability. For instance, it is expected that the decrease in boreal summer insolation in the last few millennia should favour ice buildup [*Jansen et al., 2007*;

Hoyle, 1981], the fact that this is not the case points to the existence of gaps in our understandings of the inconsistencies in the climate variability. As part of the solution, long-term integration of the KCM could also be carried out with higher model resolution to quantify the effects of resolution on the simulated mean climates (Holocene, Eemian) and on the ENSO variability. However, *Tzedakis et al. [2012]* shows that the absence of a new ice growth with the current insolation forcing indicates that the orbital scale variability might not be controlling the impacts of the global warming of anthropogenic origins. Instead models show that the current orbital configuration with a low boreal insolation might only lead to a new glacial inception provided the current level of CO₂ concentration of 390 ppm [*Archer and Ganopolski, 2005*] reduces below the preindustrial value of about 280 ppm [*Loure and Berger, 2000; Vettoretti and Peltier, 2004; Cochelin et al., 2006, see Tzedakis et al., 2012*].

While the important features of the ENSO are well simulated by the KCM, it is also necessary to consider other processes so as to explain the non-linear response of the surface temperature to the seasonal signal of the orbitally-induced insolation [see *Lorenz et al., 2006*]. Hence, the inclusion of other forcing mechanisms (like greenhouse gas forcing, changes in sea level, ice sheet extent, dynamic vegetation, volcanic forcing) to the orbital parameters might help to explain the imbalance in our understanding of the magnitude of the observed climatic changes and the present-day warming. For instance, *Otto-Bliesner et al. [2006]* indicates that a test of the impact of the continental ice sheets might shed more lights on the evolution of Eemian climate. In addition, further simulations might be needed to isolate the orbital parameters and test the response of the ENSO amplitude to the changes in the mean Tropical Pacific climate induced by variations in the individual orbital forcing. This is necessary since the present groups of models may not be perfectly representing the complex interactions between the processes required for simulating the response of ENSO to changes in the mean climate [*Brown et al., 2008*]. Furthermore, the assessment of future climate change also requires the simulation of the next centuries to cover the entire Holocene climate and periods that are analogous to that with enhanced anthropogenic greenhouse gas. This will help climate scientists in distinguishing the influence induced by the variability under natural sources from that of the anthropogenic.

In addition, the strong positive correlation between the ENSO amplitude and the WPWP SST is a robust finding in this study which needs further confirmation using high resolution paleo data from the ENSO regions (Niño4 and Niño3). More comparisons of model results with paleo reconstructions will help in verifying model's accuracy and improve our understanding of the climate variability and its predictability. Also, the ongoing efforts to improve model simulations through enhanced physical parameterization of the unresolved processes, observational records and theoretical understanding of ENSO could add to the progress made in producing reliable projection models which agree well with observations [*Collins et al., 2010*]. For instance, further work could be done on the findings by *Luo et al., [2005]* which suggests that a reduction in the easterly wind stress by transferring the ocean surface

Discussion

current momentum to the atmosphere will improve the warm pool/cold tongue structure with less westward extension of cold tongue over the Tropical Pacific.



“There is still time to avoid the worst impacts of climate change, if we take strong action now.”

- Sir Nicholas Stern

References

- Adler, R. F., G. J. Huffman, A. Chang, R. Ferraro, P. Xie, J. Janowiak, B. Rudolf, U. Schneider, S. Curtis, D. Bolvin, A. Gruber, J. Susskind, and P. Arkin (2003), The Version 2 Global Precipitation Climatology Project (GPCP) Monthly Precipitation Analysis (1979-Present), *J. Hydrometeorol.*, 4, 1147-1167.
- Andersen, C., N. Koç, A. Jennings, and J. T. Andrews (2004), Non uniform response of the major surface currents in the Nordic Seas to insolation forcing: implications for the Holocene climate variability, *Paleoceanography*, 19, 1–16.
- Archer, D., and A. Ganopolski (2005), A movable trigger: Fossil fuel CO₂ and the onset of the next glaciations, *Geochem. Geophys. Geosyst.* 6, Q05003.
- Battisti, D. S. and A. C. Hirst (1989), Interannual Variability in the Tropical Atmosphere-Ocean System: Influences of the Basic State, Ocean Geometry and Nonlinearity, *J. Atmos. Sci.*, 46, 1687-1712.
- Berger, A. L. (1978), Long-term variations of daily insolation and Quaternary climatic Changes, *J. Atmos. Sci.*, 35, 2363-2367.
- Berger, A. L. (1988), Milankovitch Theory and Climate, *Rev. Geophys.*, 26, 624–657.
- Bigelow, N. H, L. B. Brubaker, M. E. Edwards, S. P. Harrison, I. C. Prentice, P. M. Anderson, A. A. Andreev, P. J. Bartlein, T. R. Christensen, W. Cramer, J. O. Kaplan, A. V. Lozhkin, N. V. Matveyeva, D. F. Murray, A. D. McGuire, V. Y. Razzhivin, J. C. Ritchie, B. Smith, D. A. Walker, K. Gajewski, V. Wolf, B. H. Holmqvist, Y. Igarashi, K. Kremenetskii, A. Paus, M. F. J. Pisaric, and V. S. Volkova (2003), Climate change and Arctic ecosystems: 1. Vegetation changes north of 55°N between the last glacial maximum, mid-Holocene, and present. *J. Geophys. Res.*, 108, doi:10.1029/2002JD002558.
- Bjerknes, J. (1969), Atmospheric teleconnections from the equatorial Pacific, *Mon. Wea. Rev.*, 97, pp. 163–172.
- Blanke, B., J. D. Neelin, and D. Gutzler (1997), Estimating the effect of stochastic wind stress forcing on ENSO irregularity, *J. Clim.*, 10, 1473–1486.
- Braconnot, P., S. Harrison, J. Joussaume, C. Hewitt, A. Kitoh, J. Kutzbach, Z. Liu, B. L. Otto-Bleisner, J. Syktus, and S. L. Weber (2004), Evaluation of Coupled Ocean-Atmosphere Simulations of the Mid-Holocene, in: Past Climate Variability through Europe and Africa, edited by: R. W. Bartabee, F. Gasse and C. E. Stieckley, Kluwer Academic publisher, 515-533.
- Braconnot, P., C. Marzin, L. Grégoire, E. Mosquet, and O. Marti (2008), Monsoon response to changes in Earth's orbital parameters: comparisons between simulations of the Eemian and of the Holocene, *Clim. Past*, 4, 281–294.

References

- Braconnot, P., Otto-Bliesner, B., Harrison, S., Joussaume, S., Peterchmitt, J. Y., Abe-Ouchi, A., Crucifix, M., Driesschaert, E., Fichet, T., Hewitt, C. D., Kageyama, M., Kitoh, A., Loutre, M. F., Marti, O., Merkel, U., Ramstein, G., Valdes, P., Weber, L., Yu, Y., and Zhao, Y. (2007): Results of Pmip2 Coupled Simulations of the Mid-Holocene and Last Glacial Maximum – Part 2: Feedbacks with Emphasis on the Location of the ITCZ and Mid- and High Latitudes Heat Budget, *Clim. Past*, 3, 279–296, 2007b, <http://www.clim-past.net/3/279/2007/>.
- Brown, J., M. Collins, and A. Tudhope (2006), Coupled model simulations of mid-Holocene ENSO and comparisons with coral proxy records, *Adv. Geosciences*, 6, 29–33.
- Brown, J., M. Collins, A. W. Tudhope, and T. Toniazzo (2008), Modelling mid-Holocene tropical climate and ENSO variability: towards constraining predictions of future change with palaeo-data, *Clim Dyn* (2008) 30:19–36.
- Buchdahl Joe (1999), Global Climate Change, A review of contemporary and prehistoric global climate change, Atmosphere, Climate and Environment Information Programme (aric), Manchester (http://www.ace.mmu.ac.uk/resources/gcc/Climate_Change_Study_Guide.pdf).
- Buckland, P. C., T. Amorosi, L. K. Barlow, A. J. Dugmore, P. A. Mayewski, T. H. McGovern, A. E. J. Ogilvie, J. P. Sadler, and P. Skidmore (1995), Bioarchaeological evidence and climatological evidence for the fate of Norse farmers in medieval Greenland. *Antiquity* 70, 88–96.
- Cane, M. A. (2005), The Evolution of El Niño, past and future, *Earth and Planetary Science Letters*, Vol 230, 227-240.
- Cane, M. A., and S. E. Zebiak (1987), Prediction of El Niño events using a physical model. *Atmosphere and Ocean Variability*, H. Cattel, Ed, *Roy. Meteor. Soc.*, 153-182.
- Cane M. A, A. C. Clement, A. Kaplan, Y. Kushnir, D. Pozdnyakov, R. Seager, S. E. Zebiak, and R. Murtugudde (1997), Twentieth-century sea surface temperature trends *Science*, 275:957–960.
- Chiang, J. C. H., and C. M. Bitz (2005), Influence of high latitude ice cover on the marine Intertropical Convergence Zone, *Clim Dyn*, v. 25, p. 477–496, doi: 10.1007/s00382-005-0040-5.
- Chang, P., B. Wang, T. Li, and L. Ji (1994), Interactions between the seasonal cycle and the Southern Oscillation-frequency entrainment and chaos in a coupled ocean–atmosphere model. *Geophys. Res. Lett.*, 21, 817–820.
- Chavez F. P., P. G. Strutton, G. E. Friederich, R. A. Feely, G. C. Feldman, D. G. Foley, and M. J. McPhaden (1999), Biological and Chemical Response of the Equatorial Pacific Ocean to the 1997-98 El Niño, *Science*, 286, 2126-2131.
- Clement, A. C., R. Seager, and M. A. Cane (1999), Orbital controls on ENSO and tropical Climate, *Paleoceanography*, 14, 441-456.
- Clement, A. C., R. Seager, and M. A. Cane (2000), Suppression of El Niño during the mid-Holocene by changes in the Earth’s orbit, *Paleoceanography*, 15, 731–737.

-
- Codron, F., A. Vintzileos, and R. Sadourny (2001), Influence of Mean State Changes on the Structure of ENSO in a Tropical Coupled GCM, *J. Clim.*, 14, 730–742.
- Cochelin, A.-S., L. A. Mysak and Z. Wang (2006), Simulation of long-term future climate changes with the green McGill paleoclimate model: The next glacial inception, *Climatic Change* 79, 381-401.
- Cole, J. (2001), A slow dance for El Niño, *Science*, 291, 1496–1497.
- Collins, M., S.-I. An, W. Cai, A. Ganachaud, E. Guilyardi, F.-F. Jin, M. Jochum, M. Lengaigne, S. Power, A. Timmermann, G. Vecchi, and A. Wittenberg (2010), The impact of global warming on the tropical Pacific Ocean and El Niño, *Nature Geosciences*, 3, 391-397.
- Collins, M. (2000a), Understanding uncertainties in the response of ENSO to greenhouse warming, *Geophys. Res. Lett.*, 27, 3509–3512.
- Collins, M. (2000b), The El Niño Southern Oscillation in the second Hadley Centre coupled model and its response to greenhouse warming, *J. Clim.*, 13, 1299-1312.
- Conkright, M. E., R. A. Locarnini, H. E. Garcia, T. D. O'Brien, T. P. Boyer, C. Stephens, and J. I. Antonov (2002), World ocean atlas 2001: Objective analyses, data statistics, and figures, *CD-ROM documentation*, NOAA, Silver Spring.
- Conroy J. L., J. T. Overpeck, J. E. Cole, T. M. Shanahan, and M. Steinitz-Kannan (2008), Holocene changes in eastern tropical Pacific climate inferred from a Galápagos lake sediment record, *Quaternary Science Reviews* 27 (2008) 1166– 1180.
- Crowley, T. J. and North, G. R. (1991), *Palaeoclimatology*. Oxford Monographs on Geology and Geophysics No. 18. Oxford University Press, New York, 339pp. Harlow, England. 439pp.
- Crowley, T. J. and K.-Y. Kim (1994), Milankovitch forcing of the last interglacial sea level. *Science*, 265, 1566–1568.
- Cuffey, Kurt M.; Marshall, Shawn J. (2000). "Substantial contribution to sea-level rise during the last interglacial from the Greenland ice sheet", *Nature* 404: 591–594. doi:10.1038/35007053.
- Davis, B. and S. Brewer (2009), Orbital forcing and role of the latitudinal insolation/ temperature gradient. *Climate Dynamics*, 32 (2), 143–165.
- Davis, Mike (2001), *Late Victorian Holocausts: El Niño Famines and the Making of the Third World*, London: Verso. pp. 271. ISBN 1859847390.
- Deser, C., A. Capotondi, R. Saravanan, and A. S. Phillips (2006), Tropical Pacific and Atlantic climate variability in CCSM3. *J. Climate*, 19(11), 2451-2481.
- DeWitt, D. G. and E. K. Schneider (2000), The tropical ocean response to a change in solar forcing. *J. Climate*, 13, 1133-1149.
- Dommenget, D. (2010), The slab ocean El Niño, *Geophys. Res. Lett.*, 37, L20701, doi:10.1029/2010GL044888.
-

References

- Dijkstra H. A, and B. Burgers (2002), Fluid Dynamics of El Niño Variability, *Annu. Rev. Fluid Mech.*, 34:531–58.
- Dijkstra H. A., and J. D. Neelin (1995), Ocean–atmosphere interaction and the tropical climatology. Part II: Why the Pacific cold tongue is in the east. *J. Clim.*, 8, 1343–1359.
- DiNezio, P. N., A. C. Clement, G. A. Vecchi, B. J. Soden, B. P. Kirtman, and S.-K. Lee, (2009), Climate Response of the Equatorial Pacific to Global Warming. *J. Clim.*, 22, 4873–4892.
- Eckert, C., and M. Latif (1997), Predictability of a stochastically forced hybrid coupled model of El Niño, *J. Clim.*, 10, 1488–1504.
- Fairbanks, R. G. (1989), A 17,000 year glacioeustatic sea level record: Influence of glacial melting rates on the Younger Dryas event and deep ocean circulation, *Nature*, 342, 637– 642.
- Fedorov, A. V., and S. G. Philander (2000), Is El Niño changing? *Science*, 288, 1997–2002.
- Fedorov, A. V., and Philander, S.G. (2001), A stability analysis of the tropical ocean-atmosphere interactions: Bridging Measurements of, and Theory for El Niño, *J. Clim.*, 14, 3086–3101.
- Fichefet, T., and M. A. Morales Maqueda (1997), Sensitivity of a global sea ice model to the treatment of ice thermodynamics and dynamics, *J. Geophys. Res.*, 102, 12,609–12,646.
- Gagan, M. K., E. J. Hendy, S. G. Haberle, and W. S. Hantoro (2004), Post-glacial evolution of the Indo-Pacific Warm Pool, *Quat. Int.*, 118–119 (2004), pg. 127–143, doi:10.1016/S1040-6182(03)00134-4.
- Gagan, M. K, et al. (1998), Temperature and surface-ocean water balance of the mid-Holocene tropical western Pacific, *Science*, 279, 1014–1018.
- Ganopolski, A., C. Kubatzki, M. Claussen, V. Brovkin, and V. Petoukhov (1998), The influence of vegetation-atmosphere-ocean interaction on climate during the mid -Holocene, *Science*, 280, 1916-1919.
- Gastineau, G., L. Li, and H. Le Treut (2009), The Hadley and Walker circulation changes in global warming conditions described by idealised atmospheric simulations. *J. Clim.* 22, 3993–4013.
- Gill, R. B. (2000), *The Great Maya Droughts: Water, Life, and Death*, University of New Mexico Press, Albuquerque.
- Goodess, C. M., Palutikof, J. P., and Davies, T. D. (1992), *The nature and causes of climate change*. Belhaven Press, London. 248pp.
- Grootes, P. M., M. Stuiver, J. W. C. White, S. J. Johnsen, and J. Jouzel (1993), Comparison of oxygen isotope records from the GISP2 and GRIP Greenland ice cores, *Nature*, 366, 552– 554.
- Grove, R. H. (1998), "Global Impact of the 1789–93 El Niño", *Nature* 393 (6683), 318–319. doi:10.1038/30636.
- Guilyardi, E. (2006), El Niño-mean state-seasonal cycle interactions in a multi-model Ensemble, *Clim. Dyn.*, 26, 329-348, DOI 10.1007/s00382-005-0084-6.

-
- Guilyardi, E., A. Wittenberg, A. Fedorov, M. Collins, C. Wang, A. Capotondi, G. J. van Oldenborgh, and T. Stockdale (2009), Understanding El Niño in Ocean-Atmosphere General Circulation Models : progress and challenges, *Bull. Amer. Met. Soc.*, 90, 325-340.
- Hall, A., and S. Manabe (1999), The Role of water vapor feedback in unperturbed climate variability and global warming. *J. Clim.*, 12, 2327-2346.
- Harrison, S. P., J. E. Kutzbach, Z. Liu, P. J. Bartlein, B. Otto-Bliesner, D. Muhs, I. C. Prentice, and R. S. Thompson (2003), Mid-Holocene climates of the Americas: a dynamical response to changed seasonality, *Clim. Dyn.*, 20, 663-688, doi:10.1007/s00382-002-0300-6.
- Hays, J. D., J. Imbrie, and N. J. Shackleton (1976), Variations in the Earth's orbit: Pacemaker of the ice ages, *Science*, 194, pp. 1121-1132.
- Held, I. M., and B. J. Soden (2006), Robust responses of the hydrological cycle to global warming. *Journ. of Clim.*, 19, 5686-5699.
- Ho, C. R., X. H. Yan, and Q. Zheng (1995), Satellite observations of upper-layer variability in the western Pacific warm pool, *Bulletin of the American Meteorological Society* 76: 669-679.
- Hodell, D. A., Brenner, M., Curtis, J. H., Guilderson, T. (2001), Solar forcing of drought frequency in the Maya Lowlands, *Science*, 292, 1367– 1370.
- Hoyle, F. (1981), *Ice*. Hutchinson, London.
- Hurlburt H. E, J. C. Kindle, and J. J. O'Brien (1976), A numerical simulation of the onset of El Niño, *J. Phys Oceanogr.*, 6, 621-631.
- Imbrie, J., and K. P. Imbrie (1979), *Ice Ages: Solving the Mystery*, Macmillan Press Ltd., London, 224pp.
- IPCC (2007), Summary for Policymakers. In: *Climate Change 2007: The Physical Science Basis. Contribution of Working Group I to the Fourth Assessment Report of the Intergovernmental Panel on Climate Change* [Solomon, S., D. Qin, M. Manning, Z. Chen, M. Marquis, K.B. Averyt, M. Tignor and H.L. Miller (eds.)]. Cambridge University Press, Cambridge, United Kingdom and New York, NY, USA.
- Jansen, E., J. Overpeck, K.R. Briffa, J.-C. Duplessy, F. Joos, V. Masson-Delmotte, D. Olago, B. Otto-Bliesner, W.R. Peltier, S. Rahmstorf, R. Ramesh, D. Raynaud, D. Rind, O. Solomina, R. Villalba and D. Zhang (2007), Palaeoclimate. In: *Climate Change 2007: The Physical Science Basis. Contribution of Working Group I to the Fourth Assessment Report of the Intergovernmental Panel on Climate Change* [Solomon, S., D. Qin, M. Manning, Z. Chen, M. Marquis, K.B. Averyt, M. Tignor and H.L. Miller (eds.)]. Cambridge University Press, Cambridge, United Kingdom and New York, NY, USA.
- Jin, F. F. (1997), An equatorial ocean recharge paradigm for ENSO. Part I: Conceptual model, *Journal Of The Atmospheric Sciences*, 54 (7), 811–829.
-

References

- Jin, F. F., J. D. Neelin, and M. Ghil (1994), El Niño on the devil's staircase: Annual subharmonic steps to chaos, *Science*, 264, 70–72.
- Johnsen, S. J., D. Dahl-Jensen, N. Gundestrup, J. P. Steffensen, H. B. Clausen, H. Miller, V. Masson-Delmotte, A. E. Sveinbjörnsdottir, and J. White (2001), Oxygen isotope and palaeotemperature records from six Greenland ice-core stations: Camp Century, Dye-3, GRIP, GISP2, Renland and NorthGRIP, *J. Quaternary Sci.*, 16: 299–307, doi: 10.1002/jqs.622
- Jolly, D., S. P. Harrison, B. Damnati, and R. Bonnefille (1998), Simulated climate and biomes of Africa during the Late Quaternary: comparison with pollen and lake status data, *Quat. Sci. Rev.*, 17, 629–657.
- Joussaume, S., and K. E. Taylor (1995), Status of the Paleoclimate Modeling Intercomparison Project (PMIP), in Proceedings of the First International AMIP Scientific Conference, Rep. 92, pp. 425–430, *World Clim. Res. Programme*, Geneva, Switzerland.
- Jouzel, J., et al. (1996), Climatic interpretation of the recently extended Vostok ice records, *Clim. Dyn.*, 12, 513– 521.
- Kalnay, E., M. Kanamitsu, R. Kistler, W. Collins, D. Deaven, L. Gandin, M. Iredell, S. Saha, G. White, J. Woollen, Y. Zhu, M. Chelliah, W. Ebisuzaki, W. Higgins, J. Janowiak, K. C. Mo, C. Ropelewski, J. Wang, A. Leetmaa, B. Reynolds, R. Jenne, and D. Joseph (1996), The NCEP/NCAR 40-Year Reanalysis Project, *Bull. Amer. Meteor. Soc.*, 77, 437–471.
- Kanamitsu M., W. Ebisuzaki, J. Woollen, S-K Yang, J. J. Hnilo, M. Fiorino, and G. L. Potter (2002), NCEP-DEO AMIP-II Reanalysis (R-2), *Bull. Amer. Meteor. Soc.*, 1631-1643.
- Kaplan, J. O., N. H. Bigelow, I. C. Prentice, S. P. Harrison, P. J. Bartlein, T. R. Christensen, W. Cramer, N. V. Matveyeva, A. D. McGuire, D. F. Murray, V. Y. Razzhivin, B. Smith, D. A. Walker, P. M. Anderson, A. A. Andreev, L. B. Brubaker, M. E. Edwards, and A. V. Lozhkin (2003), Climate change and Arctic ecosystems: 2. Modeling, paleodata-model comparisons, and future projections. *J. Geophys. Res.*, 108, doi:10.1029/2002JD002559.
- Kaplan, M. R., and A. P. Wolfe (2006), Spatial and temporal variability of Holocene temperature in the North Atlantic region, *Quat. Res.*, 65, 223–231.
- Kessler, W. S. (2002), Is ENSO a cycle or a series of events? *Geophys. Res. Lett.*, 29(23), 2125, doi:10.1029/2002GL015924.
- Kessler, W. S., and M. J. McPhaden (1995), The 1991-93 El Niño in the central Pacific, *Deep Sea Res.*, Part II, 42, 295-334.
- Khon, Vyacheslav ; Park, Wonsun ; Latif, Mojib ; Mokhov, I.I. ; Schneider, Birgit (2010), Response of the hydrological cycle to orbital and greenhouse gas forcing In: *Geophys. Res. Lett.*, Nr. 37, S. L19705 [doi:10.1029/2010GL044377].
- Kim, J.-H., N. Rimbu, S. J. Lorenz, G. Lohmann, S.-I. Nam, S. Schouten, C. Rühlemann, R. R. Schneider (2004), North Pacific and North Atlantic sea-surface temperature variability during

-
- the Holocene, *Quaternary Science Reviews*, 23, 2141–2154, doi:10.1016/j.quascirev.2004.08.010.
- Kitoh, A., and S. Murakami (2002), Tropical Pacific climate at the mid-Holocene and the Last Glacial Maximum simulated by a coupled ocean atmosphere general circulation model. *Paleoceanography*, 17, 1047, doi:10.1029/2001PA000724.
- Kleeman, R., and A. M. Moore (1997), A theory for the limitation of ENSO predictability due to stochastic atmospheric transients, *J. Atmos. Sci.*, 54, 753–767.
- Knutson, T. R., and S. Manabe (1995), Time-mean response over the tropical Pacific to increased CO₂ in a coupled ocean–atmosphere model, *J. Clim.*, 8, 2181–2199.
- Koutavas, A., P. B. deMenocal, G. C. Olive, and J. Lynch-Stieglitz (2006), Mid-Holocene El Niño–Southern Oscillation (ENSO) attenuation revealed by individual foraminifera in eastern tropical Pacific sediments, *Geology*, 34, 993–996, doi: 10.1130/G22810A.1
- Koutavas, A., J. Lynch-Stieglitz, T. N. J. Marchitto, and J. P. Sachs (2002), El Niño-like pattern in ice age tropical Pacific sea surface temperature, *Science*, 297, 226–230.
- Krebs, U., W. Park, B. Schneider (2011), Pliocene aridification of Australia caused by tectonically induced weakening of the Indonesian throughflow. In: *Palaeogeography, Palaeoclimatology, Palaeoecology*, 309, Nr. 1-2, S. 111–117 [doi>10.1016/j.palaeo.2011.06.002].
- Kripalani, R. H., and A. Kulkarni (1997), Climatic impact of El Niño/La Niña on the Indian monsoon: A new perspective, *Weather*, 52, 39–46.
- Kucharski, F., I.-S. Kang, R. Farneti, and L. Feudale (2011), Tropical Pacific response to 20th century Atlantic warming, *Geophys. Res. Lett.*, 38, L03702, doi:10.1029/2010GL046248.
- Krishnamurthy, V., and B. N. Goswami (2000), Indian Monsoon–ENSO relationship on interdecadal timescales. *J. Clim.*, 13, 579–595.
- Kukla, G. J., M. L. Bender, J. L. de Beaulieu, G. Bond, W. S. Broecker, P. Cleveringa, J. E. Gavin, T. D. Herbert, J. Imbrie, J. Jouzel, L. D. Keigwin, K.-L. Knudsen, J. F. McManus, J. Merkt, D. R. Muhs, H. Müller, R. Z. Poore, S. C. Porter, G. Seret, N. J. Shackleton, C. Turner, P. C. Tzedakis, and I. J. Winograd (2002), Last Interglacial climates, *Quat. Res.*, 58, 2–13.
- Kutzbach, J. E., and Z. Liu (1997), Response of the African Monsoon to orbital forcing and ocean feedbacks in the middle Holocene, *Science*, 278, 440–443.
- Kutzbach, J. E., R. G. Gallimore, and P. J. Guetter (1991), Sensitivity experiments on the effects of orbitally-caused insolation changes on the interglacial climate of high northern latitudes, *Quat. Int.*, 223–229.
- Landais, A., V. Masson-Delmotte, J. Jouzel, D. Raynaud, S. Johnsen, C. Huber, M. Leuenberger, J. Schwander, and B. Minster (2006), The glacial inception as recorded in the NorthGRIP Greenland ice core: timing, structure and associated abrupt temperature changes, *Clim. Dyn.*, 26(2–3), 273–284.
-

References

- Landsea, C. W. and Knaff, J. A. (2000), How much skill was there in forecasting the very strong 1997-98 El Niño? *Bulletin of the American Meteorological Society* 81: 2107-2119.
- Latif M. and N. S. Keenlyside (2009), El Niño/Southern Oscillation response to global warming, *Proceedings of the National Academy of Sciences, PNAS* 2009, vol. 106, no. 49 pg 20578-20583, doi:10.1073/pnas.0710860105.
- Latif M., Sperber K, Arblaster J, Braconnot P, Chen D, Colman A, Cubasch U, Cooper C, Delecluse P, De Witt D, Fairhead L, Flato G, Hogan T, Ji M, Kimoto M, Kitoh A, Klutson T, Le Treut H, Li T, Manabe S, Marti O, Mechoso C, Meehl G, Power S, PoECKner E, Sirven J, Terray L, Vintzileos A, Voss R, Wang B, Washington W, Yoshikawa I, Yu J, Zebiak S (2001): ENSIP: The El Niño Simulation Intercomparison Project, *Clim. Dyn.*, 18, 255–276.
- Larkin, N. K., and D. E. Harrison (2002), ENSO warm (El Niño) and cold (La Niña) event life cycles: Ocean surface anomaly patterns, their symmetries, asymmetries, and implications, *J. Clim.*, 15, 1118–1140.
- Lau, K. M. (1985), Elements of a stochastic-dynamical theory of long-term variability of the El Niño-Southern Oscillation, *J. Atmos. Sci.*, 42, 1552–1558.
- Leduc, G., R. Schneider, J-H. Kim, and G. Lohmann (2010), Holocene and Eemian Sea surface temperature trends as revealed by alkenone and Mg/Ca paleothermometry, *Quaternary Science Reviews*, 29, 989-1004, doi:10.1016/j.quascirev.2010.01.004.
- Li, T., and T. F. Hogan (1999), The role of the annual-mean climate on seasonal and interannual variability of the tropical Pacific in a coupled GCM, *J. Clim.*, 12, 780–792.
- Li, J., S.-P. Xie, E. R. Cook, G. Huang, R. D'Arrigo, F. Liu, J. Ma, and X.-T. Zheng (2011), Interdecadal modulation of El Niño amplitude during the past millennium, *Nature Climate Change*, 1, 114-118.
- Liu, K. B. (2004), Paleotempestology: Principles, methods, and examples from Gulf coast lake-sediments. In: *Hurricanes and Typhoons: Past, Present and Future* [Murnane, R., and K. Liu (eds.)]. Columbia University Press, New York, pp. 13–57.
- Liu, Z. (1998), The Role of Ocean in the Response of Tropical Climatology to Global Warming: The West–East SST Contrast. *J. Clim.*, 11, 864–875, doi: 10.1175/1520-0442.
- Liu, Z. (2002), A simple model study of the forced response of ENSO to an external periodic forcing. *J. Clim.*, 15, 1088–1098.
- Liu, Z., and H. Yang (2003), Extratropical control of tropical climate, the atmosphere bridge and oceanic tunnel, *Geophys. Res. Lett.*, Vol. 30, No. 5, 1230, doi:10.1029/2002GL016492.
- Liu, Z., E. Brady., and J. Lynch-Stieglitz (2003), Global ocean response to orbital forcing in the Holocene, *Paleoceanography*, vol. 18, NO. 2, 1041, doi:10.1029/2002PA000819.
- Liu, Z., and B. Huang (2000), Cause of tropical Pacific warming trend, *Geophys. Res. Lett.*, 27, 1935–1938.

-
- Liu, Z., J. Kutzbach, and L. Wu (2000), Modeling Climate Shift of El Niño Variability in the Holocene, *Geophys. Res. Lett.*, 27(15), 2265-2268.
- Liu, Z., S. P. Harrison, J. Kutzbach, and B. Otto-Bliesner (2004), Global monsoons in the mid-Holocene and oceanic feedback, *Climate Dynamics*, 22: 157–182, DOI 10.1007/s00382-003-0372-y.
- Liu, Z., S. Vavrus, F. He, N. Wen, and Y. Zhong (2005), Rethinking tropical ocean response to global warming: The enhanced equatorial warming, *J. Clim.*, 18, 4684–4700.
- Lorenz, S. J., and G. Lohmann (2004), Acceleration technique for Milankovitch type forcing in a coupled atmosphere-ocean circulation model: method and application for the Holocene, *Clim. Dyn.*, 23, 727–743.
- Lorenz, S. J., J.-H. Kim, N. Rimbu, R. R. Schneider, and G. Lohmann (2006), Orbitally driven insolation forcing on Holocene climate trends: Evidence from alkenone data and climate modeling, *Paleoceanography*, 21, PA1002, doi:10.1029/2005PA001152.
- Lorius, C., J. Jouzel, C. Ritz, L. Merlivat, N.I. Barkov, Y. S. Korotkevitch, and V. M. Kotlyakov (1995), A 150,000-year climatic record from Antarctic ice, *Nature* 316:591-596.
- Luo, J.-J., S. Masson, E. Roeckner, G. Madec and T. Yamagata (2005), Reducing climatology bias in an ocean-atmosphere CGCM with improved coupling physics, *J. Clim.*, 18, 2344-2360.
- MacDonald, G. M., A. A. Velichko, C. V. Kremenetski, O. K. Borisova, A. A. Goleva, A. A. Andreev, Les C. Cwynar, R. T. Riding, S. L. Forman, T. W. D. Edwards, R. Aravena, D. Hammarlund, J. M. Szeicz, V. N. Gattaulin (2000), Holocene treeline history and climate change across northern Eurasia, *Quat. Res.*, 53, 302–311.
- Madec, G. (2008), NEMO ocean engine. Notes du Pole de Modélisation 27, *Tech. rep.*, Institut Pierre Simon Laplace, Paris.
- Madec, G., P. Delecluse, M. Imbard, and C. Levy (1998), OPA 8.1 Ocean General Circulation Model reference manual, Note Pole Model. 11, 91 pp., Inst. Pierre-Simon Laplace, Paris.
- Marchal O., I. Cacho, T. F. Stocker, J. O. Grimalt, E. Calvo, B. Martrat, N. Shackleton, M. Vautravers, E. Cortijo, S. van Kreveld, C. Andersson, N. Koc, M. Chapman, L. Scaffi, J.-C. Duplessy, M. Sarnthein, J.-L. Turon, and J. Duprat, E. Jansen (2002), Apparent long-term cooling of the sea surface in the northeast Atlantic and Mediterranean during the Holocene, *Quat. Sci. Rev.*, 21 (4–6), 455–483.
- Stute M., A. Clement, and G. Lohmann (2001), Global climate models: Past, present, and future, *PNAS*, vol. 98 no. 19 10529-10530, doi: 10.1073/pnas.191366098.
- Marra, M. J. (2003), Last interglacial beetle fauna from New Zealand, *Quart. Res.*, 59, 122–131.
- Masson-Delmotte, V., J. Jouzel, A. Landais, M. Stievenard, S. J. Johnsen, J. W. C. White, M. Werner, A. Sveinbjornsdottir, and K. Fuhrer (2005), GRIP deuterium excess reveals rapid and orbital-scale changes in Greenland moisture origin, *Science*, 309(5731), 118–121.
-

References

- Mayewski, P. A., E. Rohling, C. Stager, K. Karlén, K. Maasch, L. D. Meeker, E. A. Meyerson, F. Gasse, S. van Kreveld, K. Holmgren, J. Lee-Thorp, G. Rosqvist, F. Rack, M. Staubwasser, and R. R. Schneider, E. J. Steig (2004), Holocene climate variability, *Quaternary Research*, 62, 243-255.
- Mechoso, C. R., A. W. Robertson, N. Barth, M. K. Davey, P. Delecluse, P. R. Gent, S. Ineson, B. Kirtman, M. Latif, H. Le Treut, T. Nagal, J. D. Neelin, S. G. H. Philander, J. Polcher, P. S. Schopf, T. Stockdale, M. J. Suarez, L. Terray, O. Thual, and J. J. Tribbia (1995), The seasonal cycle in the Tropical Pacific in Coupled Ocean-Atmosphere General Circulation Models. *Month. Weath. Rev.*, 123, 2825-2838.
- McCreary, J. (1976), Eastern tropical Ocean response to changing wind systems, with application to El Niño, *J. Phys Oceanogr.*, 6, 632-645.
- McGregor, H. V., and M. K. Gagan (2004), Western Pacific coral $\delta^{18}\text{O}$ records of anomalous Holocene variability in the El Niño-Southern Oscillation, *Geophys. Res. Lett.*, 31(11), doi:10.1029/2004GL019972.
- McPhaden M. J., et al. (1999), Genesis and Evolution of the 1997-98 El Niño, *Science*, vol 283.
- McPhaden M. J., A. J. Busalacchi, R. Cheney, J. R. Donguy, K. S. Gage, D. Halpern, M. Ji, P. Julian, G. Meyers, G. T. Mitchum, P. P. Niiler, J. Picaut, R. W. Reynolds, N. Smith, and K. Takeuchi (1998), The tropical Ocean Global Atmosphere observing system: A decade of progress, *J. Geophys. Res.*, 103, 14,169–14,240.
- McPhaden M. J., and J. Picaut (1990), El Niño-Southern Oscillation displacements of the western equatorial Pacific warm pool, *Science*, 250:1 385-1 388.
- McPhaden M. J., S. E. Zebiak, and M. H. Glantz (2006), ENSO as an integrating concept in Earth science, *Science*, 314, 1740-1745.
- McWilliams, J., and P. Gent (1978), A coupled air-sea model for the tropical Pacific, *J. Atmos. Sci.*, 35, 962–989.
- Meehl, G. A., P. R. Gent, J. M. Arblaster, B. L. Otto Bliesner, E. C. Brady, and A. Graig (2001), Factors that affect the amplitude of El Niño in global climate couple model, *Clim. Dyn.*, 17, 515-526.
- Meehl, G. A., H. Teng, and G. Branstator (2006), Future changes of El Niño in two global coupled climate models, *Clim. Dyn.*, 26: 549–566 DOI 10.1007/s00382-005-0098-0.
- Meehl, G. A., and W. M. Washington (1996), El Niño-like climate change in a model with increased atmospheric CO₂ concentrations, *Nature*, 382, 56–60.
- Milankovitch, M. (1941), Kanon der Erdbestrahlung und seine Anwendung auf das Eiszeitenproblem, Spec. Publ., 132, 633 pp., Royal Serb. Acad., Belgrade. (Translated version: Milankovitch, M. (1941), *Canon of Insolation and the Ice Age Problem*. Königlich Serbische Academie,

-
- Belgrade. English translation by the Israel Program for Scientific Translations, United States Department of Commerce and the National Science Foundation, Washington D.C., 1969).
- Mitchell, T. P., and J. M. Wallace (1992), The annual cycle in equatorial convection and sea surface temperature. *J. Clim.*, 5, 1140–1156.
- Moore, A. M. and R. Kleeman (1999), Stochastic forcing of ENSO by intraseasonal oscillations, *J. Clim.*, 12, 1199–1220.
- Monterey, G. I., and S. Levitus (1997), Climatological cycle of mixed layer depth in the world ocean. U.S. Gov. Printing Office, NOAA NESDIS, 5pp (data source: www.esrl.noaa.gov/psd).
- Montoya, M., H. von Storch, and T. J. Crowley (2000), Climate simulation for 125 kyr BP with a coupled ocean-atmosphere general circulation model, *Journal of Climate*, 13(6), 1057–1072.
- Moy, C. M., Geoffrey O. Seltzer, Donald T. Rodbell & David M. Anderson (2002), Variability of El Niño/Southern Oscillation activity at millennial timescales during the Holocene epoch, *Nature*, 420, 162-165.
- Muhs, D. R., K. R. Simmons, and B. Steinke (2002), Timing and warmth of the last interglacial period: New U-series evidence from Hawaii and Bermuda and a new fossil compilation for North America, *Quat. Sci. Rev.*, 21, 1355–1383.
- Neelin, J. D., D. S. Battisti, A. C. Hirst, F. F. Jin, Y. Wakata, T. Yamagata, and S. E. Zebiak (1998), ENSO theory, *J. of Geophys. Res.-Oceans*, 103 (C7), 14261–14290.
- Neelin, J. D., and Latif, Mojib (1998), El Niño dynamics. *Physics Today*, December, 32-36.
- Neelin, J. D., M. Latif, and F.F. Jin (1994), Dynamics of coupled ocean-atmosphere models: The tropical problem, *Ann. Rev. Fluid. Mech.*, 26, 617-659.
- Neelin, J. D., M. Latif, M. A. F. Allaart, M. A. Cane, U. Cubasch, W. L. Gates, P. R. Gent, M. Ghil, C. Gordon, N. C. Lau, C. R. Mechoso, G. A. Meehl, J. M. Oberhuber, S. G. H. Philander, P. S. Schopf, K. R. Sperber, A. Sterl, T. Tokioka, J. Tribbia, and S. E. Zebiak (1992), Tropical air-sea interaction in general circulation models, *Clim. Dyn.*, 7, 73-104.
- NGRIP (North Greenland Ice Core Project) (2004), High-resolution record of Northern Hemisphere climate extending into the last interglacial period. *Nature*, 431, 147–151.
- Nicholson S. E. (2009), A revised picture of the structure of the “monsoon” and land ITCZ over West Africa, *Clim Dyn.*, 32:1155–1171, DOI 10.1007/s00382-008-0514-3.
- Newton, A., R. Thunell, and L. Stott (2011), Changes in the Indonesian Throughflow during the past 2000 years, *Geology*, 39, 63-66.
- Otto-Bliesner, B. L. (1999), El Niño/La Niña and Sahel precipitation during the middle Holocene. *Geophys. Res. Lett.*, 26, 87-90.
- Otto-Bliesner B., E. Brady, S. Shin, Z. Liu, and C. Shield (2003), Modeling El Niño and its tropical teleconnections during the last glacial-interglacial cycle, *Geophys. Res. Lett.*, 30, doi:10.1029/2003GL018553.
-

References

- Otto-Bliesner B. L., S. Marshall, J. Overpeck, G. Miller, A. Hu, and CAPE Last Interglacial Project Members (2006), Simulating Arctic Climate Warmth and Icefield Retreat in the Last Interglaciation, *Science*, 311(5768):1751–1753, doi:10.1126/science.1120808, PMID 16556838.
- Overpeck, J. T., and 20 others (2005), Arctic system on trajectory to new, seasonally ice-free state: Eos (Transactions, American Geophysical Union), v. 86, p. 309–313.
- Ó Gráda, C. (2009), *Famine: A Short History*", Princeton University Press, Chap. 1, pg 16, ISBN 978-0-691-12237-3.
- Page S. E., F. Siebert, J. O. Rieley, H. D. V. Boehm, A. Jaya, and S. Limin (2002), The amount of carbon released from peat and forest fires in Indonesia during 1997, *Nature* 420:61–65.
- Park, W., and M. Latif (2011), Atlantic Meridional Overturning Circulation Response to Idealized External Forcing, *Clim. Dyn.*, published online. DOI: 10.1007/s0
- Park, W., and M. Latif (2010), Pacific and Atlantic Multidecadal Variability in the Kiel Climate Model, *Geophys. Res. Lett.*, 37, L24702. doi:10.1029/2010GL045560
- Park, W., and M. Latif (2008), Multidecadal and multicentennial variability of the meridional overturning circulation, *Geophys. Res. Lett.*, doi:10.1029/2008GL035779.
- Park, W., N. Keenlyside, M. Latif, A. Stroeh, R. Redler, E. Roeckner, and G. Madec (2009), Tropical Pacific Climate and Its Response to Global Warming in the Kiel Climate Model, *J. Clim.*, 22, 71-92.
- Penland, C., and P. D. Sardeshmukh (1995), The optimal growth of tropical sea surface temperature anomalies, *J. Clim.*, 8, 1999–2024.
- Petit, J. R., J. Jouzel, D. Raynaud, N. I. Barkov, J.-M. Barnola, I. Basile, M. Bender, J. Chappellaz, M. Davis, G. Delaygue, M. Delmotte, V. M. Kotlyakov, M. Legrand, V. Y. Lipenkov, C. Lorius, L. Pépin, C. Ritz, E. Saltzman, and M. Stievenard (1999), Climate and atmospheric history of the past 420,000 years from the Vostok ice core, Antarctica, *Nature*, 399, 429–436.
- Pielke, Jr., R. A., and C. W. Landsea (1999), La Niña, El Niño, and Atlantic Hurricane Damages in the United States, *Bull. Amer. Meteor. Soc.*, 80, 2027-2033.
- Philander, S. G. H. (1990), *El Niño, La Niña, and the Southern Oscillation*, Academic, London.
- Philander, S. G. H. (1999), A review of tropical ocean-atmosphere interactions, *Tellus*, 51,71-90.
- Philander, S. G. H., D. Gu, D. Halpern, G. Lambert, N.-C. Lau, T. Li, and R. C. Pacanowski (1996), The role of low-level stratus clouds in keeping the ITCZ mostly north of the equator, *J. Clim.*, Vol. 9, No. 12, 2958-2972.
- Phillips J., and B. McIntyre (2000), ENSO and Interannual rainfall Variability in Uganda: Implications for Agricultural Management, *Int. J. Climatol.* 20: 171–182.

-
- Prentice, I. C., and T. Webb (1998), BIOME 6000: reconstructing global mid-Holocene vegetation patterns from palaeoecological records, *J. Biogeogr.*, 25 (6), 997–1005.
- Prentice, I. C., D. Jolly, and Biome 6000 Participants (2000), Mid-Holocene and glacial-maximum vegetation geography of the northern continents and Africa, *J. Biogeogr.*, 27, 507–519.
- Rahmstorf, S., and H. J. Schellnhuber (2006), *Der Klimawandel*, Beck Verlag, Munich, 144 pp.
- Rayner, N. A., D. E. Parker, E. B. Horton, C. K. Folland, L. V. Alexander, D. P. Rowell, E. C. Kent, and A. Kaplan (2003), Global analyses of sea surface temperature, sea ice, and night marine air temperature since the late nineteenth century, *J. Geophys. Res.*, 108, 4407, doi:10.1029/2002JD002670.
- Roeckner, E., R. Brokopf, M. Esch, M. Giorgetta, S. Hagemann, L. Kornblueh, E. Manzini, U. Schlese, and U. Schulzweida (2003), The atmospheric general circulation model ECHAM5. Part I: Model description, Rep. 349, *Tech. rep.*, Max Planck Institut für Meteorologie, Hamburg, Germany.
- Rodbell, D. T., G. O. Seltzer, D. M. Anderson, M. B. Abbott, D. B. Enfield, and J. H. Newman (1999), An ~15,000-Year Record of El Niño-Driven Alluviation in Southwestern Ecuador, *Science*, 283, 516-520.
- Rohling, E. J., R. Abu-Zied, J. S. L. Casford, A. Hayes, and B. A. A. Hoogakker (2008), The Mediterranean Sea: Present and Past (Source: <http://www.soes.soton.ac.uk/staff/ejr/Rohling-papers/2008-Rohling%20et%20al.pdf>).
- Rostami, K., W. R. Peltier, and A. Mangini (2000), Quaternary marine terraces, sea-level changes and uplift history of Patagonia, Argentina. Comparisons with predictions of ICE-4G (VM2) model of the global process of glacial isostatic adjustment, *Quat. Sci. Rev.*, 19, 1495–1525.
- Sellers H., H. Zhang, G. Berz, K. Emanuel, W. Gray, C. Landsea, G. Holland, J. Lighthill, S-L. Shieh, P. Webster, and K. McGuffie (1998), Tropical Cyclones and Global Climate Change: A Post-IPCC Assessment, *Bull. Amer. Meteor. Soc.*, 79, 19-38.
- Schimmel D. S., D. Baker (2002), Carbon cycle: the wildfire factor, *Nature* 420:29–30.
- Schneider B., G. Leduc, and W. Park (2010), Disentangling seasonal signals in Holocene climate trends by satellite-model-proxy integration, *Paleoceanography*, 25, PA4217, doi:10.1029/2009PA001893.
- Shin, S.-Ik, P. D. Sardeshmukh, R. S. Webb, R. J. Oglesby, and J. J. Barsugli (2006), Understanding the Mid-Holocene Climate, *J. Clim.*, 19, 2801–2817.
- Shulmeister, J., and B. G. Lees (1995), Pollen evidence from tropical Australia for the onset of an ENSO-dominated climate at c. 4000BP, *The Holocene*, 5, 10-18.
- Sirocko, F., K. Seelos, K. Schaber, B. Rein, F. Dreher, M. Diehl, R. Lehne, K. Jäger, M. Krbetschek, and D. Degering (2005), A late Eemian aridity pulse in central Europe during the last glacial inception, *Nature* 436 (7052): 833–836, doi:10.1038/nature03905. PMID 16094365.
-

References

- Solomon, S., D. Qin, M. Manning, Z. Chen, M. Marquis, K. B. Averyt, M. Tignor, and H. L. Miller, Eds. (2007), *Climate Change 2007: The Physical Science Basis*. Cambridge University Press, Cambridge, United Kingdom, 996 pp.
- Spencer, H., R. Sutton, and J. M. Slingo (2007), El Niño in a Coupled Climate Model: Sensitivity to Changes in Mean State Induced by Heat Flux and Wind Stress Corrections, *J. Clim.*, 20, 2273–2298, doi: 10.1175/JCLI4111.1
- Stenseth, N. Chr, A. Mysterud, G. Ottersen, J. W. Hurrell, K.-S. Chan, and M. Lima (2002), Ecological effects of climate fluctuations, *Science*, 297, 1292-1296. [DOI:10.1126/science.1071281].
- Stirling C. H., T. M. Esat, K. Lambeck, and M. T. McCulloch (1998), Timing and duration of the last interglacial: evidence for a restricted interval of widespread coral reef growth, *Earth Planet. Sci. Lett.*, 160, 745–762.
- Ströh Achim (2007), The impact of global warming on El Niño-Southern Oscillation, Diplomarbeit, 2007.
- Sun, D.-Z., and Z. Liu (1996), Dynamic ocean–atmosphere coupling: A thermostat for the tropics. *Science*, 272, 1148–1150.
- Taft, B. A., and W. S. Kessler, Variations of zonal currents in the central tropical Pacific during 1970 to 1987 (1991), Sea level and dynamich eightm easurements, *J. Geophys. Res.*, 96, 12,599-12,618.
- Timm, O., A. Timmermann, A. Abe-Ouchi, F. Saito, and T. Segawa (2008), On the definition of seasons in paleoclimate simulations with orbital forcing, *Paleoceanography*, 23, PA2221, doi:10.1029/2007PA001461.
- Timmermann A., S. J. Lorenz, S.-I. An, A. Clement, and S.-P. Xie (2007), The effect of orbital forcing on the mean climate and variability of the tropical Pacific, *J. Clim.*, 20, 4147–4159.
- Timmermann A., J. Oberhuber, A. Bacher, M. Esch, M. Latif, and E. Roeckner (1999), Increased El Niño Frequency in a climate model forced by future greenhouse warming, *Nature*, 398, 694–697.
- Tomczak, M., and J S. Godfrey (2003), *Regional Oceanography: an Introduction*, 2nd edition, Daya Pub, ISBN : 81-7035-307-6
- Tompkins, A. M. (2002), A prognostic parameterization for the subgrid-scale variability of water vapor and clouds in large-scale models and its use to diagnose cloud cover, *J. Atmos. Sci.*, 59 (12), 1917–1942.
- Thompson, C. J., and D. S. Battisti (2001), A linear stochastic dynamical model of ENSO. Part II: Analysis, *J. Clim.*, 14, 445–466.
- Trenberth, K. E. (1998), Atmospheric moisture residence times and cycling: Implications for rainfall rates and climate change, *Clim. Change*, 39, 667-694.

-
- Tudhope, A. W., C. P. Chilcott, M. T. McCulloch, E. R. Cook, J. Chappell, R. M. Ellam, D. W. Lea, J. M. Lough, and G. B. Shimmield (2001), Variability in the El Niño-southern oscillation through a glacial-interglacial cycle, *Science*, 291, 1511–1517.
- Turner A. G., P. M. Inness, and J. M. Slingo (2005), The role of the basic state in the ENSO-monsoon relationship and implications for predictability, *Q.J.R. Meteorol. Soc.*, 131:781–804, doi: 10.1256/qj.04.70.
- Valcke, S. (2006), OASIS3 user guide, PRISM Tech. Rep. 3, 64 pp., Partnership for Res. Infrastructures in Earth Syst. Model., Toulouse, France.
(Available at http://www.prism.enes.org/Publications/Reports/oasis3_UserGuide_T3.pdf).
- Vecchi, G. A., B. J. Soden, A. T. Wittenberg, I. M. Held, A. Leetmaa, and M. J. Harrison (2006), Weakening of tropical Pacific atmospheric circulation due to anthropogenic forcing, *Nature*, 441, 73-76, doi:10.1038.
- Vettoretti, G., and W. R. Peltier (2004), Sensitivity of glacial inception to orbital and greenhouse gas climate forcing. *Quat. Sci. Rev.* 23, 499-519.
- Visser, K., R. Thunell, and L. Stott (2003), Magnitude and timing of temperature change in the Indo-Pacific warm pool during deglaciation, *Nature*, 421, 152– 155.
- Voss, R., and U. Mikolajewicz (2001), The Climate of 6000 Years BP in Near-Equilibrium Simulations with a Coupled AOGCM, *Geophys. Res. Lett.*, 28(11), 2213-2216.
- Wang, C., and J. Picaut (2004), Understanding ENSO physics - A review. In: *Earth's Climate: The Ocean-Atmosphere Interaction*. C. Wang, S.-P. Xie, and J. A. Carton, Eds., AGU Geophysical Monograph Series, 147:21-48.
- Wang, F. (2007), Investigating ENSO sensitivity to mean climate in an intermediate model using a novel statistical technique, *Geophys. Res. Lett.*, 34, L07705, doi:10.1029/2007GL029348.
- Wang, G., and D. Schimel (2003), Climate change, climate modes, and climate impacts, *Annu. Rev. Environ. Resour.*, 28:1-28, doi:10.1146/annurev.energy.28.050302.105444.
- Wainwright, L., G. Meyers, S. Wijffels, and L. Pigot (2008), Change in the Indonesian Throughflow with the climatic shift of 1976/77, *Geophys. Res. Lett.*, 35, L03604, doi: 10.1029/2007GL031911.
- Walsh, K., and A. B. Pittock (1998), Potential changes in tropical storms, hurricanes, and extreme rainfall events as a result of climate change, *Climatic Change* 39: 199-213.
- Wanner, H., J. Beer, J. Bütikofer, T. J. Crowley, U. Cubasch, J. Flückiger, H. Goosse, M. Grosjean, F. Joos, J. O. Kaplan, M. Küttel, S. A. Müller, I. C. Prentice, O. Solomina, T. F. Stocker, P. Tarasov, M. Wagner, and M. Widmann (2008), Mid- to Late Holocene climate change: An overview, *Quat. Science Reviews*, 27, 1791-1828, doi:10.1016/j.quascirev.2008.06.013.

References

- Watanabe, O., J. Jouzel, S. Johnsen, F. Parrenin, H. Shojik, and N. Yoshida (2003), Homogeneous climate variability across East Antarctica over the past three glacial cycles, *Nature*, 422, 509–512.
- Webster P., and S. Yang (1992), Monsoon and ENSO: selectively interactive system, *Q. J. R. Meteorol. Soc.*, 118, 877-926.
- Wyrtki, K (1975), El Niño - The dynamic response of the equatorial Pacific Ocean to atmospheric forcing, *J. Phys Oceanogr.*, 5, 572-584.
- Xie S.-P. (1994), On the genesis of the equatorial annual cycle, *J. Clim.*, 7, 2008–2013.
- Xie S.-P., C. Deser, G. A. Vecchi, J. Ma, H. Teng, and A. T. Wittenberg (2010), Global Warming Pattern Formation: Sea Surface Temperature and Rainfall, *J. Climate*, 23, 966–986, doi: 10.1175/2009JCLI3329.1.
- Xie S.-P., Miyama, T., Wang Y., Xu H., deSzoeko S. P., Small R.J., Richards, K. J., Mochizuki T., and T. Awaji (2007), A regional ocean-atmosphere model for eastern Pacific climate: towards reducing tropical biases, *J. Clim.*, 20, 1504-1522.
- Zavala-Garay, J., A. M. Moore, C. L. Perez, and R. Kleeman (2003), The response of a coupled mode of ENSO to observed estimates of stochastic forcing, *J. Clim.*, 16, 2827–2842.
- Zebiak, S. E., and M. A. Cane (1987), A model El Niño–Southern Oscillation, *Mon. Wea. Rev.*, 115, 2262–2278.
- Zelle, H., G. van Oldenborgh, and H. Dijkstra (2005), El Niño and greenhouse warming: Results from ensemble simulations with the NCAR CCSM, *J. Clim.*, 18, 4669–4683, doi: <http://dx.doi.org/10.1175/JCLI3574.1>.
- Zeng, N., and J. D. Neelin (2000), The role of vegetation-climate interaction and interannual variability in shaping the African Savanna, *J. Clim.*, 13, 2665-2670.
- Zhang Caiyun, and Cheng Ge (2008), The atmospheric wet pool: definition and comparison with the oceanic warm pool, *Chinese Journal of Oceanology and Limnology*, Vol. 26 No. 4, P. 440-449, DOI: 10.1007/s00343-008-0440-6.
- Zhang, R., and T. L. Delworth (2005), Simulated tropical response to a substantial weakening of the Atlantic thermohaline circulation, *J. of Clim.*, v. 18, p. 1853–1860, doi: 10.1175/JCLI3460.1.
- Zheng, W., P. Braconnot, E. Guilyardi, U. Merkel, and Y. Yu (2008), ENSO at 6ka and 21ka from ocean–atmosphere coupled model simulations, *Clim. Dyn.*, 30, 745–762, DOI 10.1007/s00382-007-0320-3.
- Zhao, Y., P. Braconnot, O. Marti, S. P. Harrison, C. Hewitt, A. Kitoh, Z. Liu, U. Mikolajewicz, B. Otto-Bliesner, and S. L. Weber (2005), A multi-model analysis of the role of the ocean on the African and Indian monsoon during the mid-Holocene, *Clim. Dyn.*, 25, (7–8), 777–800.

CURRICULUM VITAE

Personal Information

Name: SALAU, Opeyemi R. S.
Date of Birth: 21st May 1970
Sex / Marital Status: Male / Married
Nationality: Nigerian

University Qualifications

2008-2011: PhD Study at the Institute of Geosciences, University of Kiel, Germany.
PhD Thesis: “El Niño/Southern Oscillation during the Holocene and Eemian Warm Periods”.

2005-2007: M. Sc at the Institute of Environmental Physics, University of Bremen, Germany.
M. Sc. Thesis: “Tropospheric Trace Gases at Bremen Measured With FTIR Spectrometry”.

1998-2000: M. Sc study at the University of Ibadan, Ibadan, Nigeria. M. Sc.
Thesis: “Computation of Geomagnetic Elements for Nigeria, Africa and the World for the year 2000 and 2010”.

1990-1995: B. Sc Ondo State University, Ado–Ekiti (now University of Ado-Ekiti), Nigeria.
B. Sc. Thesis: “Gamma Ray Spectrometry in Evaluation of Natural Radioactivity in Aramoko-Ekiti, Nigeria”.



Erklärung

Hiermit erkläre ich, dass die vorliegende Arbeit – abgesehen von der Beratung durch Prof. Birgit Schneider – nach Inhalt und Form meine eigene Arbeit ist und nach den Regeln guter wissenschaftlicher Praxis der Deutschen Forschungsgemeinschaft entstanden ist. Es wurden – abgesehen von der Beratung durch meine akademischen Lehrer – keine anderen als die angegebenen Quellen und Hilfsmittel verwendet. Die Arbeit wurde bis jetzt weder ganz noch teilweise an anderer Stelle im Rahmen eines Prüfungsverfahrens vorgelegt.

Kiel, den

.....

Opeyemi Salau